REPORT DOCUMENTATION PAGE

Form Approved
OMB NO. 0704-0188

1. AGENCY USE ONLY (Leave Blank)	2. REPORT DATE 2 Jan. 20001	3. REPORT TYPE AND DATES COVERED FINAL Ol Sep 96 - 30 May 99

4. TITLE AND SUBTITLE
INSTRUMENTATION FOR ULTRAHIGH RESOLUTION TEMPORAL AND SPATIAL STUDIES OF MATERIALS AND DEVICES

5. FUNDING NUMBERS
DAAH049610279

6. AUTHOR(S)
CHRISTOPHER C. DAVIS

7. PERFORMING ORGANIZATION NAME(S) AND ADDRESS(ES)
DEPARTMENT OF ELECTRICAL AND COMPUTER ENGINEERING
UNIVERSITY OF MARYLAND
COLLEGE PAK, MD 20742

8. PERFORMING ORGANIZATION REPORT NUMBER N/A

9. SPONSORING / MONITORING AGENCY NAME(S) AND ADDRESS(ES)

U. S. Army Research Office
P.O. Box 12211
Research Triangle Park, NC 27709-2211

10. SPONSORING / MONITORING AGENCY REPORT NUMBER

ARO 36115.1-PH-RIP

11. SUPPLEMENTARY NOTES
The views, opinions and/or findings contained in this report are those of the author(s) and should not be construed as an official Department of the Army position, policy or decision, unless so designated by other documentation.

12 a. DISTRIBUTION / AVAILABILITY STATEMENT

Approved for public release: distribution unlimited.

12 b. DISTRIBUTION CODE

13. ABSTRACT (Maximum 200 words)

This contract provided support for the procurement of equipment to build and operate improved near-field scanning optical microscopes (NSOMs). Improved scanning stages were constructed, and a scheme for high speed scanning developed based on distance regulation with tuning forks. In this scheme the phase of the drive to the fork is monitored with a digital phase-locked loop, which allows very rapid adjustment of the fork position in response to damping changes that occur as the fork and optical fiber tip are scanned in close proximity to a surface. In addition, new excitation and detection schemes were developed, which have allowed us to pioneer the use of nonlinear NSOM for the study of ferroelectric and ferromagnetic domains, and the crystal structure of surfaces

14. SUBJECT TERMS
Near-Field Scanning Optical Microscopy, Nonlinear Imaging, Plasmons, Nonlinear Optics

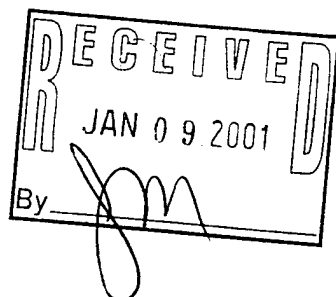**15. NUMBER OF PAGES**
23 + Appendices

16. PRICE CODE

17. SECURITY CLASSIFICATION OR REPORT UNCLASSIFIED	18. SECURITY CLASSIFICATION ON THIS PAGE UNCLASSIFIED	19. SECURITY CLASSIFICATION OF ABSTRACT UNCLASSIFIED	20. LIMITATION OF ABSTRACT UL

RECEIVED JAN 0 9 2001
By

20010227 130

FINAL REPORT ON CONTRACT DAAH049610279

Instrumentation for Ultrahigh Resolution
Temporal and Spatial Studies of Materials and Devices

Submitted by

Christopher C. Davis
Department of Electrical and Computer Engineering
University of Maryland
College Park, MD 20742

Phone: (301)405-3637
FAX: (391)314-9281
e-mail: davis@eng.umd.edu

Report Date: January 2, 2001

Abstract

This contract provided support for the procurement of equipment to build and operate improved near-field scanning optical microscopes (NSOMs). Improved scanning stages were constructed, and a scheme for high speed scanning developed based on distance regulation with tuning forks. In this scheme the phase of the drive to the fork is monitored with a digital phase-locked loop, which allows very rapid adjustment of the fork position in response to damping changes that occur as the fork and optical fiber tip are scanned in close proximity to a surface. In addition, new excitation and detection schemes were developed, which have allowed us to pioneer the use of nonlinear NSOM for the study of ferroelectric and ferromagnetic domains, and the crystal structure of surfaces

Table of Contants

SUMMARY

Our research on near-field scanning optical microscopy, and primarily its application in nonlinear studies of surfaces was greatly enhanced by the additional scanning and detection equipment procured from contract funds. We have used nonlinear near-field imaging to study various interesting characteristics of technologically important anisotropic materials such as piezoceramics, ferroelectrics, and ferromagnetics. These studies have included studies of both thin film and bulk devices. Near-field imaging with bare tapered fiber optic probes, which is a technique pioneered by us, provides minimally invasive information about domain alignment, poling directions, domain structure, and domain dynamics in both passive and active devices with a resolution on the order of 25-50nm. Ferroelectric materials such as $BaTiO_3$ and $Pb(Zr_xTi_{1-x})O_3$ (PZT) are of special interest because these materials are being increasingly used in memory systems. We have shown that the location and alignment of domains in these materials can be determined by examining the polarization dependence of second harmonic generation (SHG) in the near-field. We have improved the signal-to-noise ratio in these experiments by using femtosecond Ti:sapphire laser excitation, since the phenomena we are studying provide only weak signals unless femtosecond pulsed lasers of high peak intensity are used.

We have also carried out technological improvements on scanning techniques in NSOM using tuning fork distance control and rapid digital phase-locked loop techniques to acquire tip to sample separation and permit fast scanning and a shorter residence time per pixel

INTRODUCTION

Near-field scanning optical microscopy (NSOM) has become a relatively mature technique during the last ten years, although there continue to be difficulties in image interpretation when this technique is used as a pure imaging tool. However, the use of near-field probes for specific excitation or interrogation of surfaces suffers from fewer ambiguities. This is especially true when bare tapered fiber probes with end diameters of 50nm or less are used. We have used such probes for direct observation of near-field emission of developmental diode lasers, for studying the dynamics of surface plasmons, for the study of lithography on a 100nm scale, for studying the effects of surface roughness on SHG at metal films, for visualization of ferromagnetic domains in ferrromagnetic materials, and for examining photon bandgap effects in periodic optical structures. Near-field probes with a metal coating, which are very commonly used for high resolution suffer from artefacts, especially the excitation of surface plasmons in the tip coating itself, which makes them unsuitable for minimally invasive probing. Bare probes provide a local field enhancement, although this is not as great as can be achieved with sharp metal probes. However, this can still give a substantial enhancement in local SHG, which depends on the fourth power of the applied field.

NANOMETER SCALE CRYSTAL ANALYSIS USING NEAR-FIELD OPTICAL SECOND HARMONIC MICROSCOPY: APPLICATION TO THIN FERROELECTRIC FILMS

In this section we provide details of how we carry out nonlinear NSOM in a particular case to illustrate the scope of the research we have carried out. We describe how near-field optical scanning for second harmonic imaging using tapered optical fiber tips externally illuminated with femtosecond laser pulses is carried out. Enhancement of the electric field at the tip of the fiber results in enhanced second harmonic generation (SHG) from the sample region near the tip. This SH emission is collected by the same tapered fiber. In preliminary experiments polarization properties of second harmonic generation from a poled single crystal of $BaTiO_3$ have been studied experimentally and theoretically in the near and far field zones for different orientations of poling direction with respect to the tip and the incoming fundamental light. Good agreement between theory and experiment has been demonstrated. Symmetry properties of the near-field SH signal allow us to recover the local poling direction of individual ferroelectric domains in polycrystalline thin ferroelectric films with spatial resolution of the order of 80 nm. Near-field strain-induced SHG from thin $Ba_xSr_{1-x}TiO_3$ films has also been studied, and excellent agreement between theory and experiment has been established. Thus, nonlinear near-field scanning microscopy has been shown to be a novel tool for nanometer scale crystal analysis of polycrystalline samples.

NONLINEAR GENERATION AT SURFACES.

Optical second harmonic generation (SHG) is an extremely sensitive technique for characterization and investigation of a wide variety of materials, surfaces and adsorbates [1]. SHG is especially useful for recovery of the symmetry properties of the sample under investigation. Far-field SH microscopy has already demonstrated its great potential in such fields as magnetic imaging [2] and metal-oxide-semiconductor device characterization [3]. However, in many applications a spatial resolution below the diffraction limit of far-field optics is required. For example, better than 100 nm resolution is required in characterization of thin ferroelectric films such as $BaTiO_3$ and $Pb(Zr_xTi_{1-x})O_3$ (or PZT), which form the basis of a new thin film technology for data storage [4]. The ultimate performance (density and speed of operation) of these devices depends on the spatio-temporal properties of individual ferroelectric domains. A better understanding of these properties requires experiments performed with nanometer spatial and sub-nanosecond temporal resolution. Near-field optical microscopy may be the technique of choice for such experiments. Its main advantages in comparison with other scanning probe techniques are the possibility of fast time-resolved measurements, and substantially smaller perturbation of the sample under investigation caused by the optical probe. As a result, many attempts have been made recently [5-7] to implement different near-field optical techniques for SH imaging. Unfortunately, even the best resolution reported so far, 140 nm [7] obtained with a widely adopted aperture near-field probe [8], falls short of the desired range. The main experimental problem in near-field SH imaging is low optical signal, since SHG is generally a weak effect, and it is extremely difficult to detect using an aperture fiber probe with a typical throughput of less than 10^{-4} for a 100 nm aperture.

An apertureless approach to near-field microscopy [9] is usually based on local field perturbation or on the local field enhancement by laser-illuminated sharp metal tips. In the latter case the metal tip provides a local excitation source for the spectroscopic response of the sample under investigation. Unfortunately, this approach is difficult to apply to SH microscopy, since a laser illuminated metal tip would be a source of SHG comparable to the near-field SH signal from the sample. In this paper, we present a near-field optical technique for second harmonic imaging using a bare tapered optical fiber tip externally illuminated with femtosecond laser pulses. We show theoretically and experimentally that under illumination with P-polarized light the local SHG from the sample region under the tip is strongly enhanced even in the case of a dielectric tip. At the same time, the glass tip itself does not generate any measurable SH light. The local SH emission from the sample region under the tip is collected by the same tapered fiber, which has a field of view on the order of half the wavelength of SH light $\lambda_{2\omega}/2$ in diameter, where $\lambda_{2\omega}$=400 nm (this is the resolution limit of a linear near-field microscope using bare tapered fibers). This configuration automatically solves one of the main problems in apertureless near-field microscopy: rejection of the background signal from the entire illuminated sample area. As a result, spatial resolution on the order of 80 nm has been achieved in imaging of thin ferroelectric films. Symmetry properties of the near-field SH signal studied experimentally and theoretically have allowed us to recover local poling direction of individual ferroelectric domains in polycrystalline thin ferroelectric films. Thus, the developed technique may be considered as a novel tool for nanometer scale crystal analysis of polycrystalline samples. Measurements of strain induced near-field SHG in thin $Ba_xSr_{1-x}TiO_3$ films have also allowed us to establish near-field second harmonic microscopy as a unique tool for nanometer scale strain analysis of thin films.

EXPERIMENTAL SETUP

One experimental setup we have used is shown in Fig.1. Weakly focused light (illuminated spot diameter on the order of 50 μm) from a Ti:sapphire laser system consisting of an oscillator and a regenerative amplifier operating at 810 nm (repetition rate up to 250 kHz, 100-fs pulse duration, and up to 10 μJ pulse energy) was directed at an angle of incidence around 50° onto the sample surface. Excitation power at the sample surface was kept well below the ablation threshold. The local SHG was collected using an uncoated adiabatically tapered fiber tip, which is drawn at the end of a single mode fiber by the standard heating and pulling procedure. Tip curvature was measured using a scanning electron microscope. A fiber tip with an end diameter of about 50 nm was scanned over the sample surface with a constant tip-surface distance of a few nanometers using shear force feedback control [8]. Therefore, surface topography images were obtained while simultaneously recording the SH near-field images. A typical set of such images of a 0.5 μm thick pulsed laser deposited PZT film grown on a Si wafer substrate obtained under excitation with P- and S- polarized fundamental light is presented in Fig.2. The topographical image in Fig.2(a) shows the

grain structure of the film. Higher than usual noise in the image is caused by less stable behavior of the shear-force feedback control when the tip is illuminated with femtosecond laser pulses. This may be caused by local evaporation of the thin water layer absorbed on the sample surface, which is believed to contribute to the shear force. The SH image in Fig.2(b) obtained under illumination with P-polarized fundamental light clearly shows fine structure of SHG within individual grains. Fundamental light distribution was also measured and did not show any variations on this scale.

RESULTS AND DISCUSSIONS

1. Study of near-field SHG from single crystals of $BaTiO_3$.

Optical SHG is widely used to characterize the average structure and crystal orientation of ferroelectric films [10]. Near-field second harmonic microscopy is the logical extension of these far-field techniques. In order to understand its main contrast mechanisms (and, as a result, understand the origin of the fine structure in Fig.2) we performed a study of the polarization properties of the near- and far-field SH signal using a poled single crystal of $BaTiO_3$ as a sample ($BaTiO_3$ and $Pb(Zr_xTi_{1-x})O_3$ have similar perovskite structure and belong to the same tetragonal symmetry class). Phase-matched SHG is prohibited in the bulk of $BaTiO_3$ because of its strong dispersion [11]. As a result, the measured SH signal originates at the surface, which makes the experimental situation look very similar to the case of a thin film. Near-field SH signal dependencies on the polarization of the fundamental light for three different poling (optical axis) directions of $BaTiO_3$ crystal are shown in Fig.3. The SH signal exhibits approximate 4-fold symmetry with respect to polarization angle rotation in the case (a) of poling (optical axis) direction located in the incidence plane of the fundamental light parallel to the crystal surface. The symmetry becomes 2-fold in the case (b) when the optical axis is perpendicular to the incidence plane. In case (c) (when the poling direction is perpendicular to the crystal surface) SH signal is much weaker than in cases (a) and (b). Big differences between these dependencies indicate that the near-field SHG may be used to recover local poling direction in thin ferroelectric films. In order to do this, we must achieve some theoretical understanding of the reasons for such a difference. Another important question is: how good is the spatial resolution of the near-field SH microscopy in the experimental geometry discussed above?

Surprisingly, most of the features of the near-field SHG may be understood from a very simple theoretical model. Let us consider fundamental light illuminating the tip of the microscope located near the $BaTiO_3$ crystal surface. Three different cases of the poling vector orientation are shown in Fig.4(a,b,c), where α is the incidence angle, and the z-axis is chosen to coincide with the poling direction of the crystal. All three cases may be considered in a similar way, so we will concentrate on case (b) and only present the final results for the cases (a) and (c). Let us consider the fundamental optical field distribution in the tip-sample region at distances much smaller then the wavelength λ of the fundamental light. In this region the quasi-electrostatic approximation may be used. The tip shape may be approximated as an ellipsoid with a very high aspect ratio. For P-polarized excitation light and y-component (the component perpendicular to the sample surface) of the optical field the exact analytic solution of the Laplace equation [12] gives $E_{tip}(\omega)=\varepsilon E_{y0}(\omega)$ where ε is the dielectric constant of the tip, E_{y0} is the incoming field and E_{tip} is the y-component of the field just below the tip apex. As a result, for the incidence angles α around $\pi/2$ the local SHG under the tip is enhanced by a factor of n^8 (since $I(2\omega)_{tip}=E^2_{tip}(2\omega)=E^4_{tip}(\omega)=n^8 E^4_{y0}(\omega)$), where n is the tip refractive index. Assuming n=1.6 the enhancement factor equals about 40. It may be even higher (of the order of $(2\varepsilon)^4$) in the vicinity of a sample surface with a high dielectric constant, such as a metal or a ferroelectric, due to the image potential. Exact tip enhancement factors in non-linear near-field microscopy were calculated by Y. Kawata *et al.* [13] for different tip-sample pairs. For example, in the case of a diamond/air/diamond tip-sample gap E^4_{tip} may be enhanced by a factor of 600. However, in our discussion to follow, we will not consider any particular value of the field enhancement factor. Instead, we denote the fundamental field enhancement factor by γ. The fundamental optical field components under the tip apex at a polarization angle ϕ can be written approximately as:

$$E_x = E\cos\phi\cos\alpha, \qquad E_y = (\gamma/\varepsilon_b)E\cos\phi\sin\alpha, \qquad E_z = E\sin\phi, \qquad (1)$$

where ε_b is the dielectric constant of $BaTiO_3$, $\phi=0$ and $\phi=90°$ correspond to P-polarized and S-polarized excitation light respectively. Taking into account the non-zero components of the second harmonic susceptibility tensor for $BaTiO_3$: $\chi^{(2)}_{yyz} = \chi^{(2)}_{xxz} = \chi^{(2)}_{yzy} = \chi^{(2)}_{xzx} =17.7\times10^{-12}$ m/V, $\chi^{(2)}_{zyy} = \chi^{(2)}_{zxx} = $ -

18.8×10^{-12} m/V, and $\chi^{(2)}_{zzz} = -7.1 \times 10^{-12}$ m/V (where z is the poling direction) [14], the second harmonic field components at the tip apex may be written as:

$$D^{(2)}_x = \chi^{(2)}_{zxx}E^2\sin^2\phi\cos\alpha, \qquad D^{(2)}_y = (\gamma/\varepsilon_b)\chi^{(2)}_{xzx}E^2\sin^2\phi\sin\alpha, \qquad (2)$$

$$D^{(2)}_z = (\gamma^2/\varepsilon_b^2)\chi^{(2)}_{zxx}E^2\cos^2\phi\sin^2\alpha + \chi^{(2)}_{zxx}E^2\cos^2\phi\cos^2\alpha + \chi^{(2)}_{zzz}E^2\sin^2\phi$$

If we assume that the microscope tip collects only dipole radiation, the second harmonic optical signal will be proportional to

$$I^{(2)} = D^{(2)2}_z + D^{(2)2}_x \qquad (3)$$

(SH dipoles that oscillate along the y-direction do not radiate towards the tip). Similar calculations of the field at the tip apex are easy to perform for cases (a) and (c). Let us point out that within our model the angular dependencies of the field E for the points in space around the tip apex should be approximately the same as in (1). Only the enhancement factor γ is different for these points (its value changes from a maximum just under the tip apex to $\gamma=1$ far from the apex). So, in the final result one must replace the factors γ^4 and γ^2 by the average values $<\gamma^4>$ and $<\gamma^2>$ taken over all the area around the tip apex where the SH signal is collected. The diameter of this area is approximately $\lambda_{2\omega}/3 - \lambda_{2\omega}/2$ which is the theoretical resolution limit of near-field optical microscopy in the collection mode performed with uncoated fiber tips [15].

The final results of our calculations are presented in Fig.5. The best agreement with experimentally measured symmetry properties of the near-field SH polarization curves was achieved in the $\gamma = 5 -7$ range for the field enhancement factor. This is reasonably close to the expected value of $\gamma = 2\varepsilon_{tip}$. A much smaller value of the SH signal in case (c) is a consequence of the fact that $I^{(2)}$ contains terms proportional to $<\gamma^4>$ in the cases (a) and (b), but in case (c) the SH signal $I^{(2)}$ is proportional to $<\gamma^2>$:

$$I^{(2)} = D^{(2)2}_x + D^{(2)2}_y = (<\gamma^2>/\varepsilon_b^2)\chi^{(2)2}_{xzx}E^4(\sin^2 2\phi\sin^2\alpha+\cos^4\phi\sin^2 2\alpha) \qquad (4)$$

The transition from near-field mode to far-field mode operation of the microscope (which corresponds to an increase in the tip-sample separation from a few nanometers to a distance of a few wavelengths of light) can be described mathematically within our model as a transition from $\gamma = 5 - 7$ to $\gamma=1$ (no field enhancement by the tip). Results of numerical calculations for such a transition performed using (3) are shown in Fig.6. Experimental data shown in the same figure are in good qualitative agreement with the calculations: both theoretical and experimental data have the same symmetry of the SH polarization dependencies in the near-field and far-field zones. This indicates that our simple model provides an adequate description of the essential physics involved in near-field observation of SHG from ferroelectric samples.

2. Measurements of local poling direction in thin BaTiO$_3$ and PZT films.

We have performed similar local polarization properties measurements in different areas of thin $BaTiO_3$ and $Pb(Zr_xTi_{1-x})O_3$ films. An example of such measurements is presented in Fig.7. The data obtained at points A, B and C of Fig.7(b) show close resemblance to the curves (a), (b) and (c) respectively in Fig.3. Optical properties of $Pb(Zr_xTi_{1-x})O_3$ and $BaTiO_3$ are similar to each other, with $Pb(Zr_xTi_{1-x})O_3$ (or PZT) having somewhat higher values of refractive index and nonlinear susceptibility: $n_o=2.610$ and $n_e=2.611$ at 800 nm; $n_o=2.966$ and $n_e=2.967$ at 400 nm; $\chi^{(2)}_{yyz} = \chi^{(2)}_{xxz} = \chi^{(2)}_{yzy} = \chi^{(2)}_{xzx} =37.9 \times 10^{-12}$ m/V, $\chi^{(2)}_{zyy} = \chi^{(2)}_{zxx} = -42.8 \times 10^{-12}$ m/V, and $\chi^{(2)}_{zzz} = -8.5 \times 10^{-12}$ m/V at 1060 nm [16,17]. Thus, our theoretical analysis performed for $BaTiO_3$ should also be applicable to PZT films. As a result, the localized areas of dark and bright SHG in Fig.7(b) should be identified as regions with different poling (optical axis) directions. Similarly, the areas of bright SHG from Fig.2(b) localized within bigger crystalline grains (visible in topography), and separated by thin dark boundaries, should be identified as individual ferroelectric domains separated by domain boundaries. A similar multidomain structure of grains in thin pulse laser deposited PZT films was observed in [18]. Very high spatial resolution of the near-field SH image is evident from Fig.2(d) where the apparent thickness of a domain boundary is equal to 80 nm. Such a high spatial resolution may seem surprising since theoretical estimates of the resolution obtained with uncoated fiber tips in linear near-field measurements varies within the $\lambda/2 - \lambda/3$ range [15]. The following simple estimate shows that in the SH mode the resolution obtained with adiabatically tapered uncoated tips can be an order of magnitude better. From the theoretical discussion above and the experimental data shown in Fig.6 it is clear that the fundamental field component parallel to the microscope tip (and perpendicular to the sample surface) is enhanced by a factor γ of the order of $\gamma = 5 - 7$. This leads to the local SH signal enhancement at the tip apex by a factor of up to γ^4 for P-polarized excitation light. The fiber tip of the microscope collects SHG

from a sample area limited by a circle with a diameter on the order of $\lambda_{2\omega}/2$, where $\lambda_{2\omega}$ is the wavelength of SH light. But the sample area just below the tip dominates the resulting SH signal. As a result, the resolution of the microscope in the SH mode is determined by the fiber tip diameter d, which was on the order of 50 nm in our experiments. Even better resolution may be expected using thinner tips or tips with higher refractive indices. The tip contribution and the contribution from all the other sample surface become equal at a tip diameter determined by $\gamma^4 d^2 = (\lambda_{2\omega}/2)^2$ or $d = \lambda_{2\omega}/(2\gamma^2)$ which may be as small as 10 - 30 nm. In fact, more severe limitations on the resolution of the microscope are caused by the small number of SH photons collected by the microscope tip. In our setup the SH signal was measured with a photomultiplier and a gated photon counter. The gate was open only for the duration of a single photon pulse from the photomultiplier in sync with the femtosecond pulses of the laser. The SH signal at every point of the image was averaged over 100-300 ms. The characteristic SH photon counting rate was on the order of one photon count per 100-300 laser pulses. Thus, the image acquisition time was on the order of 20-30 minutes. Further increase of the microscope resolution is limited by the time of measurement rather than by achievement of a better tip geometry.

SH imaging performed with S-polarized excitation light provides another verification of the proposed mechanism for high spatial resolution. Since fundamental field components perpendicular to the tip axes do not experience any substantial enhancement, one should expect much smaller SH signal collected in this case. SH images in Fig.2(b) and Fig.2(c) obtained from the same region of the PZT film under P-polarized and S-polarized excitation light clearly show the expected behavior.

Another proof of high spatial resolution achieved in our measurements of local poling direction has been obtained by observation of sudden symmetry changes in SH polarization dependencies performed with 45 nm spatial steps (Fig.8). After obtaining the topographical and SH images shown in Fig.8(a) and Fig.8(b) respectively, we have performed point by point measurements of local SH polarization dependencies over the region which show clear change in SH contrast. These measurements were done by moving the tip in 45 nm steps from left to right through the points on the film surface indicated in both the topographical and SH images. The data obtained are shown in Fig.8(c), where the curves are numbered in succession. A clear transition from 4-fold symmetry (curves 1-3) to 2-fold symmetry (curves 8 and 9) has been observed with a narrow intermediate region (curves 4-7) which does not show any polarization dependence of SHG.

3. Strain induced near-field SHG in thin $Ba_xSr_{1-x}TiO_3$ films.

We also applied our near-field setup to visualize strain induced SHG in thin $Ba_xSr_{1-x}TiO_3$ (or BST) films grown on LaO substrates. At room temperature bulk BST has the centrosymmetric cubic m3m crystal symmetry, for which bulk SHG should be absent. The Curie temperature of BST for a phase transition into a ferroelectric state is about 240K. As has been shown recently [19], thin BST films may generate SH light because of strain due to the lattice mismatch. The nonlinear susceptibility values of these films measured in [19] are sufficiently different from those of BaTiO$_3$ and PZT: $\chi^{(2)}_{yyz} = \chi^{(2)}_{xxz} = \chi^{(2)}_{yzy} = \chi^{(2)}_{xzx} = 2.2\times10^{-12}$ m/V, $\chi^{(2)}_{zyy} = \chi^{(2)}_{zxx} = -4.7\times10^{-12}$ m/V, and $\chi^{(2)}_{zzz} = -11.0\times10^{-12}$ m/V (where z is the strain direction). As a result, theoretical near-field SH signal polarization dependencies calculated for different strain directions and shown in Fig.9 differ substantially from the dependencies in Figs. 3 and 5. For instance, curve (b) obtained for a strain direction perpendicular to the incidence plane of the fundamental light shows SH maxima for S-polarized excitation light. This behavior was never observed with BaTiO$_3$ and PZT samples, but it was routinely observed (see Fig.10(c)) in experiments conducted with BST films. Curve B in Fig.10(c) represents typical polarization behavior of the SH signal measured in different areas of the SH image in Fig.10(b). After the sample had been rotated by 90°, the typical polarization behavior changed (curve A in Fig.10(c)). Curves A and B look similar to theoretical curves in Fig.9 (a) and (b) respectively, which is another indication that our simple theoretical model provides an adequate description of near-field SH measurements.

Near-field SH signal observed from BST films was an order of magnitude weaker than the signal observed with PZT films, which required substantially longer image acquisition times. Nevertheless, SH imaging was possible and an example of such images obtained with a 0.4 μm thick BST film are presented in Fig.10(a,b). The SH image (Fig.10(b)) is supposed to show the distribution of mechanical strain in the film. Features as small as 200 nm are clearly detectable in this image. They are probably caused by the terrace structure of the LaO substrate, which was clearly visible and has the same spatial orientation as the orientation of stripes in the SH image.

In conclusion, an apertureless near-field optical technique for second harmonic imaging with optical resolution on the order of 80 nm has been developed. Polarization properties of second harmonic generation from a poled single crystal of $BaTiO_3$ have been studied experimentally and theoretically in the near and far field zones for different orientations of poling direction with respect to the tip and the incoming fundamental light. Good agreement between theory and experiment is demonstrated. Symmetry properties of the near-field SH signal allow us to recover local poling direction of individual ferroelectric domains in polycrystalline thin ferroelectric films with spatial resolution on the order of 80 nm. Near-field strain-induced SHG from thin $Ba_xSr_{1-x}TiO_3$ films has also been studied, and excellent agreement between theory and experiment has been established. Thus, the described technique provides a novel tool for nanometer scale crystal and strain analysis of polycrystalline samples.
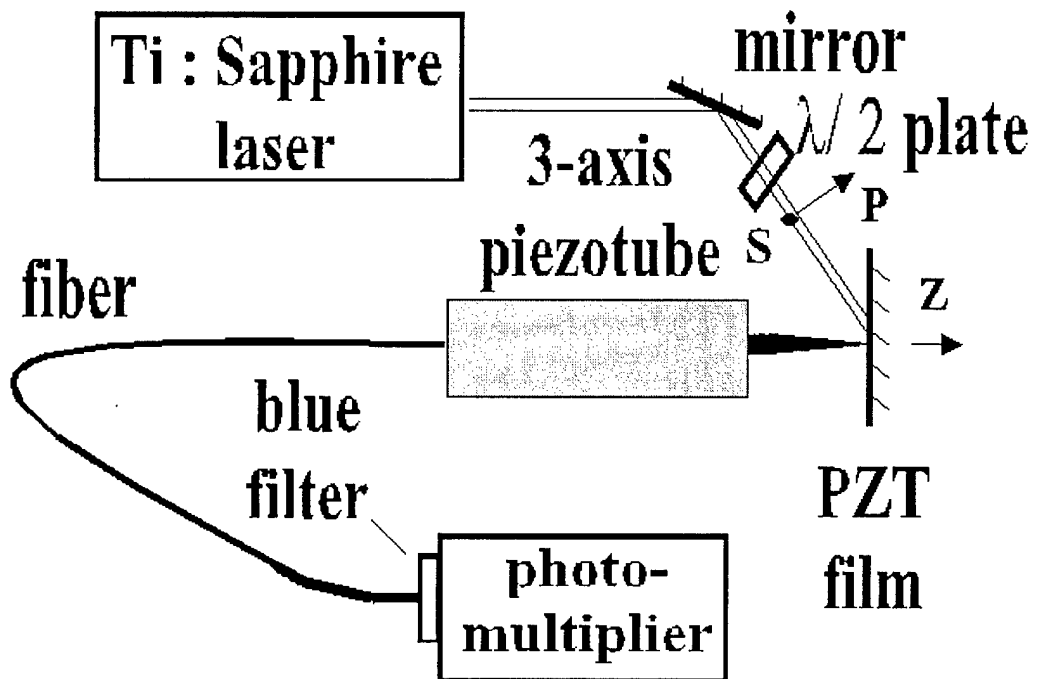
Figure 1. Schematic view of our near-field SH microscopy setup. P- and S- polarization directions of the fundamental light are indicated.
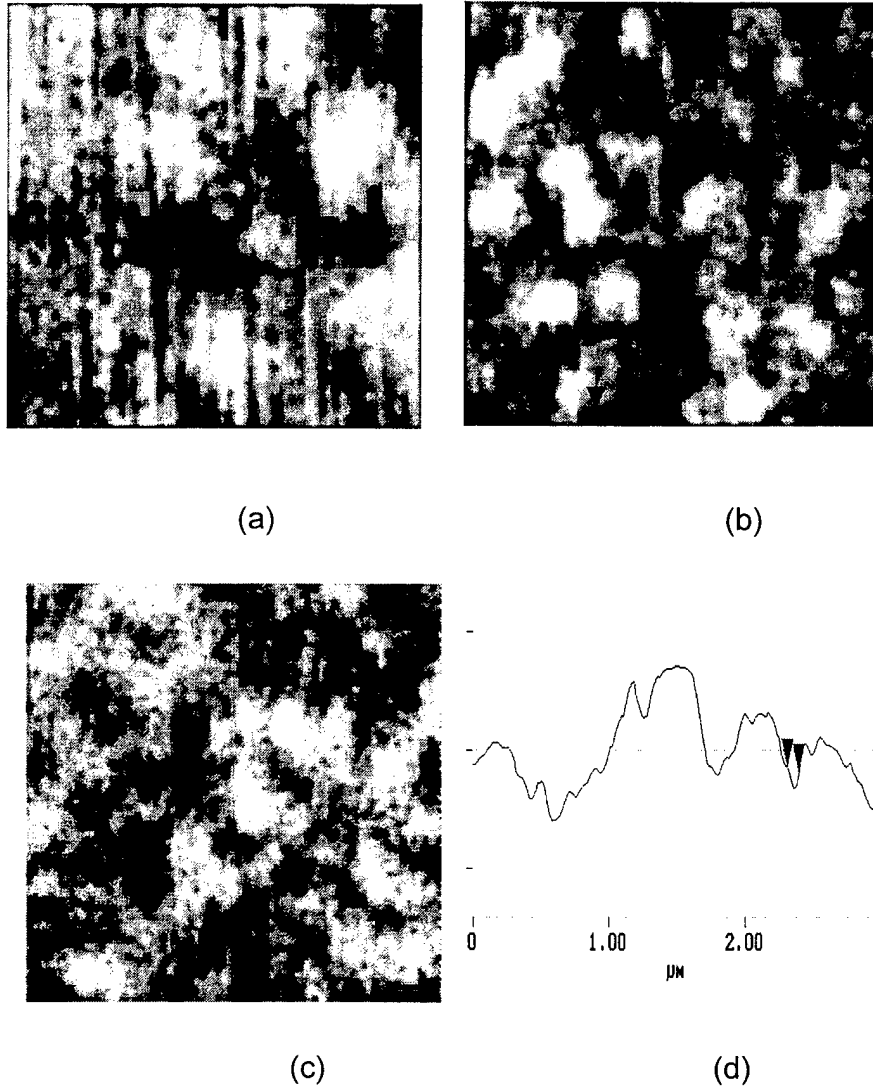
(a)

(b)

(c)

(d)

Figure 2. Simultaneously measured shear-force topographical (a) and SH near-field optical images (b,c) of a 0.5 μm thick PZT film surface obtained respectively with P- and S-polarized excitation light. The size of the images is 3 μm by 3 μm. Height variation within the topographical image is 82 nm. (d) Cross-section of the near-field image along the direction shown in (b). The apparent domain boundary width shown by the markers equals 80 nm.

11

Figure 3. Near-field SH signal dependencies on the polarization of fundamental light for three different poling directions of BaTiO₃ crystal (shown by the arrows) with respect to the incoming fundamental light (shown by the straight lines). P- and S- polarization directions of the fundamental light are indicated.
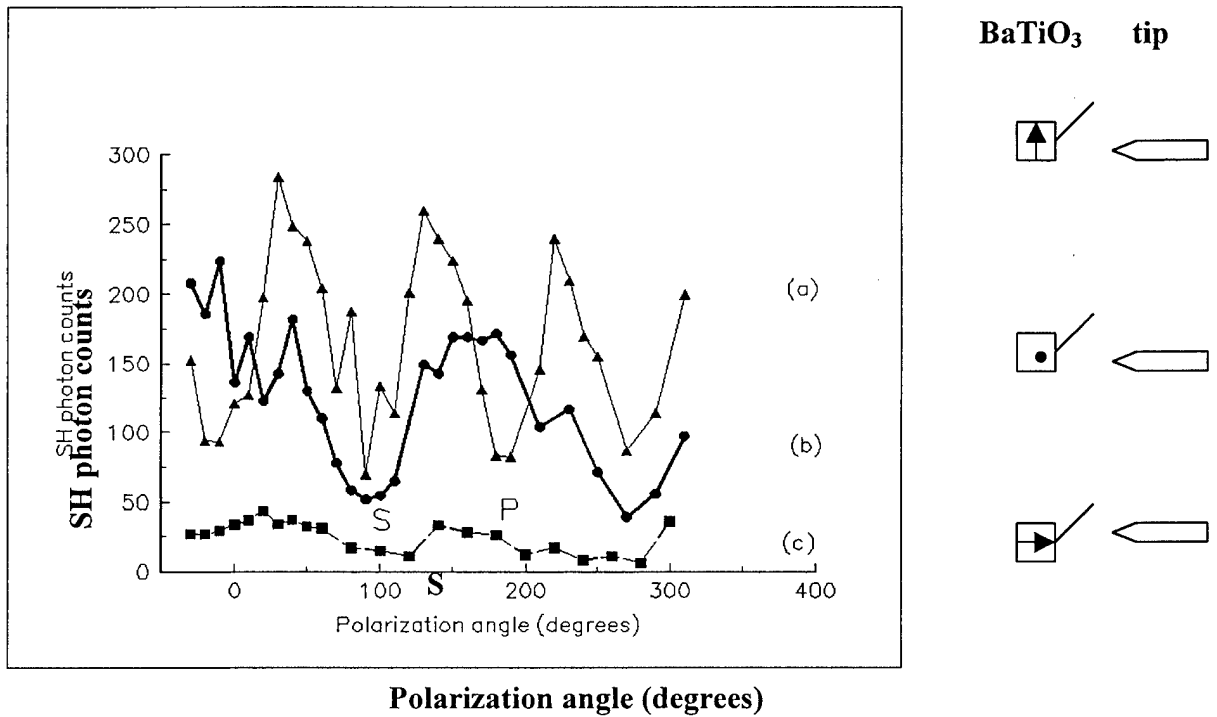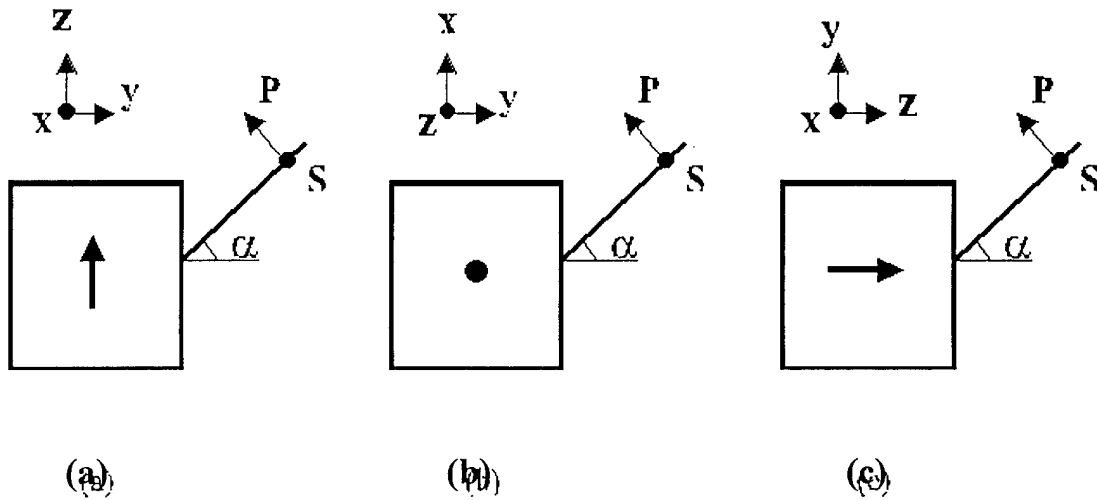

Polarization angle (degrees)

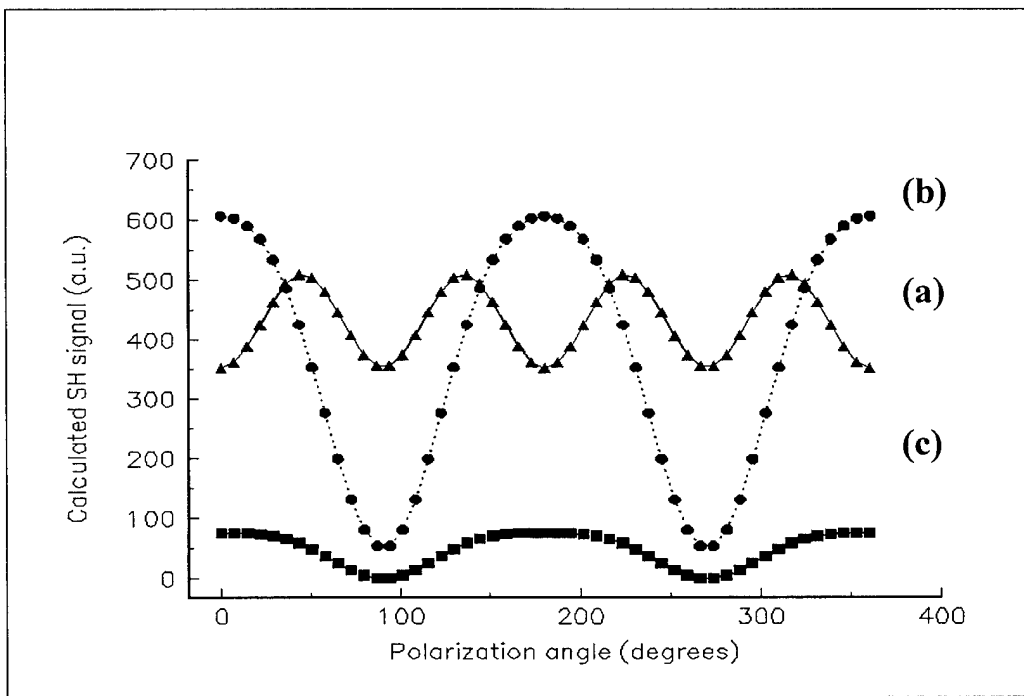Figure 4. Orientation of the BaTiO₃ crystal with respect to the illuminating fundamental light for curves (a), (b), and (c) in Fig.3.

Figure 5. Theoretical near-field SH signal dependencies on the polarization angle of fundamental light obtained in the geometry (a), (b) and (c) from Fig.4 for the field enhancement factor $\gamma = 7$ and $\alpha = 45°$.

Figure 6. Theoretical (open circles and triangles) and experimentally measured (filled circles and triangles) data for the transition from the near-field to the far-field behavior of the SH signal polarization dependency for geometry (b) from Fig.4.
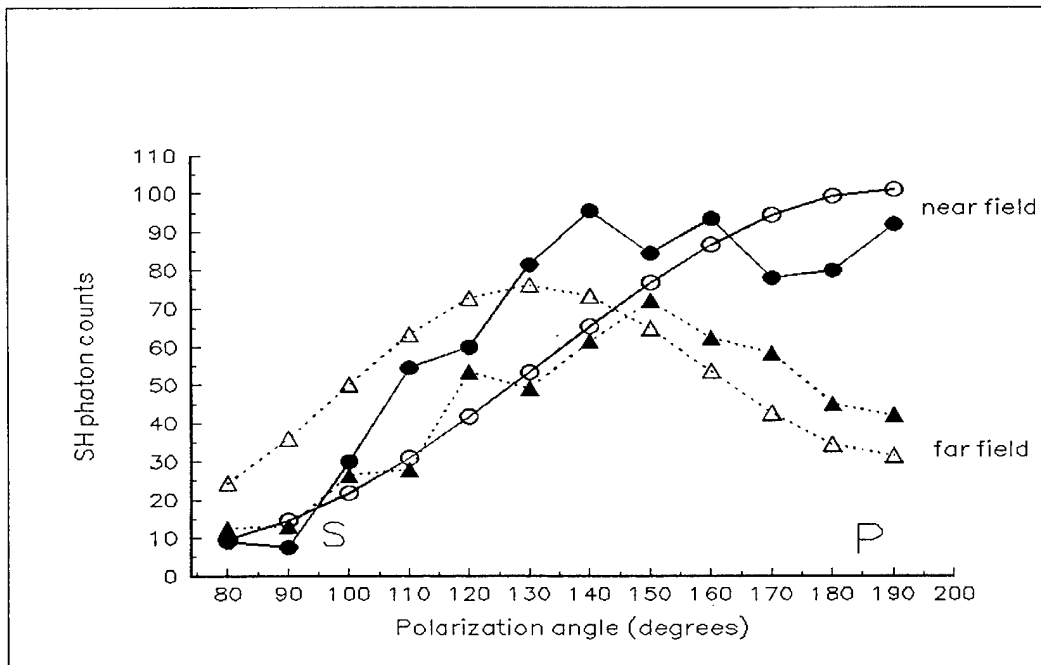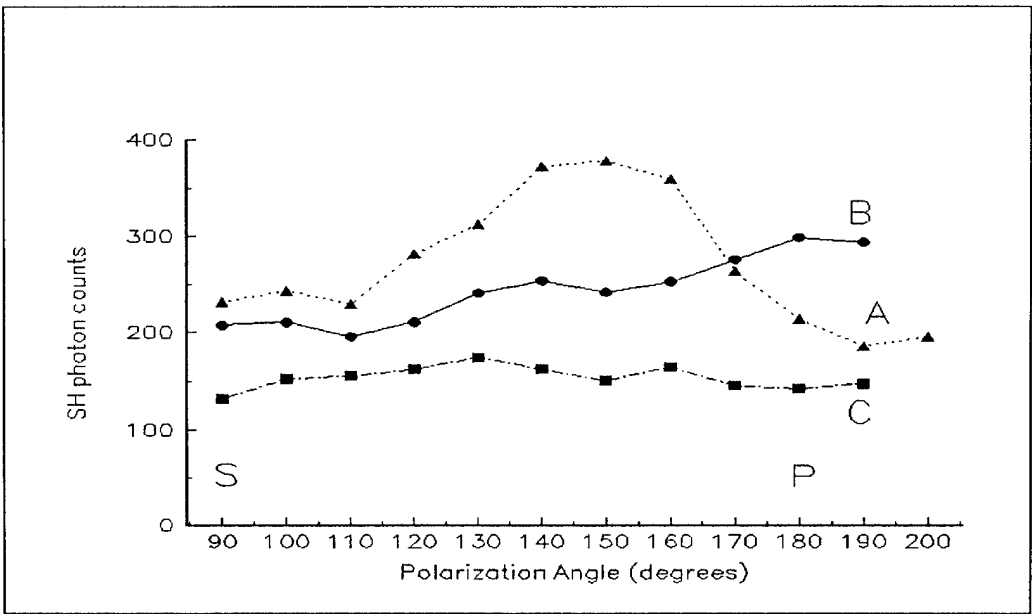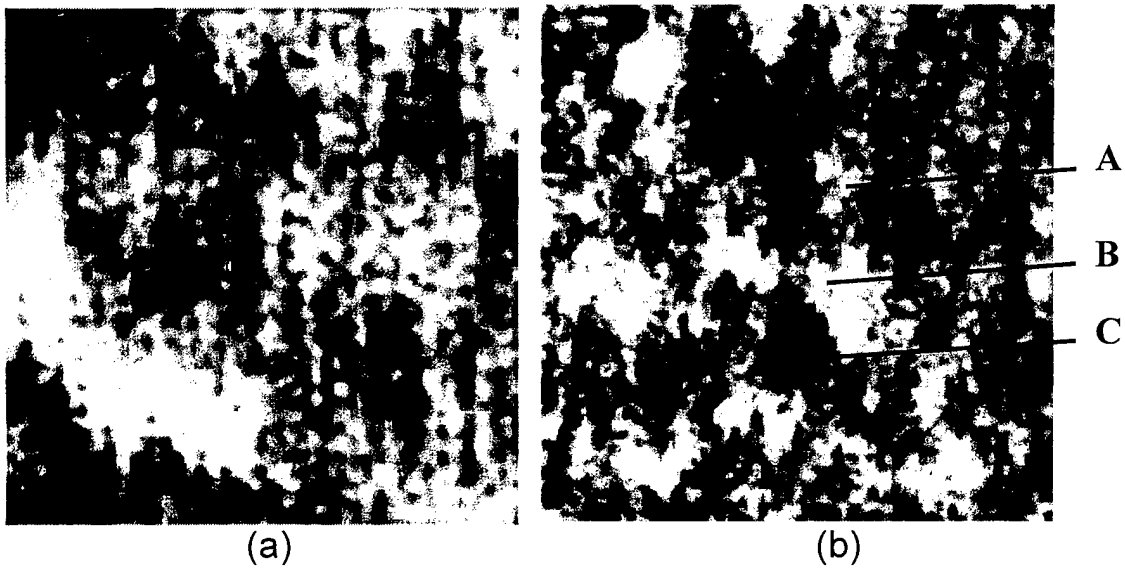
Figure 7. Simultaneously measured (a) topographical and SH near-field optical image (b) of a PZT film. 3 μm by 3 μm images were obtained using P- polarized excitation light. Height variation within the topographical image is 90 nm. Near-field SH signal dependencies on the polarization of the fundamental light taken at three different points A, B and C of the images are shown in (c).

Figure 8. Simultaneously measured (a) topographical and SH near-field optical image (b) of a PZT film. 3 μm by 3 μm images were obtained using P- polarized excitation light. Height variation within the topographical image is 75 nm. Near-field SH signal dependencies on the polarization of the fundamental light taken at 9 points indicated in the images are shown in (c). The spacing between the points is 45 nm. The points are numbered in succession from left to right.
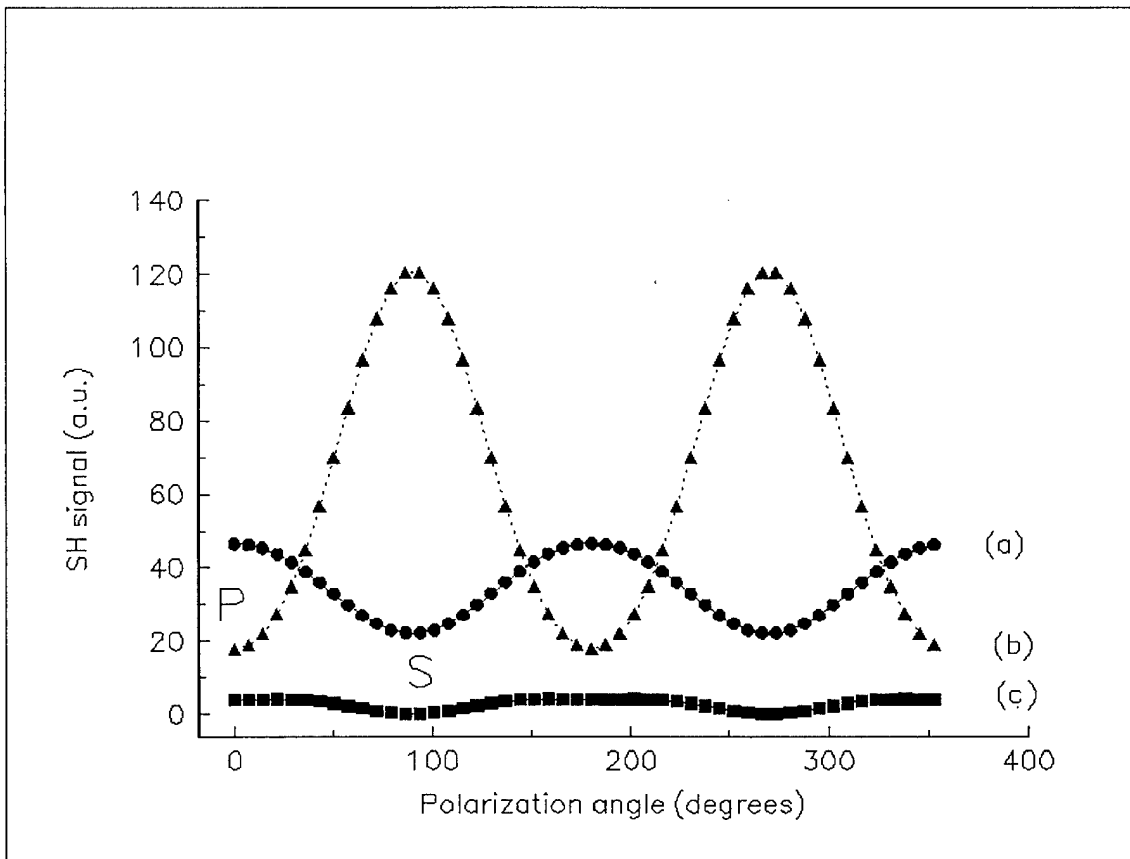
Figure 9. Theoretical near-field SH signal dependencies on the polarization angle of fundamental light obtained for strained BST films in the geometry similar to (a), (b) and (c) in Fig.4, where the arrows represent the direction of strain in the film. The field enhancement factor is assumed to be $\gamma = 4$ and the incidence angle $\alpha = 50^{\circ}$.
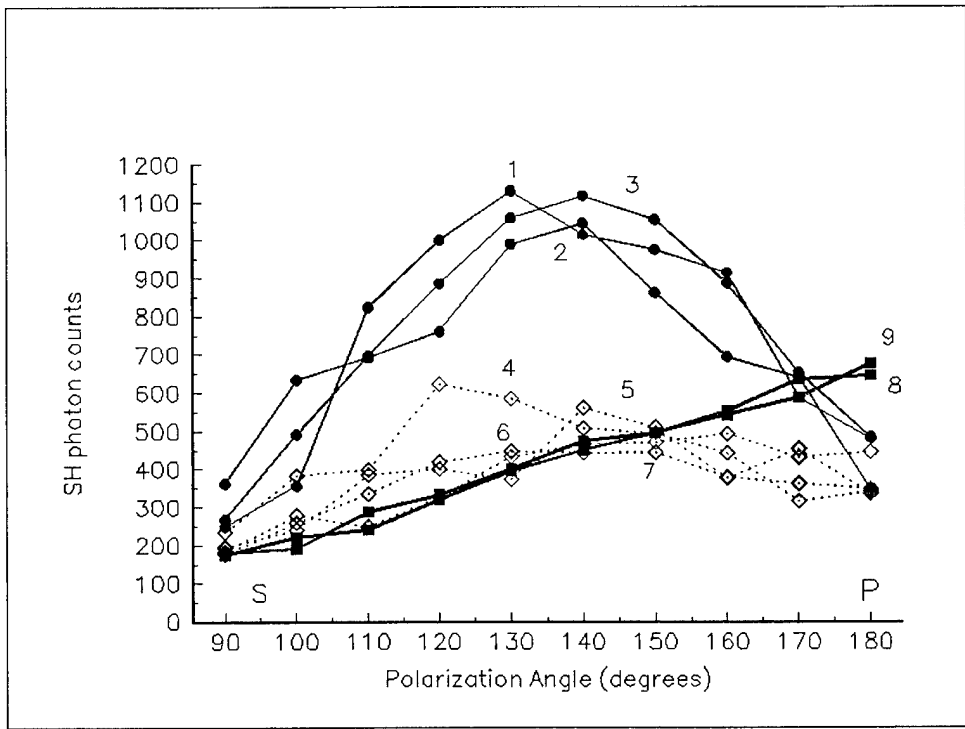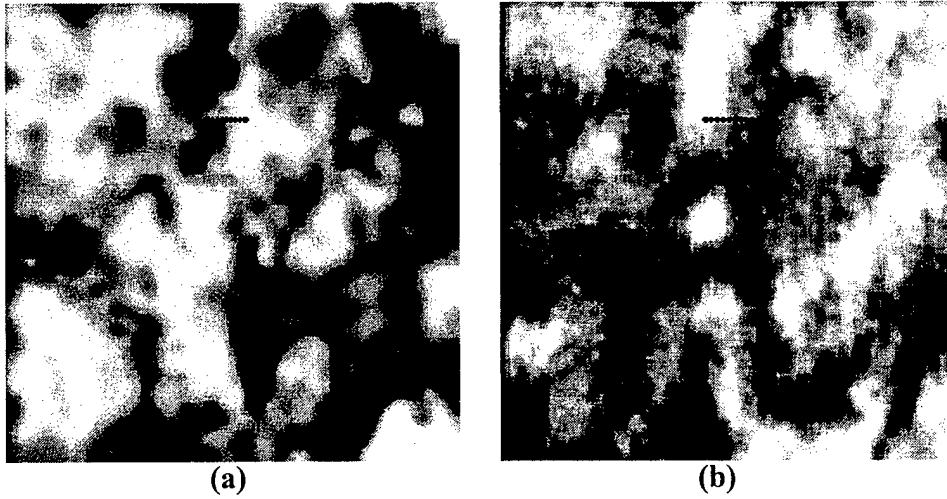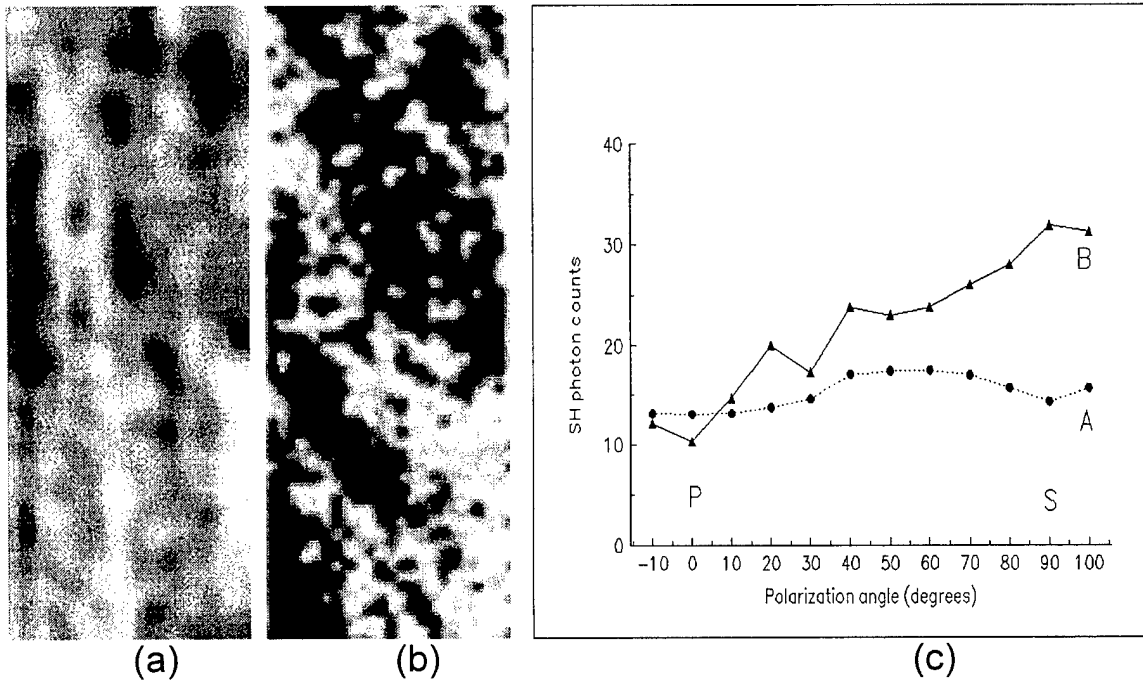
Figure 10. Simultaneously measured (a) topographical and SH near-field optical image (b) of a BST film. 2.2 μm by 0.9 μm images were obtained using S- polarized excitation light. Height variation within the topographical image is 50 nm. (c) Typical near-field SH signal dependencies on the polarization angle of the fundamental light measured over a thin BST film. Curve B was measured in the middle point of the SH image (b). Curve A was measured over the same area of the film after the sample had been rotated by 90°.

CITED REFERENCES

[1] J.F. McGilp, Progr. Surf.Sci. 49, 1 (1995).
[2] V. Kirilyuk, A. Kirilyuk, and Th.Rasing, Appl. Phys. Lett. 70, 2306 (1997).
[3] C. Ohlhoff, G. Lupke, C. Meyer, and H. Kurz, Phys .Rev. B 55, 4596 (1997).
[4] O. Auciello, J.F. Scott, and R. Ramesh, Physics Today, N7, 22-27 (1998).
[5] I.I. Smolyaninov, A.V. Zayats, and C.C. Davis, Phys. Rev.B 56, 9290 (1997);
I.I. Smolyaninov, C.H. Lee, and C.C. Davis, Appl. Phys. Lett. 74, 1942 (1999).
[6] S.I. Bozhevolnyi, B. Vohnsen, and K. Pedersen, Opt. Commun. 150, 49 (1998).
[7] D. Jakubczyk, Y. Shen, M. Lal, C. Friend, K.S. Kim, J. Swiatkiewicz, and P.N. Prasad, Opt. Letters 24, 1151 (1999).
[8] E. Betzig and J.K. Trautman, Science 257, 189 (1992).
[9] F. Zenhausern, M.P. O'Boyle, H.K. Wickramasinghe, Appl. Phys. Lett. 65, 1623 (1994).
[10] L.D. Rotter, D.L. Kaiser, and M.D. Vaudin, Appl. Phys. Lett. 68, 310 (1996).
[11] I.I. Smolyaninov, C.H. Lee, and C.C. Davis, Phys. Rev. Lett. 83, 2429 (1999).
[12] J.I. Gersten, A. Nitzan, J. Chem. Phys. 73, 3023 (1980).
[13] Y. Kawata, C. Xu, and W. Denk, J. Applied Phys. 85, 1294 (1999).
[14] F. Zernike and J.E. Midwinter, Applied Nonlinear Optics (Wiley, New York, 1973).
[15] L. Novotny, D.W. Pohl, and B. Hecht, Ultramicroscopy 61, 1 (1995).
[16] CRC handbook of lasers with selected data on optical technology, R.J. Pressley, ed. (The CRC, Cleveland, OH, 1971) p.513.
[17] S. Singh, J.P. Remeika, and J.R. Potopowicz, "Nonlinear optical susceptibilities of ferroelectric lead titanate", OSA Spring Meeting, Tuscon, AZ, April 1971.
[18] M. Tyunina, J. Wittborn, K.V. Rao, J. Levoska, S. Leppavuori, and A. Sternberg, Appl. Phys. Lett. 74, 3191 (1999).
[19] U.C. Oh, J. Ma, G.K.L. Wong, J.B. Ketterson, and J.H. Je, Appl. Phys. Lett. 76, 1461 (2000).
[20] I.I. Smolyaninov, A.V. Zayats, and C.C. Davis, "Near-Field Second-Harmonic Imaging of Ferromagnetic and Ferroelectric Materials Opt. Lett. 22, 1592-1594

Publications Arising from Research Supported by the Contract

Refereed Journal Articles

1. Walid A. Atia and Christopher C. Davis, "A Phase-Locked Shear-Force Microscope for Distance Regulation in Near-Field Optical Microscopy," Applied Physics Letters 70, 405-407, 1997.
2. Richard B. Wagreich and Christopher C. Davis, "Accurate Magneto-Optic Sensitivity Measurements of Some Diamagnetic Glasses and Ferrimagnetic Bulk Crystals Using Small Applied AC Magnetic Fields," IEEE Transactions on Magnetics 33, 2356-2361, 1997.
3. Igor I. Smolyaninov, David L. Mazzoni, Joseph Mait, and Christopher C. Davis, "Experimental Study of Surface-Plasmon Scattering by Individual Surface Defects," Phys. Rev. B 56, 1601-1611, 1997.
4. Igor I. Smolyaninov, Anatoly V. Zayats, and Christopher C. Davis, "Near-Field Second-Harmonic Imaging of Ferromagnetic and Ferroelectric Materials, " Optics Letters 22, 1592-1594, 1997.
5. Walid A. Atia, Saeed Pilevar, Ali Gungor, and Christopher C. Davis, On the Spatial Resolution of Uncoated Fiber Probes in Internal Reflection Near-Field Scanning Optical Microscopy," Ultramicroscopy 71, 379-382, 1998.
6. Saeed Pilevar, Walid A. Atia, and Christopher C. Davis, "An Experimental Technique for Characterizing Near-Field Optical Fiber Probes," to appear in Ultramicroscopy.
7. I.I. Smolyaninov, W.A. Atia, S. Pilevar, and C.C. Davis, "Experimental Study of Probe-Surface Interaction in Near-Field Optical Microscopy, Ultramicroscopy 71, 177-182, 1998.
8. Igor I. Smolyaninov, Anatoly V. Zayats, and Christopher C. Davis, "Near-Field Second Harmonic Generation from a Rough Metal Surface," Phys. Rev. B 56, 9290-9293, 1997.
9. Saeed Pilevar, Klaus Edinger, Walid Atia, Igor Smolyaninov, and Christopher Davis, "Focused Ion Beam Fabrication of Fiber Probes with Well-Defined Apertures for Use in Near-Field Scanning Optical Microscopy," Applied Physics Letter 72, 3133-3135, 1998.
10. Igor I. Smolyaninov and Christopher C. Davis, "On the Apparent Superresolution in Near-Field Optical Imaging of Periodic Gratings," Optics Letters 23, 1346-1347, 1998.
11. Igor I. Smolyaninov. Walid A. Atia, and Christopher C. Davis, "Near-Field Optical Microscopy of Two-Dimensional Photonic and Plasmonic Crystals," Physical Review B 59, 2454-2460, 1999.
12. Igor I. Smolyaninov, Chi H. Lee, and Christopher C. Davis "Near-Field Second Harmonic Imaging of Lead Zirconate Titanate Piezoceramic," Appl. Phys. Lett. 74, 1942-1944, 1999.
13. Igor I. Smolyaninov and Christopher C. Davis, "Near-Field Optical Study of Photorefractive Surface Waves in $BaTiO_3$," Optics Letters 24, 1367-1369, 1999.
14. Igor I. Smolyaninov, Chi H. Lee, and Christopher C. Davis, "Giant Enhancement of Surface Second Harmonic Generation in $BaTiO_3$ due to Photorefractive Surface Wave Excitation," Physical Review Letters 83, 2429-2432, 1999..
15. I.I. Smolyaninov, C.H. Lee, and C.C. Davis "Near-Field Microscopy of Second Harmonic Generation, Proc. SPIE 3666, 626-629, 1999.
16. Igor I. Smolyaninov, Chi H. Lee, and Christopher C. Davis "Near-Field Second Harmonic Imaging of Lead Zirconate Titanate Piezoceramic," J. Microscopy 194, 426-433, 1999
17 A.V. Zayats, I.I. Smolyaninov, and C.C. Davis "Near-Field Microscopy of Second-Harmonic Generation," Proc. SPIE 3732, 81-92, 1999.
18. A.V. Zayats, I.I. Smolyaninov, and C.C. Davis, "Observation of Localized Plasmonic Excitations at Thin Metal Films with Near-Field Second Harmonic Microscopy," Opt. Commun. 169, 93-96, 1999.
19. I.I. Smolyaninov, C.H. Lee, C.C. Davis and S. Rudin, "Near-Field Imaging of Surface-Enhanced Second Harmonic Generation, J. Microscopy 194, 532-536, 2000
20 I.I. Smolyaninov, H.Y. Liang, C.H. Lee, C.C. Davis, S. Aggarwal, and R. Ramesh, "Near-Field Second-Harmonic Microscopy of Thin Ferroelectric Films," Opt. Lett. 25, 1-3, 2000.
21. I.I. Smolyaninov, H.Y. Liang, C.H. Lee, C.C. Davis, V. Nagarjan, and R. Ramesh, "Near-field second harmonic imaging of the c/a/c/a polydomain structure of epitaxial $PbZr_xTi_{1-x}O_3$ films.to be published in the Journal of Microscopy.
22. I.I. Smolyaninov, H.Y. Liang, C.H. Lee, and C.C. Davis, "Nanometer scale crystal and strain analysis using near-field optical second harmonic microscopy: application to thin ferroelectric films," to be published in the Journal of Applied Physics.

Conference Presentations

1. W.A. Atia, S. Pilevar, B. Gopalan, P. Heim, M. Dagenais, and C.C. Davis, "Near-Field Scanning Optical Microscopy Analysis of the Near and Far-Field Intensity Distribution of Semiconductor Laser Diodes," paper presented at CLEO '96, Anaheim, California, June 2-7, 1996
2. I.I. Smolyaninov, D.L. Mazzoni, and C.C. Davis, "Direct Write Gold and Silicon Ablation on a 100nm Scale," paper presented at CLEO '96, Anaheim, California, June 2-7, 1996
3. Walid Ali Atia, Saeed Pilevar," Ali Gungor, and Christopher C. Davis, "On the Spatial Resolution of Uncoated Optical Fiber Probes in Internal Reflection Near-Field Scanning Optical Microscopy," paper presented at the Fourth International Conference on Near-Field Optics, Jerusalem, Israel, Feb. 9-13, 1997.
4. Saeed Pilevar, Walid Ali Atia, and Christopher C. Davis," "An Experimental Near-Field Technique for Characterizing Near-Field Optical Fiber Probes," paper presented at the Fourth International Conference on Near-Field Optics, Jerusalem, Israel, Feb. 9-13, 1997.
5. Walid A. Atia, Saeed Pilevar, and Christopher C. Davis, "Piezoelectric Tuning Fork Force Sensing of Optical Fiber Cantilevers," paper presented at the Fourth Workshop on Industrial Applications of Scanned Probe Microscopy, NIST, Gaithersburg, Maryland
6. Igor I. Smolyaninov, Anatoly V. Zayats, and Christopher C. Davis, "Mapping of Piezoelectric Ceramic Poling Using a Near-Field Optical Microscope," paper presented at the Fourth Workshop on Industrial Applications of Scanned Probe Microscopy, NIST, Gaithersburg, Maryland
7. I.I. Smolyaninov, and C.C. Davis "Confined Surface Plasmon Beams Produced by Surface Defects: Potential for Novel Sensor Applications," paper presented at CLEO '97, Baltimore, Maryland, May 18-23, 1997.
8. Christopher C. Davis, "Fiber Near-Field Microscopy," invited plenary address at the 12th International Conference on Optical Fiber Sensors, Williamsburg, Virginia, October 228-31, 1997. Published in the Conference Technical Digest, Vol 16, OSA Technical Digest Series, (Optical Society of America, Washington, DC, 1997, pp 8-12. ISBN 1-55752-514-5.
9. Igor I. Smolyaninov, A.V. Zayats, and Christopher C. Davis, "Near-Field Optical Microscopy of Surface Second Harmonic Generation, paper presented aat LEOS '97, San Francisco, California, 10-13 November, 1998.
10. I.I. Smolyaninov, C.H. Lee, C.C. Davis, and A.V. Zayats, "Near-Field Optical Microscopy of Surface Second Harmonic Generation" paper presented at the 1998 March Meeting of the American Physical Society, Los Angeles, California, March 16-20, 1998. Abstract in Bull. Am. Phys. Soc., 43, 481, 1998.
11. I.I. Smolyaninov, C.H. Lee and C.C. Davis, "Near-field optical study of second harmonic generation in piezoelectric ceramics," paper presented at the OSA Annual Meeting/ILS XIV, October 1998, Baltimore, Maryland.
12. Anatoly V. Zayats, Igor I. Smolyaninov, and Christopher C. Davis, "Near-Field Microscopy of Second-Harmonic Generation," paper presented at the XVI International Conference on Coherent and Nonlinear Optics, Moscow, Russia, 29 June - 3 July, 1998.
13. Igor I Smolyaninov, Chi H. Lee, and Christopher C. Davis, "Near-Field Second Harmonic Imaging of Lead Zirconate Titanate Piezoceramic," paper presented at NFO-5, Shirahama, Japan, December 6-10, 1998. Technical Digest of the 5th International Conference on Near-Field Optics (Shirahama, 1998), p66.
14. Andre Scherz, Walid Atia, and Christopher C. Davis, "DSP Controlled Fast Tracking Near-Field Scanning Optical Microscope," paper presented at NFO-5, Shirahama, Japan, December 6-10, 1998. Technical Digest of the 5th International Conference on Near-Field Optics (Shirahama, 1998), p117.
15. Igor I Smolyaninov, Chi H. Lee, and Christopher C. Davis, "Near-Field Imaging of Surface Enhanced Second Harmonic Generation," paper presented at NFO-5, Shirahama, Japan, December 6-10, 1998. Technical Digest of the 5th International Conference on Near-Field Optics (Shirahama, 1998), p393.
16 Igor I Smolyaninov, Walid Atia, and Christopher C. Davis, "Near-Field Microscopy Imaging of Two-Dimensional Photonic and Plasmonic Crystals," paper presented at NFO-5, Shirahama, Japan, December 6-10, 1998. Technical Digest of the 5th International Conference on Near-Field Optics (Shirahama, 1998), p471.
17. Igor I. Smolyaninov, Chi H. Lee, and Christopher C. Davis, "Near-Field Microscopy of Second Harmonic Generation," paper presented at Photonics 98, New Delhi, India, December 14-18, 1998. Conference Digest published by Viva Books Private Limited, New Delhi, Anurag Sharma and Ajoy Ghatak, Editors, ISBN 81-7649-073-3 (Three Volumes.)

18. Christopher C. Davis, "Resolution in near-field optical interactions involving bare tapered optical fibers," paper presented at CLEO '99, Baltimore, Maryland, May 23-28, 1999.

19. Saeed Pilevar, Klaus Edinger, Igor Smolyaninov, Christopher C. Davis, and Walid Atia, "Near-field scanning optical microscopy probe fabrication using focused ion-beam milling techniques," paper presented at CLEO '99, Baltimore, Maryland, May 23-28, 1999. OSA Technical Digest (OSA, Washington, DC), pp. 68-69.

20. Igor I. Smolyaninov, Chi H. Lee, and Christopher C. Davis, "Near-field second harmonic imaging of lead zirconate titanate piezoceramic," paper presented at QELS '99, Baltimore, Maryland, May 23-28, 1999. OSA Technical Digest (OSA Washington, DC), p 117.

21. I.I. Smolyaninov, H.Y. Liang, C.H. Lee, C.C. Davis, L.D. Rotter, and D.L. Kaiser, "Near-field second harmonic microscopy of thin ferroelectric films," paper presented at the MRS 1999 Fall Meeting, November 1999, Boston, Massachussetts. Published in the Mat. Res. Soc. Symp. Proc. Vol 596. pp 333-338, 2000

22. I.I. Smolyaninonv, H.Y. Liang, C.H. Lee, C.C. Davis, S. Aggarwal, and R.Ramesh, "Near-Field Second Harmonic Microscopy of Thin Ferroelectric Films," paper presented at CLEO/QELS 2000, San Francisco, California, May 7-12, 2000.

23. I.I. Smolyaninonv, C.H. Lee, and C.C. Davis, "Giant Enhancement of Surface Second Harmonic Generation in $BaTiO_3$ due to photorefractive surface wave excitation," paper presented at CLEO/QELS 2000, San Francisco, California, May 7-12, 2000.

Principal Personnel at the University of Maryland Working on Research Connected with the Contract (Most were not financially supported by this contract)

Professor Christopher C. Davis: Project Director

Professor Chi Lee: Expert on short pulse optical techniques and nonlinear phenomena

Dr. Igor I. Smolyaninov: Assistant Research Scientist. Dr. Smolyaninov provided key expertise in acquiring and interpreting nonlinear near-field images of surfaces.

Dr. Saeed Pilevar: An Assistant Research Scientist (now with Gould Fiber Optics), who provided fiber tip fabrication expertise.

Professor Ali Gungor: A visitor from Uludag University in Bursa, Turkey

Dr. Joe Mait: A visiting scientist on sabbatical from the Army Research Laboratory in Adelphi, Maryland

Dr. Sergei Rudin: Visitng researcher from the Army Research Laboratory in Adelphi, Maryland. Helped with the theoretical interpretation of nonlinear images.

Dr. Anatoly Zayats: A postdoctoral Research Associate

Dr. Klaus Edinger: A postdoctoral Research Associate who helped with ion-beam fabrication of special NSOM fiber tips.

Walid Atia: Graduate Research Assistant. Walid Atia received the Ph.D. during the period of the contract and joined MIT Lincoln Laboratory. His thesis was entitled "Near-Field Scanning Optical Microscopy: Theory, Design, and Applications."

Andre Scherz: Graduate research Assistant, working towards the Ph.D. degree on fast scanning and control schemes for NSOM.

Hongye Liang: A Graduate Research Assistant working towards the Ph.D. degree on time-resolved nonlinear near-field studies for domain dynamics

APPENDICES

Copies of some key journal articles published during the contract period.

A phase-locked shear-force microscope for distance regulation in near-field optical microscopy

Walid A. Atia and Christopher C. Davis[a]

Electrical Engineering Department, University of Maryland, College Park, Maryland 20742

A nonoptical phase-locked shear-force microscope utilizing a quartz crystal tuning fork acting as a voltage-controlled oscillator in a phase-locked loop has been implemented. A tapered optical fiber is rigidly mounted on one of the prongs of the fork to serve as both a shear-force pickup and a near-field optical probe. The crystal is driven at its resonance frequency through positive feedback of the monitored current through the crystal. This signal is used as the voltage-controlled oscillator in a phase-locked loop. The scheme allows for scan speeds far beyond the Q-limited amplitude sensor bandwidth and exhibits excellent sensitivity for a high-Q resonator. Furthermore, given the small vibration amplitude of the tip (<0.5 nm) and the distance over which it is reduced (>6 nm), it is unlikely that the tip is making direct contact with the sample surface as has been suggested for the optical shear-force detection scheme. © *1997 American Institute of Physics.*
[S0003-6951(97)01204-7]

Shear-force microscopy[1,2] has been the method of choice for distance regulation in near-field scanning optical microscopy,[3] allowing one to simultaneously maintain the aperture within the near-field of the sample and obtain a topographical map of the sample surface. To date, the most popular implementation of shear-force microscopy involves vibrating an optical fiber probe at its resonance frequency in a direction lateral to the sample surface, and optically monitoring the vibration amplitude. This amplitude decreases as the tip approaches some tens of nanometers from the sample surface. The mechanism for this amplitude reduction is still not well understood. Recently, however, Gregor *et al.*[4] have proposed that the damping is simply due to the tip edge lightly contacting the sample in a manner similar to tapping-mode atomic force microscopy.[5] They propose that as the tip makes contact with the surface, it exhibits a new compliance term because the very end of the tip is pressing against the sample surface. As this excess compliance results only when the tip is in contact with the sample, which occurs over a small fraction of the pendulum-like trajectory of the fiber tip, the differential equation that describes the tip-sample interaction is nonlinear and depends on the tip-sample geometry. An alternative, nonoptical distance regulation scheme described by Karrai and Grober[6] involves the use of a quartz crystal tuning fork to sense the force exerted on a fiber tip glued to one of the arms of the fork. Because the typical vibration amplitude of the fork is very small (<0.5 nm[6]) compared to that required for optical shear-force detection (typically tens of nanometers,[4]) the tip-sample angle would have to be unrealistically large for the measured crystal approach curves[6] to be consistent with the surface contact model.[4] Specifically, the surface contact model would suggest that $\alpha = \tan^{-1}(0.5 \text{ nm}/d)$, where α is the tip-sample angle and d is the distance from which the tip amplitude starts to reduce to where it is reduced to zero by complete tip contact, a distance $d \gtrsim 10$ nm measured in Ref. 6 would yield an unrealistically small tip-sample angle $\alpha < 3°$ (i.e., the tip would have to be nearly parallel to the sample surface). A

more likely explanation is that the tuning fork scheme involves a lateral force exerted on the tip before tip contact, possibly caused by interaction with a surface contamination layer. Gregor *et al.*[4] acknowledged that over "larger separations," an interaction before surface contact may occur, and the tuning fork scheme, with a force sensitivity of less than 1 nN,[6] is an ideal detector to probe such interactions.

One limitation of the tuning fork scheme is its scan speed. This results from the extremely high Q of the tuning fork, which allows it to be used as a sensitive force detector despite its stiff spring constant (typically 20 000 N/m), but limits the transient *amplitude* response to a time constant of $\tau = 2Q\sqrt{3}/\omega_0$, where Q and ω_0 are the measured quality factor (at full width half maximum) and resonance frequency of the crystal with the fiber attached, respectively. For typical values of $Q = 1000$ and $\omega_0 = (2\pi)33\,000$ rad/s, this yields a time constant of $\tau = 17$ ms, which implies a rather large settling time (to 1%) of $5\tau = 85$ ms. In a conventional servo loop, one cannot increase the bandwidth much beyond that of the slowest system element (either actuator or sensor). Furthermore, if the fork were operated in a vacuum, then Q would typically increase by a factor of 10, yielding an unreasonably large settling time that would make the maximum scanning speed unacceptably slow for most applications.[7]

In order to overcome this limitation, we have implemented a frequency modulation/demodulation scheme similar to that used for high-Q cantilevers in atomic force microscopy.[7] Conceptually, if the shear force mechanism is not purely dissipative, as suggested previously,[6] but also includes a conservative component that changes the effective compliance of the cantilever, then the resonance frequency of the cantilever will change instantaneously independent of the cantilever Q as the tip approaches the sample. A higher Q would simply increase the signal-to-noise ratio (S/N) for observation of the resonance frequency.[7] A significant compliance change would be expected if the shear force mechanism results from the very end of the tip pressing against the sample,[4] or against the sample's contamination layer. In order to facilitate frequency modulation, the tuning fork was

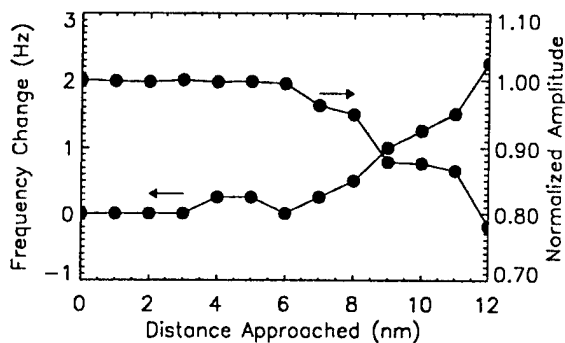[a] Electronic mail: davis@eng.umd.edu

FIG. 1. Simultaneous amplitude and frequency deviation of the quartz crystal oscillator upon approach to the sample. Within 6 nm from the interaction area, the amplitude decays by over 20% while the frequency increases by 2.3 Hz. The center frequency $f_0 = 33,089$ kHz with $Q = 2100$.

driven at its resonance frequency by sampling the current through it and positively feeding back this signal into the crystal, as is commonly done in conventional crystal oscillator circuits.[8] As the resonance frequency of the cantilever is $\omega_0^2 = k/m$, where k is its effective spring constant and m is the effective mass of the cantilever, any variations of k or m will result in an instantaneous resonance frequency change. If we consider the amplitude reduction upon approach to result from a change in viscosity,[6] then the resonance frequency, within the framework of a simple harmonic oscillator model, would decrease slightly given the initial large Q. However, as plotted in Fig. 1, we have experimentally observed an *increase* in the resonance frequency of the oscillator upon approach of over 2 Hz, suggesting a phenomenological repulsive lateral force gradient $\partial F/\partial x \approx 2$ N/m for a center frequency $f_0 = 33$ kHz[9] (the tip was vibrating with an amplitude of 0.47 nm during the approach). This finding, together with the unrealistic tip-sample geometry needed for tapping-induced damping[4] suggests that both the simple harmonic oscillator model and the direct contact nonlinear bending force model fail to adequately describe the shear force mechanism.

Because the frequency shift upon approach is small ($< 0.01\%$), a simple frequency demodulator, for example a phase-locked loop integrated circuit or digital frequency counter, could not be used and provide the required bandwidth. Therefore, we employ the phase difference between a reference signal and the oscillator signal from the monitored current of the tuning fork to demodulate the frequency shift in a phase-locked loop (PLL) configuration.[10] A similar scheme for an atomic force microscope cantilever was demonstrated by Kikukawa et al.[11] Since frequency is the derivative of phase, a variation of 1 Hz between the reference and oscillator frequency manifests itself as a 1 Hz sinusoidal signal at the output of the phase detector. This signal readily serves as an error signal in a PLL arrangement where the voltage-controlled oscillator (VCO) incorporates the piezo controlling the tip-sample distance of the fork. A schematic diagram of the shear force PLL is shown in Fig. 2. The error signal is the dc output of the phase detector. It is a null when the tip-sample distance causes the fork oscillation frequency to be exactly equal to that of the reference signal and simul-
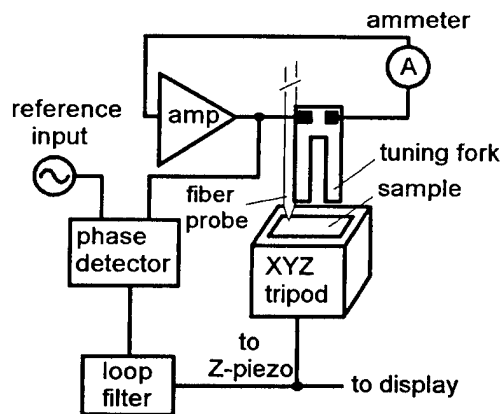

FIG. 2. Schematic diagram of the phase-locked shear-force microscope. The current through the quartz crystal is converted to a voltage and is then positively fed back to the crystal to form an oscillator that tracks the resonance frequency of the fiber-crystal system. This frequency shift is demodulated by means of a phase detector whose reference input is set by the user to the frequency deviation for a given tip-sample height. The loop filter's output is then sent into the z-piezo where a zero error signal condition is obtained when the tip-sample separation causes the oscillator frequency to equal the reference frequency.

taneously $90°$ out of phase. The experimentally measured closed-loop frequency response for a crystal with $Q = 2100$ along with a theoretical curve based on a modeling of the phase-locked loop and piezo stage is shown in Fig. 3, yielding a bandwidth of over 70 Hz (defined at which the output is attenuated to a factor of 0.707 times the input relative to the zero-frequency gain[12]). This defined bandwidth is also inversely proportional to the loop's settling time for the transient to decay to its steady state value to within 1%, thus facilitating direct comparison with the amplitude settling time of the tuning fork. For the crystal used to produce Fig. 3, the theoretical settling time of $5\tau = 10Q\sqrt{3}/\omega_0 = 175$ ms (for $Q = 2100$, $\omega_0 = 2\pi \cdot 33089$ rad/s), which has an amplitude response bandwidth of 5.7 Hz. Thus, the experimentally attained bandwidth of 70 Hz is over an order of magnitude faster than that obtainable by amplitude detection. Fig. 4 shows a scan of a 500 nm period diffraction grating taken
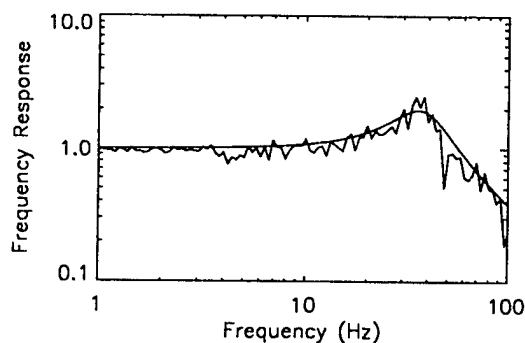

FIG. 3. The measured closed-loop frequency response plotted with a theoretical curve based on a control system analysis that models the piezo response, loop filter, and crystal VCO. The bandwidth is over 70 Hz which exceeds the limit of 5.7 Hz imposed by amplitude detection for the measured $Q = 2100$ by over an order of magnitude. The noise spike near 50 Hz is due to the feedback compensated piezo stage.
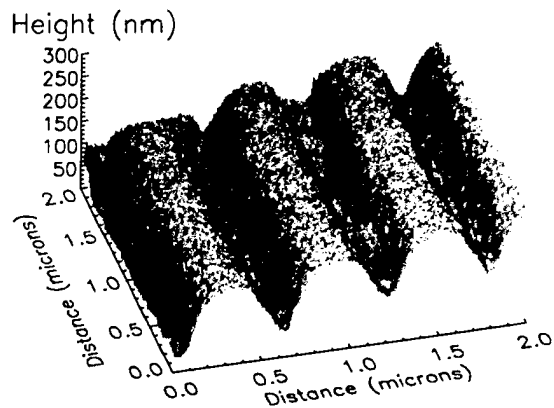
W. A. Atia and C. C. Davis

Height (nm)

FIG. 4. Shear-force image of a 500 nm period diffraction grating obtained with a frequency deviation of 1.5 Hz. The tip amplitude was 0.47 nm (interferometrically measured), the dither direction is perpendicular to the grating, there are 200 by 200 pixels, and the scan rate is (1/70 Hz)200=2.86 s/line. The noise in the image is less than 3 nm and is caused primarily by noise in the feedback compensated piezo stage.

with a frequency deviation of 1.5 Hz. The noise in the image was determined to be less than 3 nm, primarily due to noise in the feedback-compensated piezo stage (a Melles-Griot Nanoblock). The 300 Hz bandwidth of this stage limits the fastest possible scanning speed.

Besides faster response, there are additional benefits of the phase-locked shear-force microscope. There is no need for an external dither, resulting in a more compact and stable tip head. The crystal is made to automatically operate at resonance through self-oscillation, so it is essentially self-tuning and requires no time-consuming frequency sweeps to

find the resonance frequency. Because the scheme is based on frequency demodulation, it is immune from the usual dc drifts and noise associated with amplitude detection. Furthermore, the scheme is nonoptical, eliminating the problem of the large background radiation associated with optical shear-force control, and obviating the need for alignment of an external laser beam and detector. We have implemented the technique using both a bare glass fiber and an aluminum coated fiber with no observable difference in performance.

[1] E. Betzig, P. L. Finn, and J. S. Weiner, Appl. Phys. Lett. **60**, 2484 (1992).
[2] R. Toledo-Crow, P. Yang, Y. Chen, and M. Vaez-Iravani, Appl. Phys. Lett. **60**, 2957 (1992).
[3] E. Betzig, J. K. Trautman, T. D. Harris, J. S. Weiner, and R. L. Kostelak, Science **251**, 1468 (1991).
[4] M. J. Gregor, P. G. Blome, J. Schöfer, and R. G. Ulbrich, Appl. Phys. Lett. **68**, 307 (1996).
[5] Q. Zhong, D. Inniss, K. Kjoller, and V. B. Elings, Surf. Sci. Lett. **290**, L688 (1993).
[6] K. Karrai and R. D. Grober, Appl. Phys. Lett. **66**, 1842 (1995).
[7] T. R. Albrecht, P. Grütter, D. Horne, and D. Rugar, J. Appl. Phys. **69**, 668 (1991).
[8] R. Matthys, Crystal Oscillator Circuits (Wiley, New York, 1983).
[9] D. Sarid, in Scanning Force Microscopy (Oxford University Press, New York, 1991), Chap. 1.
[10] F. M. Gardner, Phaselock Techniques (Wiley, New York, 1979).
[11] A. Kikukawa, S. Hosaka, Y. Honda, and R. Imura, Jpn. J. Appl. Phys. 1 **33**, 1286 (1994).
[12] G. F. Franklin, J. D. Powell, and A. Emami-Naeini, in Feedback Control of Dynamic Systems (Addison-Wesley, Menlo Park, 1991).

Experimental study of surface-plasmon scattering by individual surface defects

Igor I. Smolyaninov and David L. Mazzoni
Electrical Engineering Department, University of Maryland, College Park, Maryland 20742

Joseph Mait
US Army Research Laboratory, AMSRL-SE-EO, 2800 Powder Mill Road, Adelphi, Maryland 20783

Christopher C. Davis
Electrical Engineering Department, University of Maryland, College Park, Maryland 20742
(Received 26 February 1997)

A direct-write ablation technique has been implemented in a photon scanning tunneling microscope setup. This combination allows us to study surface-plasmon (SP) scattering by *in situ* created individual surface defects, while the sizes and shapes of the defects are varied continuously. It is found that within a certain range of its size, a "hill" on an otherwise flat surface can be the source of a very narrow plasmon beam. This effect is explained using the Huygens-Fresnel principle. Shadowing and refraction of the SP field by smaller defects has also been observed. In order to explain these results we introduce an effective SP refractive index for two classes of surface defects: shallow topographical defects and areas covered with absorbed molecular layers. This concept allows us to achieve a qualitative understanding of plasmon scattering in many practical cases. Some simple optical elements for the control of SP propagation are suggested and demonstrated. Our observations suggest numerous practical applications in multichannel chemical sensing, biosensing, and integrated optics. [S0163-1829(97)05928-6]

I. INTRODUCTION

The surface plasmon (SP) is a fundamental electromagnetic excitation mode of a metal-dielectric interface.[1,2] The properties of SP's have been the subject of extensive studies because of their extreme sensitivity to surface roughness and the dielectric properties of surface absorbed layers. This sensitivity results from the exponential dependence of the SP electromagnetic field on the distance from the interface in each of the bounding media. The SP is free to propagate along the metal surface with a mean free path determined by the quality of the surface and Ohmic losses. If the surface is perfectly flat then Ohmic loss is the only channel for decay, since the momentum conservation law prohibits SP conversion into photons. In the visible range the SP mean free path on a silver surface is limited to about 50 μm but can extend to many mm in the infrared region.[3] Similar waves exist on the surfaces of a number of dielectrics and semiconductors.[1] Since the properties of SP's depend strongly on the properties of the interface along which they propagate, they have found applications in the surface-roughness analysis,[1] gas detection, and biosensing.[4]

Until recently there was no tool for the direct study of SP propagation, since the SP field decay length perpendicular to the interface is on the order of 100 nm in the visible range. Indirect information about SP properties had been extracted from far-field measurements of light scattered into a free space by SP interaction with surface defects such as in surface-plasmon microscopy.[5] The development of scanning probe techniques has opened the way to a study of SP properties at the surface along which the SP propagates with resolution in the nanometer range. The scanning tunneling microscopy (STM) was the first such technique. In STM

experiments an additional tunneling current has been observed in the presence of the SP wave.[6] A closely related technique, in which the SP field scattered by a STM tip is detected in the far-field zone, has been introduced by Specht *et al.*[7] However, a metallic STM tip positioned within a fraction of a nanometer from the surface causes a very strong perturbation of the initial SP field distribution. The results of these experiments reflect the properties of localized plasmon modes[8] that develop between the STM tip and the sample rather than the unperturbed SP field distribution. Similarly an atomic force microscope (AFM) tip has been used to scatter the SP field.[9] Although less intrusive then STM, this technique also relies on the perturbation of the SP field as its sensitive mechanism. Kim *et al.* even refer to the potential benefits of a metal-coated AFM tip for obtaining an improvement in the sensitivity of this technique.[9]

The development of near-field optical microscopy[10] has created different ways for probing the SP field distribution. For example, in a tunneling near-field optical microscopy[11] light from a metal-coated optical fiber tip is used for SP excitation. However, the most successful experimental geometry for measuring the true unperturbed SP field distribution appears to be the photon scanning tunneling microscopy (PSTM).[12] In the PSTM geometry a fiber tip is used to detect the evanescent field of the light being totally internally reflected at the sample surface. In Ref. 13, PSTM was used to measure the exponential decay of the SP field away from a metal-air interface. SP propagation along the interface has also been studied[14] and the SP propagation length measured. SP's on both an external metal-air interface and an internal interface between a metal film and a glass substrate have been excited[15] and the SP field distribution for both modes has been mapped. Extension of SP studies to the control of
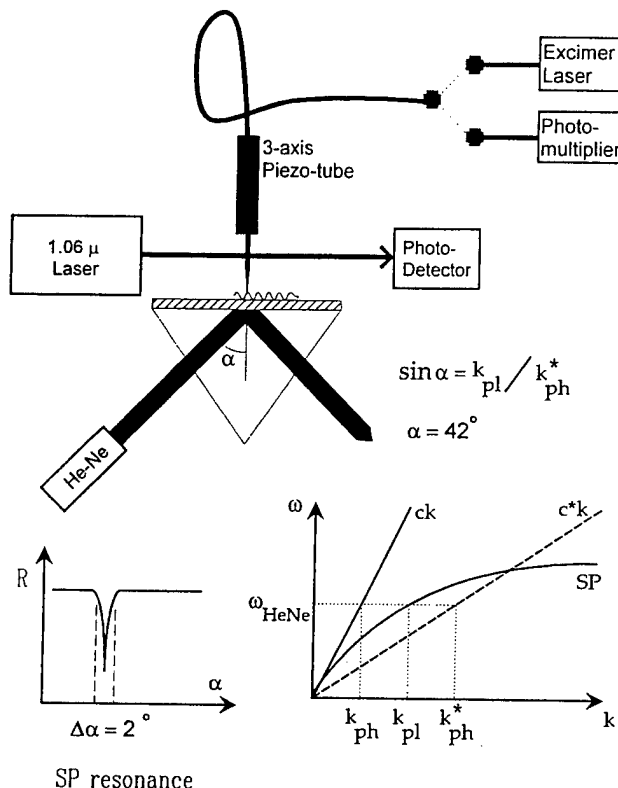
FIG. 1. Schematic view of the experimental setup. Dispersion curves for surface plasmons and photons in air and in glass are shown in the inset.

FIG. 3. Topography (a) and optical near-field distribution (b) around a crater created by a UV laser pulse at full energy.

SP's by two-dimensional optics is anticipated. This could create numerous applications in integrated optics and multichannel chemical sensing and biosensing. However, until recently there has been no attempt to create a real two-dimensional optical element for SP's.

Recently we studied the scattering of SP's by *in situ* created individual surface defects.[16] Some prototype two-dimensional optical elements able to control SP propagation were demonstrated. Using a combination of a PSTM with a direct-write lithography technique[17] we can create submicrometer size patterns on the surface of a metal film and measure the SP field redistribution caused by these patterns. An uncoated tapered optical fiber allows us to deliver sub-
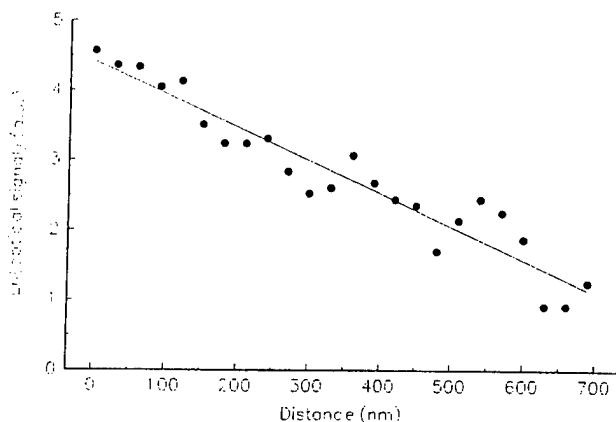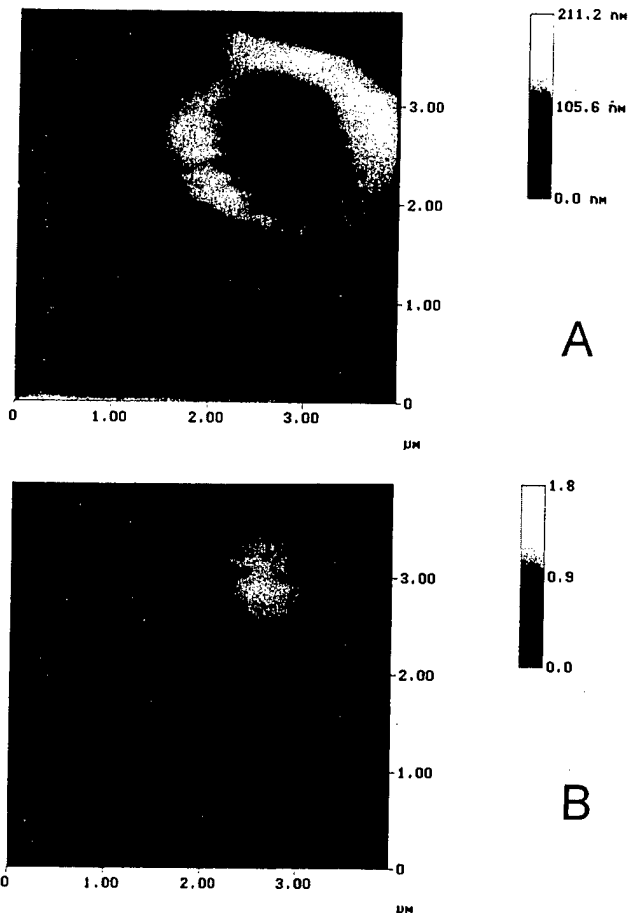
stantial light power into a diffraction-limited area of the sample near the tip. We are able to ablate submicrometer craters on virtually any opaque surface without damaging a transparent fiber tip. On the other hand, the resolution of our microscope in the PSTM mode depends strongly on the diameter of the uncoated fiber tip: it is not dominated by diffraction. An uncoated fiber tip introduces a relatively small perturbation into the SP field distribution, since the difference $\epsilon_{tip} - 1$ between the dielectric constant of the tip and a vacuum is much smaller than the difference between the dielectric constant of the tip and a metal (in the case of silver $\epsilon_{Ag} = -17.9 + 0.7i$ at $\lambda = 633$ nm). A comparison of theoretical and experimentally measured SP field distribution (discussed later in this paper) confirms this conclusion. All these facts make our experimental technique a very reliable tool for a study of the optics of SP's.

Below we discuss in detail our experimental setup and report experimental observations. In the discussion section we present some model calculations of the SP field distribution around simple defects and compare them with our observations. We present the design of some optical elements that could control SP propagation. Finally, some practical applications of these elements are suggested.

FIG. 2. Dependence of the optical signal on the tip-sample distance.

II. EXPERIMENTAL SETUP

In our experiment SP's are excited in an attenuated total reflection (ATR) arrangement[18] on the surface of an 80-nm-
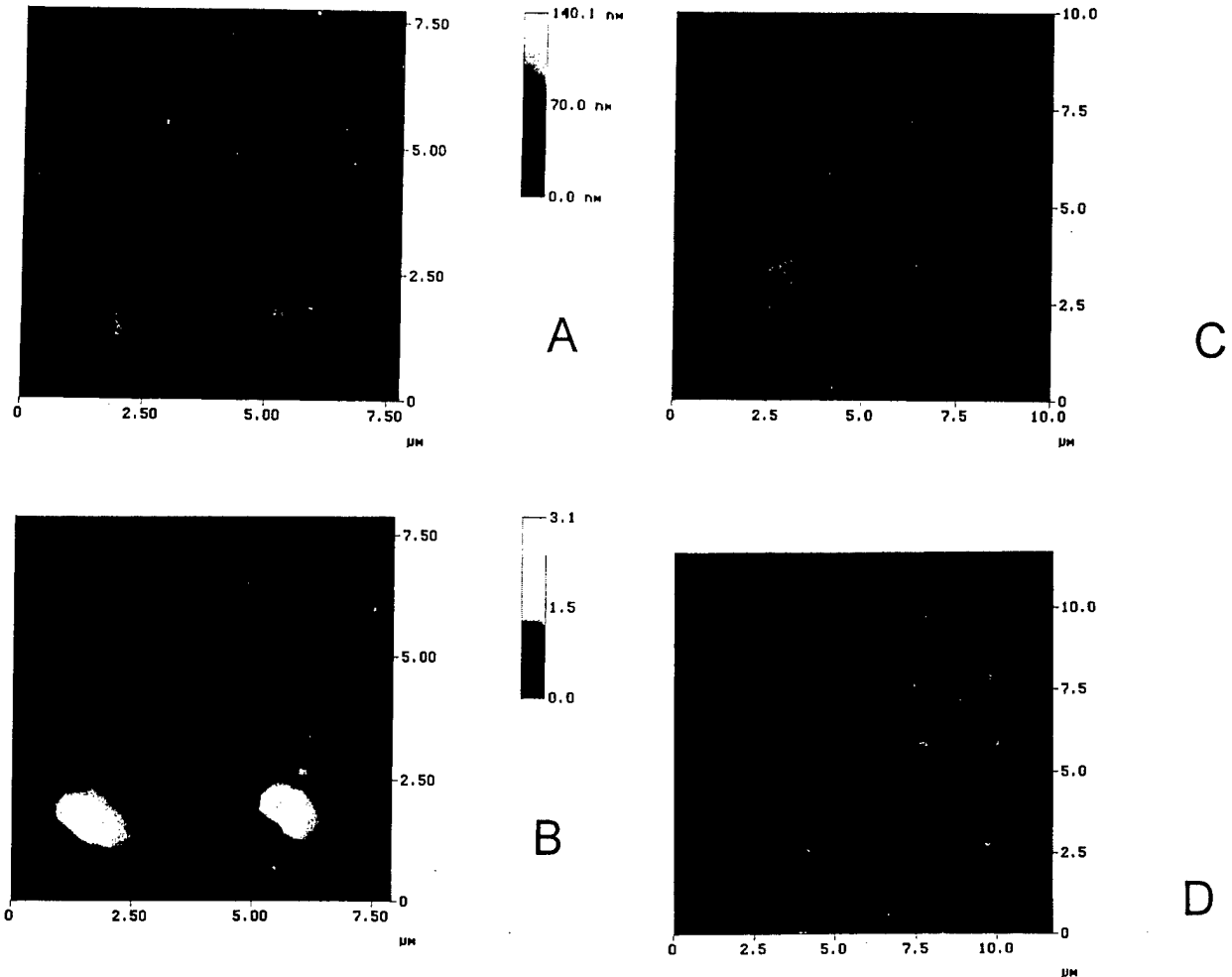
FIG. 4. Topography (a) and optical near-field distribution (b) around two plasmon "flashlight" structures. (c) and (d) are far-field images taken at distances 1 and 4 μm from the sample.

thick silver film evaporated onto the hypotenuse face of a right-angle glass prism (Fig. 1). An unfocused P-polarized HeNe laser beam is used for excitation of the SP's. Wave-vector matching to the SP mode at the silver-air interface is achieved when light is internally incident on the silver film at an angle $\alpha = \arcsin\{[\epsilon_{Ag}/(\epsilon_g\epsilon_{Ag}+\epsilon_g)]^{1/2}\} = 42°$, where ϵ_{Ag} and ϵ_g are the dielectric constants of silver and the glass prism (this value stems from the SP dispersion relation in the thick-film limit[14]). The thickness of the film is a little bit less than the decay length of the SP field into silver, so the coupling of fields between the top and bottom interfaces is sufficient for effective SP excitation. The SP local field is probed with an uncoated, adiabatically tapered fiber tip that is drawn at the end of 200-μm UV fiber by heating it with a CO_2 laser beam in a micropipette puller. The fiber tip can be scanned over the sample surface with a constant tip-surface distance ($\sim$5 nm) using shear force feedback as described elsewhere.[17] Therefore, surface topography can be imaged with a resolution on the nanometer scale, while simulta-neously allowing the recording of a near-field optical image corresponding to the distribution of the SP local-field inten-sity near the film surface. This configuration of a scanning probe microscope is usually called a PSTM.[12]

For the purpose of lithography the free end of the fiber can be connected to the output of a 248-nm excimer laser.

The laser power is easily attenuated in order to change the size of defects created in the film. The use of uncoated UV grade tapered fiber and nanosecond pulsed 248-nm excimer laser light allows us to deliver an estimated 200 GW/m^2 UV light power into a tip-sample region smaller then 200×200 nm^2 during a single laser pulse. This power is sufficient for local surface ablation of gold or silver and local melting of silicon without melting of the transparent UV fiber tip.[17] The topographic changes caused by UV irradiation are immedi-ately recorded by the shear force microscope. The developed technique is to some extent similar to STM lithography but is not restricted by the conductance of the sample surface.

III. EXPERIMENTAL RESULTS

The quality of the silver films used in our experiments was good enough to provide a quite homogeneous optical signal distribution over the unmodified surface areas. As a first step, we measured the optical signal dependence on the distance between the tip and the silver film (Fig. 2). The signal exhibits an exponential decay with distance increase: $\text{Ln}(I) = -2\alpha d$ superimposed on a small background. This background signal is due to the scattering of SP's into pho-tons over the entire illuminated film area. The value of the exponent ($\alpha = 1/416$ nm) is consistent with the angle of SP

FIG. 6. Cross section of the optical signal in the plasmon beam in Fig. 5(c).

propagate along the surface, so one can distinguish its contribution from the contribution of SP field scattering. It is important to mention that the contrast of each image is determined internally by scaling the difference between the maximum and minimum of the detected signals to the maximum number of gray levels in the image. A comparison between images therefore needs to be performed with care.
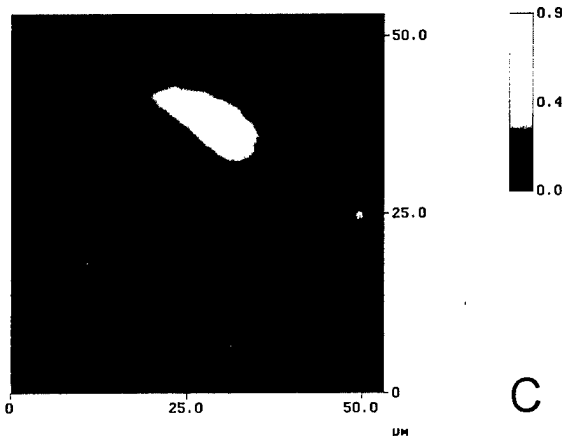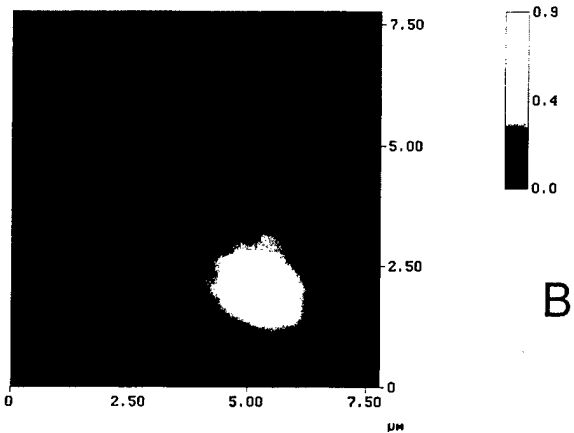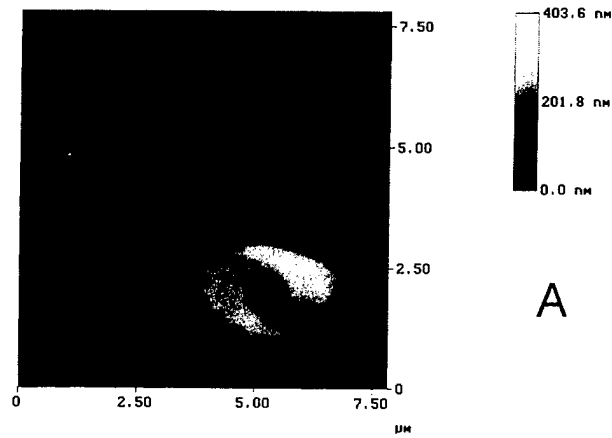
FIG. 5. More complicated defects emitting plasmon beams: topography (a) and optical near-field distribution (b) around an individual defect; (c) is a near-field distribution around a big defect.

excitation. According to theory, the SP field should decay into air with a decay constant $k_z = (k_x^2 - \omega^2/c^2)^{1/2} = 1/412$ nm, where k_x is the wave vector parallel to the surface.

Below we present images of the optical near-field around *in situ* created defects having different shapes and sizes. These images result from the scattering of the SP field by the defects. They also contain an evanescent component of the totally internally reflected HeNe laser beam used for the excitation of SP's. But this evanescent component does not
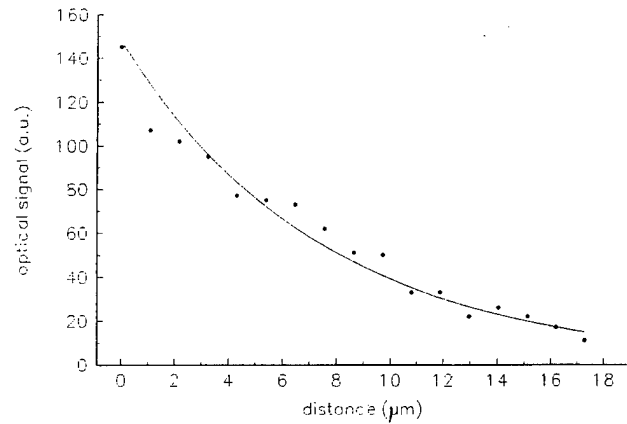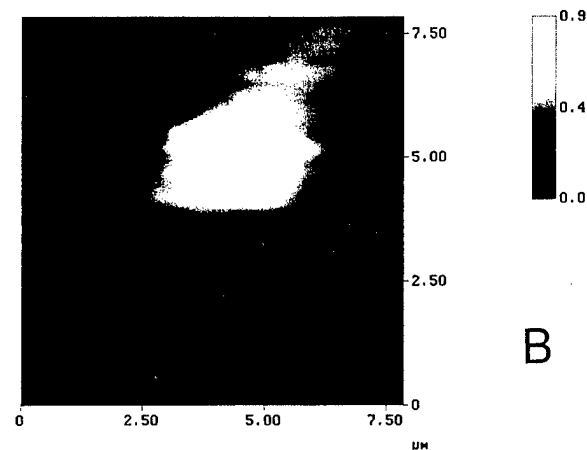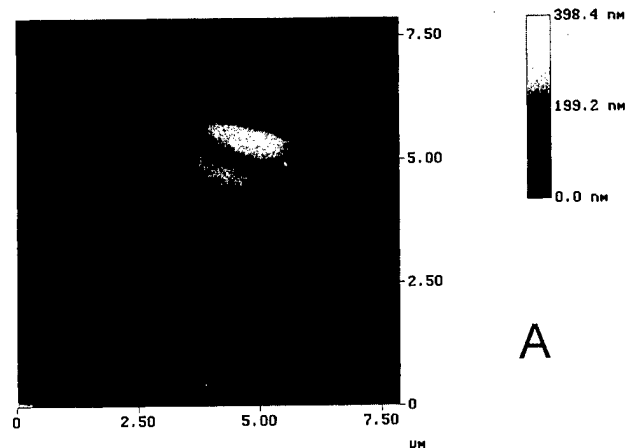
FIG. 7. Topography (a) and optical near-field distribution (b) around a surface defect emitting a weaker reflected plasmon beam. A stronger plasmon beam is emitted in the forward direction.
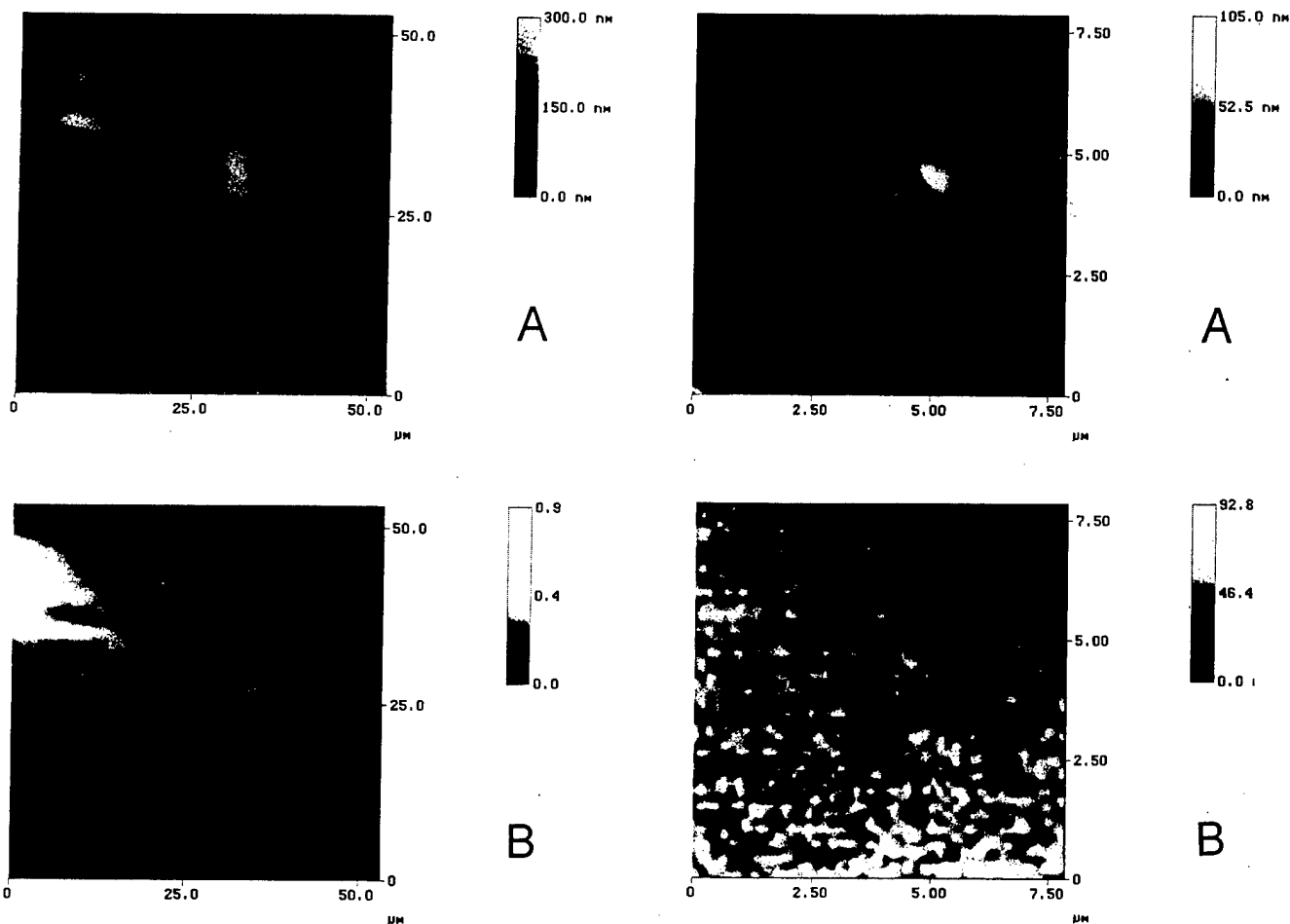
FIG. 8. Scattering of a plasmon beam emitted from a surface defect in the top left corner of the image by another surface defect. As usual, images (a) and (b) are the topography and the near-field distribution, respectively.

FIG. 9. Topography (a) and optical near-field distribution (b) around smaller defects created at around $\frac{1}{2}$ of the initial power. The direction of plasmon propagation is shown by the arrows. Shadows are seen behind the defects.

At maximum laser power (~ 1 nJ per pulse measured in the far field of the tip) a single nanosecond UV pulse delivered to the silver film surface by the uncoated tapered fiber was able to ablate a hole through the 80-nm-thick film. The topography of such a defect [Fig. 3(a)] looks like a large crater with an approximately 0.5-μm hole in the middle. The optical near-field distribution [Fig. 3(b)] has a strong maximum around the hole because the glass prism surface is almost clear of metal in the hole and we see the near field of the totally internally reflected HeNe laser beam used for the excitation of SP's. By attenuating the UV laser pulse power we are able to make craters of shallower depth and smaller diameter. At low power craters may even disappear and we observe a "hill" at the irradiated site. Such hills created at approximately $\frac{3}{4}$ of the initial power are shown in Fig. 4. Strong maxima of the optical near field are again seen around these hills. The surprising feature of the near-field image in Fig. 4(b) is the appearance of quite strong and narrow beams (their width is around 1 μm) shining from the hills in the direction determined by the HeNe laser beam used for SP excitation. These "beams" are localized within the surface. The near-field intensity seems not to change significantly along the 7-μm length of the left "beam" visible in the image. On the other hand, a far-field image taken 7

μm away from the surface is completely dark on the same half-tone scale. A number of images taken at intermediate distances show the spreading and exponential attenuation of the beam "brightness" with increasing distance from the surface. Some of them are shown in Figs. 4(c)–4(d). (Note, however, that the contrast for both images is internal and not relative to each other.) Evidently, in the near-field image [Fig. 4(b)] we see surface-plasmon beams shining from the peaks of the optical near-field around the hills. We like to call these structures plasmon "flashlights." Our experience shows that the appearance of a plasmon beam is a rather common features of an optical-field distribution near surface defects in the ATR geometry. In Fig. 5 one can see some other images showing plasmon beams. If the defect has a complicated shape as in Fig. 5(c) the plasmon beam can shine from some region of the defect. The cross section (Fig. 6) of the plasmon beam in this image shows the lateral exponential decay of the SP field intensity with the distance from the source of the beam. The value of the SP propaga-
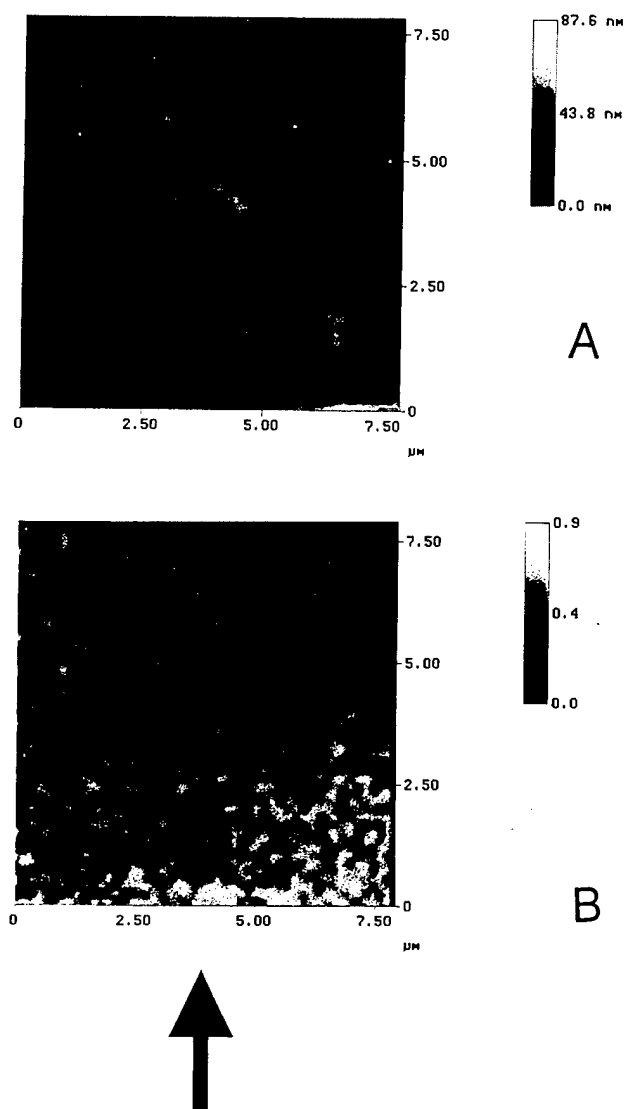
FIG. 10. Topography (a) and optical near-field distribution (b) around three surface defects.

tion length equals 9.1 μm in this case. This value is close to the 13.2-μm value reported in Ref. 14 yet is much smaller than the theoretically estimated propagation length 42.4 μm.[14] A possible explanation of this discrepancy is that the image in Fig. 5(c) was recorded using a rather old silver film sample whose surface looked slightly oxidized. The value of the propagation length derived from the image in Fig. 4(b) taken using a freshly prepared silver film equals 30 μm. This number is much closer to the theoretical value.

In some images of surface defects emitting SP beams one can see not only a forward beam but also a weaker beam emitted in the backward direction (Fig. 7). This means that a "plasmon mirror" can be created as another prototype surface optical element. A plasmon beam from one defect can be directed onto another one, as is the case in Fig. 8. One can see a large defect in the top left corner of the image that emits a wide plasmon beam. This beam is scattered by another defect in the middle of the field of view. This experiment shows that one can deal with plasmon "flashlights" in the manner that is very similar to the operation of usual

three-dimensional light sources.

Attenuation of the UV power during the lithography process allows us to create smaller surface defects and study plasmon scattering by these defects. The results of these studies are shown in Figs. 9 and 10. The UV power used to create these smaller defects was approximately $\frac{1}{2}$ of the initial power. We cannot see bright near-field maxima around these defects any more. Instead, we see prominent shadows behind the defects (the direction of plasmon propagation is shown by the arrows). Two characteristic features of these figures emerge. First, the sources of the shadows appear to be larger in the near-field images than in the topographic ones (a comparison of these images with the near-field image in Fig. 4(b) shows that this effect does not stem from the resolution of the near-field images). Second, for different defects the shadows have different, but still large, angular widths. The approximately 90°-angular widths cannot be accounted for by diffraction. The diffraction angle can be easily estimated from the uncertainty principle: $\beta \sim \delta k_{pl}/k_{pl} \sim \lambda_{pl}/(2\pi d)$, where $\lambda_{pl} = 590$ nm is a plasmon wavelength and d is the size of a scatterer. A micrometer size scatterer gives diffraction angle values on the order of 5°. This value is consistent with the rather small visible width of the SP beams from the plasmon "flashlights" in Fig. 4(b). Another interesting feature is an apparent difference in the ability to scatter SP field at hills and dips of similar geometrical size. Looking at Fig. 10 one can notice three defects of about the same lateral size. Two of them are shallow hills. The third is a dip of about the same vertical size. The hills seem not to affect the SP propagation at all. On the other hand, the dip gives a distinct angular shadow. In the next part of the paper we propose an explanation for these phenomena. We have used these phenomena to create another simple two-dimensional optical element which we call a "beam stop."[16] A number of defects were created along a single line on the surface of a silver film (Fig. 4 in Ref. 16). The near-field image shows some increase in the optical field around the defects and a prominent dark shadow behind the line of defects. Thus, an effective optical shield has been created that does not allow plasmons to pass by.

IV. DISCUSSION

The scattering of SP's by surface defects has been considered in numerous theoretical papers. A recent paper by Pincemin et al.[19] contains a good overview of the research in this field. Generally this problem has no analytical solution. Numerically it has been solved for a limited number of experimental geometries. No comparison between such calculations and experimental near-field data has been carried out. Unfortunately, we have not found in the literature any result of numerical calculations that could be directly applied to our observations. Nevertheless we propose two simple models that allow us to understand our results and compare them with theoretical predictions.

The plasmon flashlight phenomenon can be understood directly from the Huygens-Fresnel principle. Let us consider an array of ten secondary sources of SP circular waves (Fig. 11) equally spaced along a 2-μm line. The resulting SP field distribution is given by the expression
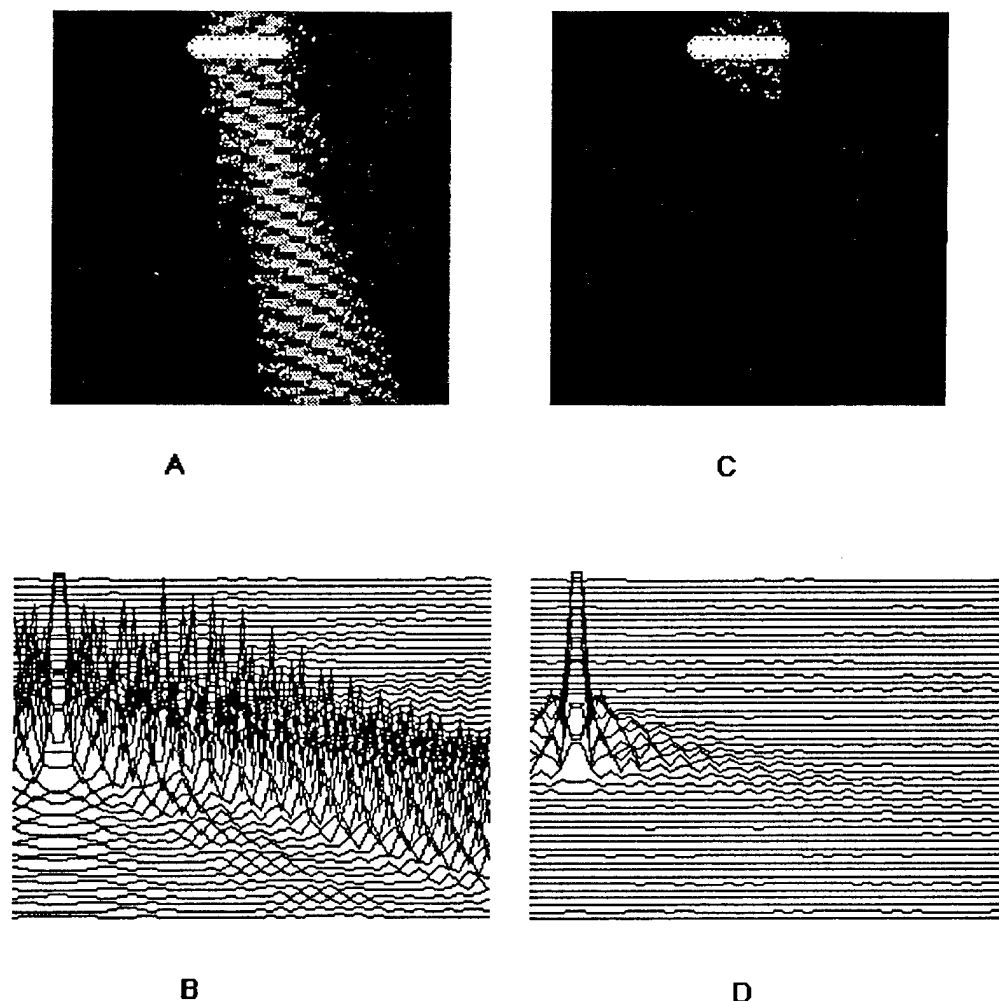
FIG. 11. Field distribution from a 2-μm-long array of point sources in two-dimensional (a), (b) and three-dimensional (c),(d) cases. A pronounced SP beam appears for a two-dimensional field distribution. Horizontal size is 10×10 μm. Halftone views and line scan views are presented.

$$I \sim \left(\sum_n e^{i(kr_n + \phi_n)} / r_n^{1/2} \right)^2, \qquad (1)$$

where r_n is the distance between the point of observation and the nth secondary source. This SP field distribution is shown in Fig. 11(a), 11(b) for the case where the phases of secondary sources change linearly with n. A plasmon beam similar to the one in Fig. 5(b) is clearly visible in the half-tone representation. It appears that the primary reason for the beam existence is a weak $\sim r^{-1/2}$ distance dependence of the fields from individual point sources of circular SP waves. For a comparison, the field distribution from the same source calculated using the bulk r^{-1} distance dependence is shown in Figs. 11(c), 11(d). No prominent beam appears in this case. We believe that the strong maxima of the optical near field observed in Figs. 4(b) and 5(b) can be represented by the arrays of secondary sources of SP circular waves. The phase shift between the secondary waves is due to the angular illumination of the defects by the He-Ne excitation laser. It results in the plasmon beam shining in the direction of the incoming beam of HeNe laser. The enhancement of the near field around the defects should be calculated from the exact theory. The main factors contributing to the enhancement are a "lightning rod effect," which leads to field enhancement

near the prominent hills on the silver film, and larger photon tunneling through the thinner regions of the film.

Figure 12 represents our modeling of data shown in Fig. 4. Two arrays of secondary sources similar to the one discussed in the previous paragraph are positioned at different distances from each other. Figure 12(c) demonstrates a very close resemblance to Fig. 4(b). It is really a surprising result that two plasmon flashlight structures can be positioned within a few micrometers from each other giving rise to distinctly separate plasmon beams. One can envision numerous applications of these structures in sensor arrays. Each plasmon beam could probe the surface chemistry in a very localized region. Based on the success of our plasmon beam modeling we suggest some optical elements that could control SP propagation. One could think of focusing mirrors or lenses consisting of surface defects similar to ones in Fig. 4. Some examples of these optical elements are shown in Fig. 13. A curved defect described (in polar coordinates) by the expression $R(\alpha) = 2F/(1 + \cos\alpha)$ would be a perfect focusing mirror with focal length F: $R(\alpha)$ is a solution of the equation $kR(\alpha) + \phi(\alpha) = \text{const}$ [where $\phi(\alpha) = kR(\alpha)\cos(\alpha)$] for the positions of the point sources that would direct reflected secondary SP waves to be exactly in phase at some particular focal point. A curved defect as shown in Fig. 13(b), which
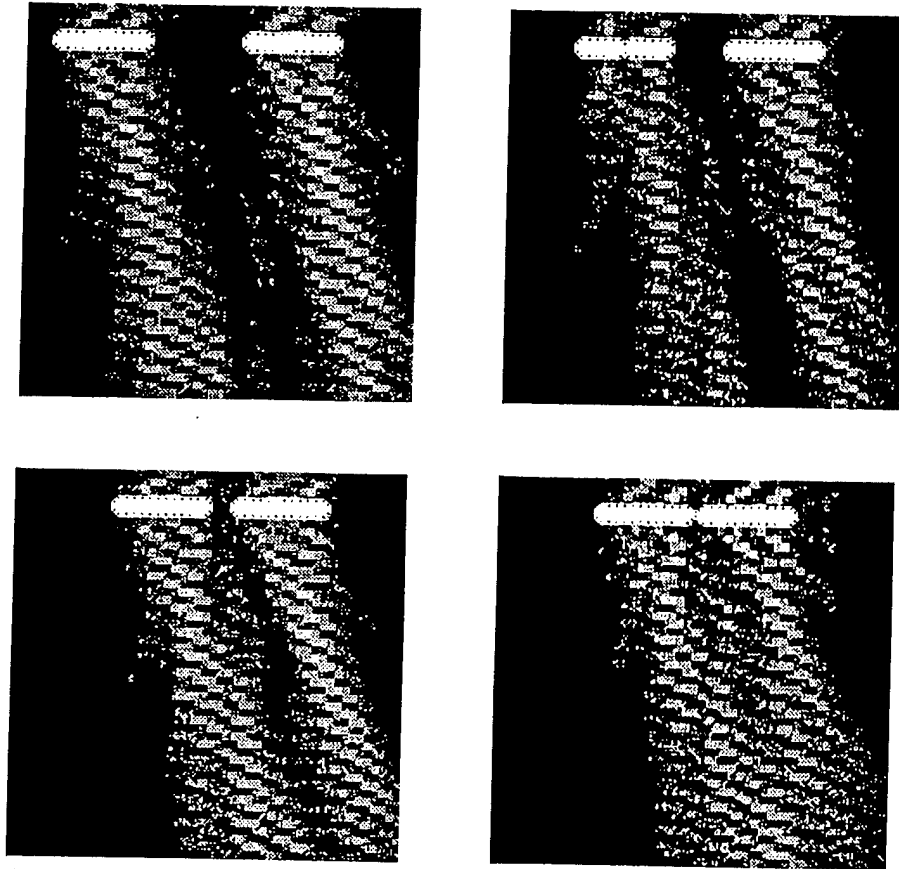
FIG. 12. Numerical modeling of two plasmon flashlights at different distances from each other. Horizontal size is 10×10 μm.

consists of two parts of this focusing mirror positioned next to each other should have two focal points. These calculations are justified by the observation of a "plasmon mirror" in Fig. 7. Another possibility is to create a focusing lens using a zone plate principle. Figure 13(c) represents the field distribution of such an element. The defects are positioned on a circle of radius R in order to compensate for the distance dependence of the field in a circular wave. The angular position of the nth point SP source is given by the expression $kR - kR\cos(\alpha_n) = 2\pi n$. All these optical elements could find numerous applications in integrated optics.

Let us now discuss our data concerning the SP scattering by smaller defects. The simplest explanation of the observed discrepancy between the visible sizes of the shadow sources in the near-field and topographic maps could be that the actual size of the scatterers is not the one that is seen in the surface topographic map. The bulk structure of the silver film can be deformed around the surface defect. Also the chemical composition of the surface oxide layer (and/or absorbed layer) could be changed under UV irradiation on a much larger scale than is apparent in the visible size of the defect. Precise control of these parameters would require experiments under ultrahigh-vacuum conditions. But, there is strong theoretical evidence that the visible size of even a point scatterer in the near-field map may be on the order of some micrometers. Let us imagine a point defect on an otherwise ideally flat metal film surface. This defect is irradiated by a plane surface-plasmon wave. The defect breaks translation symmetry of the film surface. The SP wave can transfer part of its momentum to the defect and decay into a photon.

Consider the cross section of the point defect for such a process. This point defect can be Fourier decomposed into a set of diffraction gratings with periods from zero to infinity (in reality, the upper limit is the inverse atomic size). Since SP scattering is a linear process we can treat the SP interaction with each diffraction grating separately. Each grating can change the momentum of a plasmon by a multiple of its inverse period. Most probably the plasmon momentum will change by only one inverse grating period. If the inverse grating period is smaller than the difference between the momentum of plasmon and the momentum of photon, then plasmon decay will not happen. Hence, only grating with sufficiently large inverse periods will contribute to the cross section of SP decay into photons. In order to find this cross section we should cutoff the Fourier spectrum of the defect at wave vectors less then the difference between the plasmon and photon wave vectors ($k_{pl} - k_{ph}$) and perform an inverse Fourier transformation. Such a procedure gives an effective cross section $s \sim 1/(k_{pl} - k_{ph})$. This cross section is $s \sim 1.6$ μm at HeNe laser wavelengths. This value is consistent with the effective sizes of the shadow sources in Fig. 9(b).

Another effect that might produce a shadowlike phenomenon around a surface defect is attenuated energy transfer from the He-Ne laser excitation beam into the SP's. Resonant excitation of SP's is happening because of the phase matching between the SP and the HeNe beam in the glass prism. The phase-matching length L is determined by the angular width of the SP resonance (see Fig. 1) which is usually on the order of $\delta\alpha \sim 1°$: $\delta k_{pl} L \sim \delta\alpha k_{pl} L \sim 1$. This gives a value of the phase-matching length on the order of $L \sim 5$
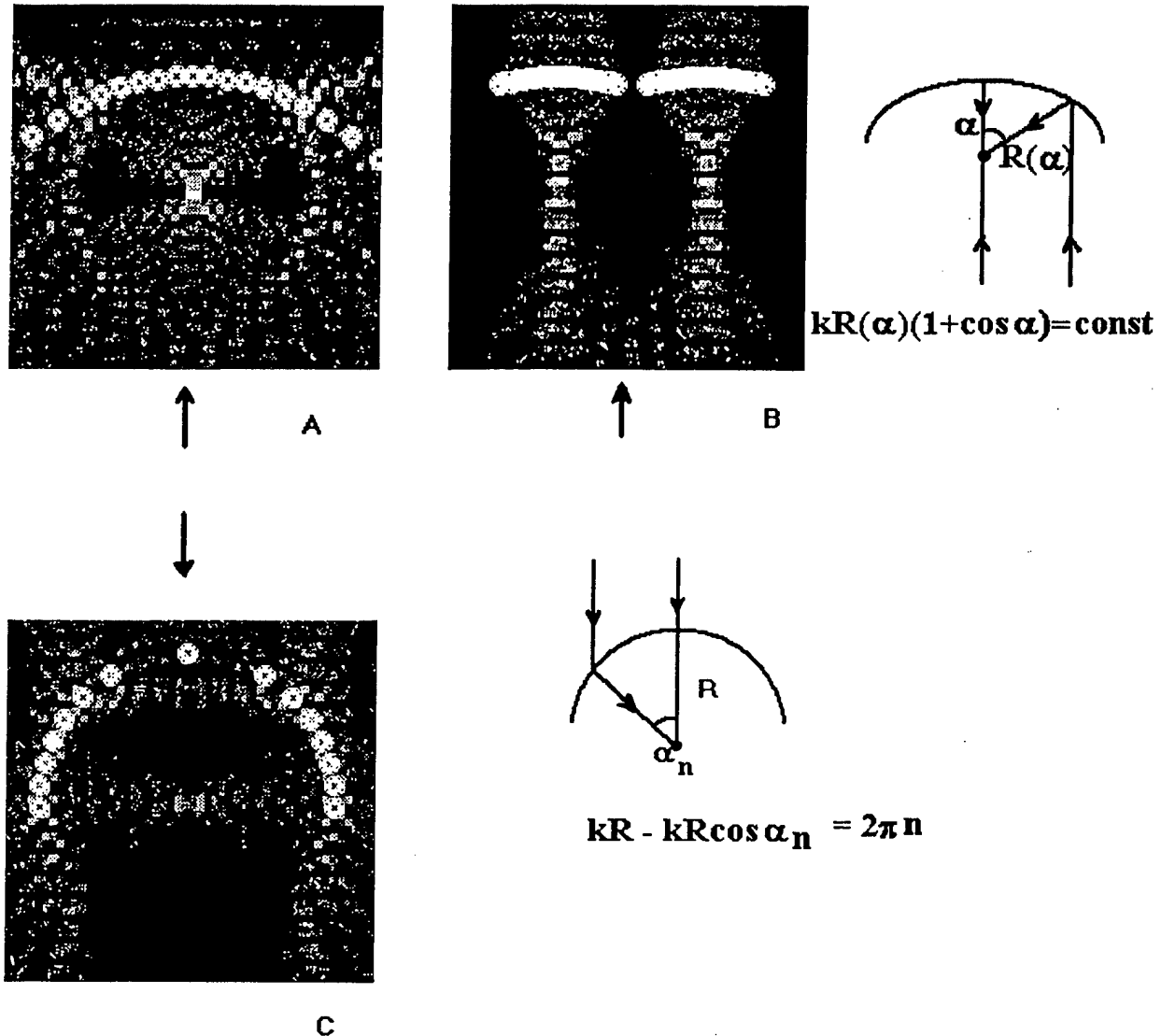
$$kR(\alpha)(1+\cos\alpha)=\text{const}$$

$$kR - kR\cos\alpha_n = 2\pi n$$

FIG. 13. Numerical modeling of plasmon mirrors (a),(b) and a plasmon lens (c). Horizontal size is 10×10 μm.

μm. A surface defect could worsen this phase matching and cause smaller energy transfer in to the SP's. A smaller intensity of the SP field would look like a shadow behind the defect. The two effects discussed above lead to essentially the same effective size of the shadow source. We believe both effects contribute to the observed field distribution. Unfortunately, neither of these effects could be responsible for the angular shape of the shadows and an apparent difference between SP scattering by shallow hills and dips.

The most probable reason for shadows to have an angular shape is refraction. As we have discussed earlier, the SP interaction with a surface defect can be decomposed into interactions with separate gratings that constitute the Fourier spectrum of a defect. Interaction with gratings that have periods much smaller than $2\pi/(k_{pl}-k_{ph})$ leads to SP decay into photons. Interaction with the rest of the gratings can be treated like two-dimensional optics: a plasmon will remain a plasmon after the interaction. Thus, we can talk about SP refraction.

It is relatively easy to introduce an effective refractive index for a shallow dip or hill that scatters a SP wave. The

dispersion relation for the SP in the three-media air-metal-glass system can be written as follows:[20]

$$(\epsilon_1/k_1 + \epsilon_2/k_2)(\epsilon_2/k_2 + \epsilon_3/k_3)$$
$$+ (\epsilon_1/k_1 - \epsilon_2/k_2)(\epsilon_i k_2 - \epsilon_3/k_3)e^{-2k_2d_2} = 0, \tag{2}$$

where $k_n = (k_x^2 - \omega^2\epsilon_n/c^2)^{1/2}$, and $n=1,2,3$ denotes glass, silver film, and air, respectively. After some transformations the dispersion law can be rewritten in the more explicit form:

$$\omega = k_x c[(\epsilon_2 + 1)/\epsilon_2]^{1/2}(1 + Ae^{-2k_2d_2}), \tag{3}$$

where

$$A = 2\epsilon_2 \frac{[(-\epsilon_1\epsilon_2 + \epsilon_2 - \epsilon_1)^{1/2} + i\epsilon_1]}{\{(\epsilon_2^2 - 1)[(-\epsilon_1\epsilon_2 + \epsilon_2 - \epsilon_1)^{1/2} + i\epsilon_1]\}} \sim 0.11 \tag{4}$$
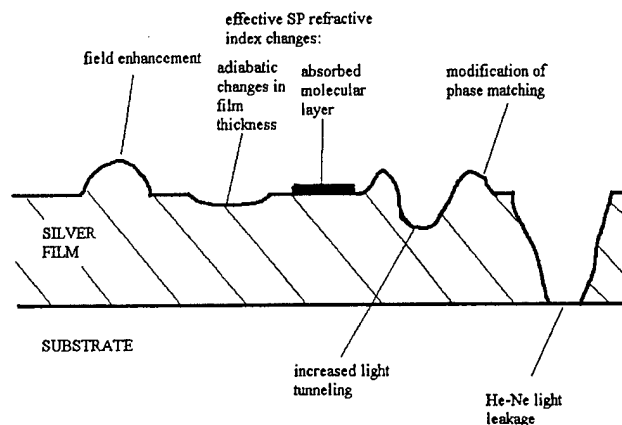
FIG. 14. Summary of different physical mechanisms affecting surface-plasmon field distribution.

(here we assume that the thickness of the silver film is large enough that $e^{-2k_2 d_2} \ll 1$). As we can see, the phase velocity of SP depends on the thickness of the silver film. The SP's are faster in the areas where the thickness of a film is smaller. The effective refractive index of a shallow defect can be written as follows:

$$n = V_0/V = 1 + A(e^{-2k_2 d_0} - e^{-2k_2 d}), \qquad (5)$$

where V is a SP phase velocity at thickness d and V_0 is a SP phase velocity in unmodified areas of a silver film with a thickness d_0. Numerical analysis of this expression shows that in our experiments (with $d_0 = 80$ nm) the effective refractive index n varies within the range 0.89–1.0001. For shallow hills $n > 1$ and the changes in n are negligible, while shallow dips have $n < 1$. This results agrees qualitatively with our observations in Fig. 10. Shallow hills should have much less of an effect on the SP propagation than shallow dips. Evidently, shallow dips act as negative lenses. This results in the angular shape of shadows.

Similar effective refractive indices could be assigned to areas of the silver film where the composition of an absorbed layer is modified. Sometimes the presence of an absorbed layer could lead to appearance of additional SP modes.[21] But in many cases the presence of a few molecular monolayers on the surface of a metal film leads only to a shift in the SP phase velocity.[22] In terms of effective refractive index this shift can be expressed as follows:

$$n = 1 + (\epsilon_a - 1)/[\epsilon_a(-\epsilon_{Ag} - 1)^{1/2}] \times 2\pi d_a/\lambda, \qquad (6)$$

where ϵ_a is a dielectric constant and d_a is the thickness of an absorbed layer (here we assume that $\epsilon_a \ll \epsilon_{Ag}$). According to Ref. 23 four monolayers of cadmium arachidate gives a shift in the SP phase velocity which corresponds to $n = 1.033$. The potential consequence of this result for our experiment is that possible modification of an absorbed layer by an UV light pulse during defect creation could cause refraction of SP's around the defect. On the other hand, this effect can be used to create simple optical elements for SP field redistribution such as lenses or prisms. A triangular region of the silver film covered with a layer of molecules such as cadmium arachidate would act like a prism on a propagating SP beam. One could calculate the dispersion of this prism by taking into account the dispersion of ϵ_{Ag} and ϵ_a. This has the same

order of magnitude as the dispersion of any bulk prism. The dispersion of such optical elements can be used in multichannel chemical sensors and biosensors.

Figure 14 summarizes our discussion of different effects that influence the SP field distribution near surface defects. A change of metal film thickness and the local surface tilt cause the modification of the phase matching between the He-Ne laser light and SP's. Some sharp surface "hills" and holes through the film can cause strong-field enhancement in their vicinity. These effects influence the electromagnetic field distribution in close proximity to these defects. One needs to use an exact theory to describe these "near-field" effects.

The SP "far-field" distribution is much easier to understand using such simple concepts as the Huygens-Fresnel principle and effective SP refractive index. One can replace strong maxima of the near field around the hills and the holes with secondary SP sources. Adiabatic changes in film thickness and local variations in the absorbed molecular layer can be described by an effective refractive indices. Then the nature of SP propagation can be treated as a two-dimensional optics problem.

V. CONCLUSIONS

In summary, we have constructed a combined PSTM/direct-wire lithography setup that has allowed us to study the scattering of surface plasmons by individual defects, while continuously adjusting their shapes and sizes. The use of an uncoated fiber tip as a local probe causes much less perturbation of the SP field as compared to other scanning probe techniques such as STM, AFM, or near-field optical microscopy with metal-coated tips.

Surface defects that emit micrometer wide SP beams (plasmon flashlights) have been observed. This phenomenon has been explained using the Huygens-Fresnel principle. Scattering and refraction of SP field by smaller surface defects has also been studied. The concept of effective refractive index has been introduced for two classes of surface defects: shallow hills or dips, and areas covered with a layer of absorbed molecules. This concept allows us to achieve a qualitative understanding of SP field redistribution by defects, which is otherwise a complicated theoretical problem without an analytical solution.

Some simple optical elements able to govern SP field propagation have been suggested. We believe our technique has the potential to create analogs of any three-dimensional optical devices in two dimensions. Similar techniques can be used not only in the two-dimensional optics of surface plasmons on metal surfaces but also in the optics of any surface waves on semiconductors and dielectrics. Plasmon flashlights in combination with other SP optical elements could have numerous potential applications in multichannel chemical sensing, biosensing, and integrated optics.

[1] *Surface Polaritons*, edited by V. M. Agranovich and D. L. Mills (North-Holland, Amsterdam, 1982).

[2] H. Raether, *Surface Plasmons*, Springer Tracts in Modern Physics Vol. 111 (Springer, Berlin, 1988).

[3] G. N. Zhizhin et al., in *Surface Polaritons* (Ref. 1), p. 122.

[4] B. Liedberg, C. Nylander, and I. Lundstr, Sens. Actuators 4, 299 (1983).

[5] E. Yeatman and E. A. Ash, Electron. Lett. 23, 1091 (1987); B. Rothenhausler and W. Knoll, Nature (London) 332, 615 (1988).

[6] R. Moller et al., J. Vac. Sci. Technol. B 9, 506 (1991); N. Kroo et al., Europhys. Lett. 15, 289 (1991).

[7] M. Specht, J. D. Pedarnig, W. M. Heckl, and T. W. Hansch, Phys. Rev. Lett. 68, 476 (1992).

[8] R. W. Rendell and D. J. Scalapino, Phys. Rev. B 24, 3276 (1981).

[9] R. B. G. De Hollander, N. F. van Hulst, and R. P. H. Kooyman, Ultramicroscopy 57, 263 (1995); Y.-K. Kim, J. B. Ketterson, and D. J. Morgan, Opt. Lett. 21, 165 (1996).

[10] *Near Field Optics*, edited by D. W. Pohl and D. Courjon (Kluwer, The Netherlands, 1993).

[11] B. Hecht et al., in *Photons and Local Probes*, edited by O. Marti and R. Moller (Kluwer, The Netherlands, 1995), p. 93; Phys. Rev. Lett. 77, 1889 (1996).

[12] R. C. Reddick, R. J. Warmack, and T. L. Ferrel, Phys. Rev. B 39, 767 (1989); D. Courjon, K. Sarayeddine, and M. Spajer, Opt.

Commun. 71, 23 (1989); F. de Fornel et al., Proc. SPIE 77, 1139 (1989).

[13] O. Marti et al., Opt. Commun. 96, 225 (1993); P. M. Adam et al., Phys. Rev. B 48, 2680 (1993).

[14] P. Dawson, F. de Fornel, and J.-P. Goudonnet, Phys. Rev. Lett. 72, 2927 (1994).

[15] S. I. Bozhevolnyi, I. I. Smolyaninov, and A. V. Zayats, Phys. Rev. B 51, 17 916 (1995).

[16] I. I. Smolyaninov, D. L. Mazzoni, and C. C. Davis, Phys. Rev. Lett. 77, 3877 (1996).

[17] I. I. Smolyaninov, D. L. Mazzoni, and C. C. Davis, Appl. Phys. Lett. 67, 3859 (1995); I. I. Smolyaninov et al., in *Conference on Lasers and Electro-Optics*, OSA Technical Digest Series (OSA, Washington, D.C., 1996), Vol. 9, p. 253.

[18] E. Kretschmann and H. Raether, Z. Naturforsch. A 23, 2135 (1968).

[19] F. Pincemin, A. A. Maradudin, A. D. Boardman, and J.-J. Greffet, Phys. Rev. B 50, 15 261 (1994).

[20] C. A. Ward et al., J. Chem. Phys. 62, 1674 (1975).

[21] V. M. Agranovich, Zh. Éksp. Teor. Fiz. 77, 1124 (1979) [Sov. Phys. JETP 50, 567 (1979)].

[22] F. Abeles and T. Lopez-Rios, in *Surface Polaritons* (Ref. 1), p. 252.

[23] J. G. Gordon and J. D. Swalen, Opt. Commun. 22, 374 (1977).

Near-field second harmonic generation from a rough metal surface

Igor I. Smolyaninov, Anatoly V. Zayats, and Christopher C. Davis
Electrical Engineering Department, University of Maryland, College Park, Maryland 20740
(Received 5 June 1997)

Local second-harmonic generation (SHG) from a rough metal surface has been measured using a near-field optical microscope. The dependence of the SH signal on the tip-surface distance for excitation with S- and P-polarized light shows the presence of evanescent SH field components. With excitation by S-polarized light the SHG over the rough surface is found to be strongly related to surface topography. For P-polarized light excitation, local enhancement of SH emission have been observed that may be attributed to SH field localization. [S0163-1829(97)07040-9]

I. INTRODUCTION

In recent years there has been increasing interest in linear and nonlinear optics of disordered media, particularly rough surfaces.[1] Because second-harmonic generation (SHG) is known to be surface sensitive on an atomic scale[2] (especially when the nonlinearity itself is due to the presence of the surface, as is the case for isotropic materials[3]), studies of the nonlinear optical response are particularly suitable for improving our knowledge of the relationship between optical properties and morphology (roughness, defects, impurities, adsorbates) of metallic and semiconductor surfaces.[4,5]

Second-harmonic generation from very flat surfaces has been extensively studied.[2,6] However, real surfaces always have different degrees of roughness. The inclusion of roughness leads to several phenomena affecting SHG (such as relaxation of polarization selection rules and an enhancement of the electromagnetic field by the roughness). Less obvious is the strong influence of weak-localization effects on the SHG from rough surfaces[7] that result in significant changes of the angular spectrum of SHG observed in the far-field region.[8] Even more pronounced changes should be expected in the near-field region close to the surface.

Until now, SHG from rough surfaces has been studied only in the far-field region without exact knowledge of the surface topography. Information provided by the usual (far-field) optical studies of surfaces is derived from data averaged over a surface region limited, in the best case, by diffraction of the probe light. However, the usual sizes of these regions is much larger: from several square micrometers to several square millimeters. Thus, optical data obtained from linear and nonlinear spectroscopy are valid for very large defect ensembles. At the same time, the lateral distribution of the electromagnetic field over a surface is not uniform and depends itself on the surface defect structure. The local-field intensity can vary by several orders of magnitude on a scale less than half a wavelength along the surface.[9,10] Therefore, investigation of the averaged optical response in many cases does not result in an understanding of the underlying physics (especially in nonlinear spectroscopy where optical response depends on the driving field in a nonlinear manner).

The recent development of near-field optical microscopy (NFOM) has opened the possibility for study of numerous optical phenomena with a resolution well below the diffraction limit.[11] Most near-field optical studies have concentrated on the investigation of the linear optical response of materials. The possibility of studying nonlinear optical processes (especially, wave mixing) with near-field optical characterization methods has been discussed recently,[12,13] but only phase-conjugation experiments were experimentally realized in the near-field region.[14] This slow progress in nonlinear near-field optics stems from numerous experimental difficulties caused by the small optical throughput of conventional metal-coated near-field apertures. This small throughput enters quadratically into the measured SH optical signal. Another disadvantage of metal-coated fiber tips in nonlinear optical measurements is a strong perturbation introduced by a tip into the local surface field distribution. For example, in SHG experiments SH light intensity is proportional to the fourth power of the local field. Hence, by using a metal-coated fiber tip one can study only the properties of a microresonator formed between the tip and the sample, but not the true local SH field distribution. Uncoated fiber tips (used in Ref. 14) introduce much smaller perturbation into the local field near the sample, since the dielectric constant ϵ of a fiber is much less than ϵ of a metal. However, the decrease in optical confinement does lead to somewhat lower resolution.

The combination of second-harmonic generation techniques with near-field optical microscopy has significant potential for probing the nonlinear optical response of a surface locally with subwavelength lateral resolution while simultaneously measuring surface topography using shear-force feedback. The data obtained in such a way may allow comparison of experiment and theory in sufficient detail to understand the essential features of SHG at rough surfaces and provide better understanding of the underlying microscopic electrodynamics. Since SHG is sensitive to any asymmetry of the sample, it is sensitive to surface magnetic or electric dipole moments. Near-field SHG microscopy can be used to image magnetic or electric domains and is an alternative to magnetic and electric force microscopies in this regard. Near-field SHG microscopy of a rough metal surface is an important first step in this direction.

In this paper we report the observation of second-harmonic light generated at a rough silver surface using a near-field optical microscope. The SH signal dependence on the tip-surface distance has been measured for S and P polarization of the excitation light. The spatial distribution of
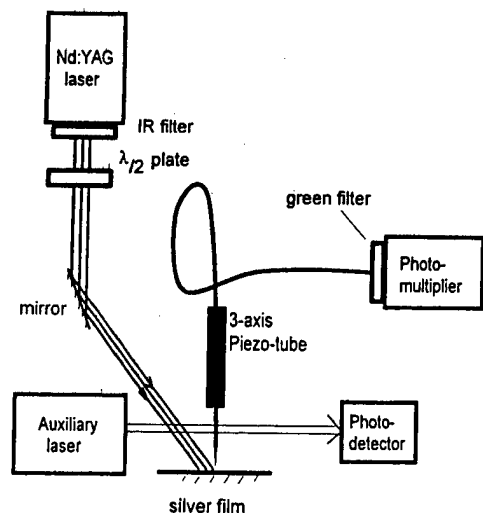
FIG. 1. Schematic view of the near-field optical microscope for second-harmonic light studies.

SHG over the surface has been imaged. Such images demonstrate that different mechanisms affect surface SHG at rough metal surfaces for S- and P-polarized excitation light. Our data clearly show near-field features inaccessible in the usual far-field measurements.

II. EXPERIMENTAL SETUP

Our experimental setup for near-field microscopy of second-harmonic generation is shown in Fig. 1. A 400-nm-thick silver film was prepared by thermal evaporation on a glass substrate and was used as the sample in our near-field optical microscope. The local SH field distribution has been probed with an uncoated adiabatically tapered fiber tip, which is drawn at the end of a single mode fiber by heating it with a CO_2 laser in a micropipette puller. The fiber tip can be scanned over the sample surface with a constant tip-surface distance of a few nanometers using shear force feedback control. Therefore, surface topography can be imaged with a resolution on a nanometer scale, while simultaneously recording the SH near-field image. The SHG has been excited at an angle of incidence of 60° with a Nd:YAG (yttrium aluminum garnet) laser operating at 1064 nm (repetition rate 10 Hz, pulse duration 20 ns, pulse energy 10–15 mJ). The excitation power at the sample surface is estimated to be about 1 MW/cm^2. The SH signal has been measured with a photomultiplier and gated electronics. The SH signal at every point of the image has been averaged over 70 or 100 laser pulses for P-polarized and S-polarized light excitation, respectively. The characteristic SH photon counting rate was on the order of one photon count per 3–5 laser pulses. The main source of noise in our data is statistical fluctuation ($N^{1/2}$) of the number of photon counts detected. The measured SH intensity depends quadratically on the fundamental light power. The spatial resolution of the microscope in the SH light collection mode has been determined to be better than 150 nm (this is the size of the smallest features visible in the SH images of piezoelectric ceramics and the sharpness of magnetic domain walls observed in SH images of a Ni surface[16]). The fiber tip itself did not contribute to the SH
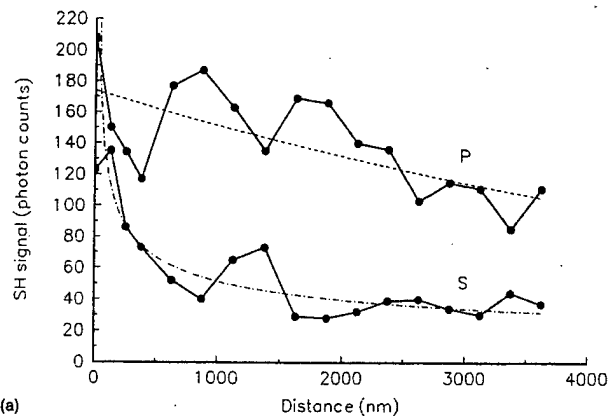
(a)
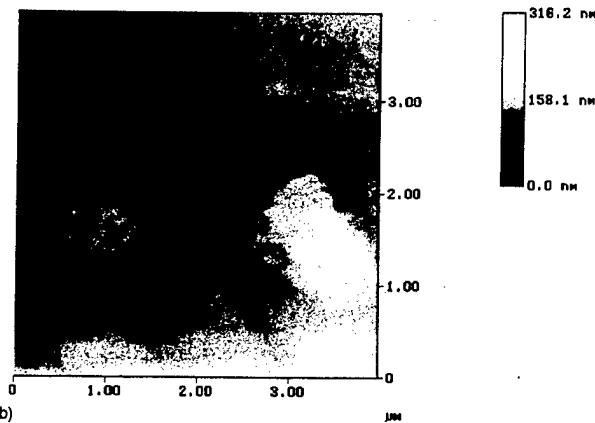
(b)

FIG. 2. (a) Variation of SH signal on the tip-sample distance for S- and P-polarized excitation. These variations have been measured in the center of the silver film region imaged in (b). The noise level in these data is determined by the statistic fluctuations ($N^{1/2}$). Dashed lines are simple power-law curves drawn as a guide to the eye.

signal: we measured zero SH signal when the sample was far from the tip.

III. RESULTS AND DISCUSSION

To determine the contribution of near-field processes to the SH generation, we have studied the dependence of the second-harmonic signal on the tip-sample distance for S- and P-polarized excitation light [Fig. 2(a)]. These measurements were made near the center of the silver film surface shown in Fig. 2(b). A rather strong decrease in the signal occurs about 500 nm from the surface. This behavior is especially pronounced for S-polarized excitation. This initial drop in the signal is followed by a number of oscillations for both polarizations. Note that each maximum for P-polarized excitation corresponds to a minimum for S-polarized excitation and vice versa. Similar oscillations have been observed at every point on the sample surface. We believe that this behavior results from the standing waves of the 1064 nm fundamental light formed between the glass tip and silver film surface. The phase shift of π between the distance dependencies can be explained by the phase shift of π between P- and S-polarized fundamental waves reflected between tip and metal at angles larger than the Brewster angle.

The ratio of the SH signals induced by P- and S-polarized

light changes substantially in the near-field region. This ratio falls from 3.1 at a distance of 3600 nm from the surface to 1.5 near the surface. This is a nontrivial near-field phenomenon. In the dipole approximation the nonlinear polarization $P(2\omega)$ induced by incident laser light $E(\omega)$ is equal to

$$P_i(2\omega) = \chi_{ijk}^d E_j(\omega) E_k(\omega) + \cdots . \tag{1}$$

Here χ_{ijk}^d is an electric dipole related source of the nonlinear susceptibility. Symmetry considerations show that this contribution is absent in centrosymmetric media and in this case the only remaining source of nonlinearity is a surface interface where inversion symmetry is broken. SHG from a perfectly flat metal surface can be excited mainly with P-polarized light while the much smaller S-polarized-light-induced SHG is a measure of the roughness of the surface.[17] In the near-field region there is a substantial contribution from evanescent fundamental and second-harmonic fields. Phase-matching condition and polarization selection rules are meaningless in the near-field region of a rough surface. Both are defined with respect to the plane of incidence by the direction of propagation and the normal to the surface. There is no direction of propagation for an evanescent wave. The normal direction depends on the scale of observation and does not coincide with the average normal to the sample surface. As a consequence there is a substantial increase in S-polarized-light-induced evanescent SH field in the vicinity of a rough surface.

Simultaneously measured topographical and near-field second-harmonic images of the silver film are shown in Figs. 3 and 4. For these figures characteristic data acquisition time was 4–6 h. The power of the 1064 nm light has been selected in a trade off between signal magnification and the rate of thermal drift of the image. The noise in the topographical image is due to the laser pulses striking the sample surface. The noise in the SH image results from statistical variations in the number of photons counted in individual pixels.

Near-field images in Figs. 3(b) and 3(d) have been measured using S-polarized excitation light. It appears that the main contrast mechanism for the S-polarized-light-induced near-field SH image is topography variation. The surface topography in Fig. 3(a) can be described as essentially flat regions at the top and at the bottom of the image separated by a narrow groove. The SH image [Fig. 3(b)] looks almost like a "negative" of the topographical image. The SH signal measured in the flat regions is much smaller than the signal measured near the groove. In Fig. 3(c) one can see generally flat regions at the left and at the right sides of the image divided by a step. Again, the SH signal measured near the step is much larger than the signal measured in the flat regions [Fig. 3(d)]. In both cases the enhancement of SH generation induced by S-polarized excitation occurs near the places on the surface where inhomogeneities are present. This effect has the same origin as the growth of the ratio of S-polarized- to P-polarized-light-induced SH signals near the rough surface discussed above.

Generally, P-polarized-light-induced SH images are much more complicated. The topographical image in Fig. 4(a) shows a rather usual picture of different crystalline grains randomly distributed over the silver film surface. In the SH image these grains have different brightness: the
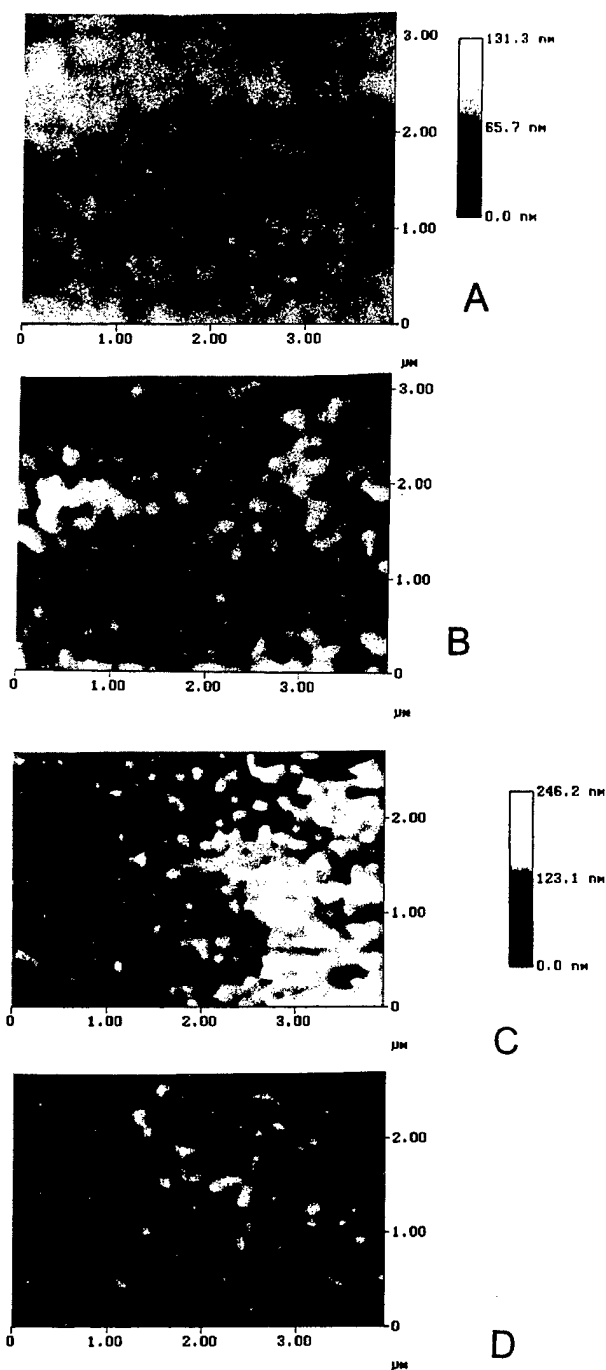

FIG. 3. Topography (a),(c) and SH light distribution (b),(d) measured for S-polarized excitation light.

grain in the bottom right corner looks much darker than the grain in the top right corner. This contrast may be due to the different crystalline orientation of different grains. SH generation is known to be sensitive to the atomic structure of the surface,[2] since in an isotropic metal such as silver the SH light is generated within the top few atomic surface layers. In addition, our experiments have been conducted under ambient conditions. Although we have used freshly prepared silver films, surface oxidization could have affected our results. The rate of surface oxidization depends on crystalline orientation. Thus, we may see a contrast that is related to surface chemistry of the silver film. It will be necessary to conduct further experiments in ultrahigh vacuum to clarify this issue.
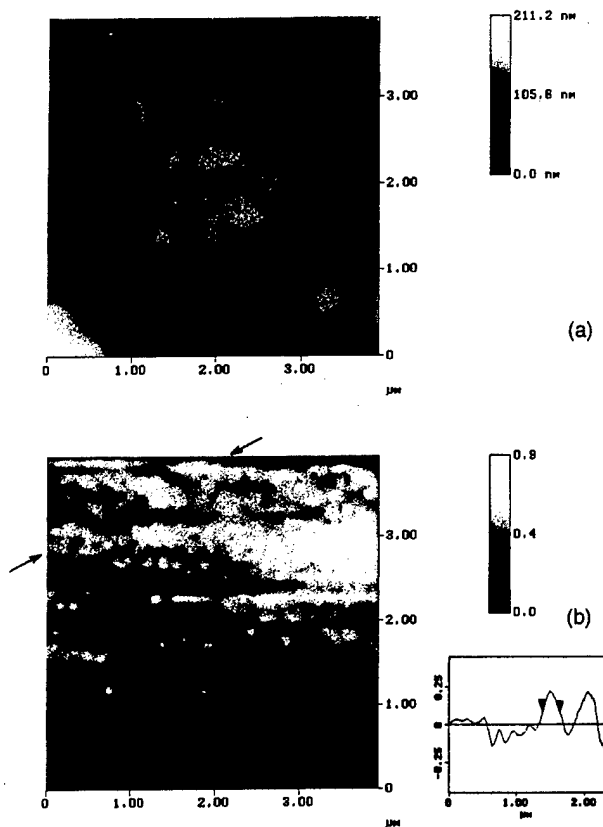
FIG. 4. Topography (a) and SH light distribution (b) measured for P-polarized excitation light. The cross section of the SH image along the line determined by the arrows is shown in the inset.

An interesting feature of Fig. 4(b) is the presence of small bright spots in the top part of the image. The cross section through two of these spots is shown in the inset. The width of the spot shown by the markers is equal to 240 nm, or about half of the wavelength of the SH light. Bright spots with similar sizes have been detected in the surface near-field distribution with surface plasmon-polariton (SPP) excitation.[10] These spots have been identified as the result of optical field localization.

In fact, SH generation at a rough surface and SPP excitation are closely related phenomena since any surface defect is a source of a surface wave.[15] Localization effects in the SH generation from rough metal surfaces have been predicted by McGurn, Leskova, and Agranovich.[7] It has been shown that multiple scattering leading to light localization gives a contribution to the SH generation. Both fundamental and second-harmonic wave localization contributes to the effect giving rise to components of SH light propagating perpendicularly to the average sample surface and in the reverse direction to the fundamental wave propagation, respectively. The latter process results in a local surface enhancement of the SH field. The spots observed in Fig. 4(b) may correspond to this localization. Previously, the SH field localization has been observed indirectly by measuring weak changes in the far-field angular distribution of the SH lights.[8]

IV. CONCLUSION

In summary, we have presented images of SH light emission taken in near-field proximity to a metal surface together with corresponding images of surface topography. Differences in the mechanisms of SH generation for different polarizations of the excitation light have been demonstrated. For S-polarized excitation the observed local SH generation is related mainly to the topology of the surface. For P-polarized light excitation, local enhancement of SH emission have been observed that may be attributed to SH field localization. We believe that these results are important for further development of SH near-field microscopy, which may become a useful tool in magnetic and electric domain imaging and has the potential for accessing the microscopic electrodynamics of rough surfaces.

[1] K. A. O'Donnel, in Current Trends in Optics, edited by A. Consortini, ICO Series (Academic Press, London, 1995).

[2] J. F. McGilp, Prog. Surf. Sci. 49, 1 (1995).

[3] N. Blombergen, R. K. Chang, S. S. Jha, and C. H. Lee, Phys. Rev. 174, 813 (1968).

[4] Y. R. Shen, J. Vac. Sci. Technol. B 3, 1464 (1985).

[5] T. F. Heinz, M. M. T. Loy, and W. A. Thompson, Phys. Rev. Lett. 54, 63 (1985).

[6] Nonlinear Surface Electromagnetic Phenomena, edited by H.-E. Ponath and G. I. Stegeman (North-Holland, Amsterdam, 1991).

[7] A. R. McGurn, T. A. Leskova, and V. M. Agranovich, Phys. Rev. B 44, 11 441 (1991).

[8] Y. Wang and H. J. Simon, Phys. Rev. B 47, 13 695 (1993).

[9] D. P. Tsai et al., Phys. Rev. Lett. 72, 414 (1994).

[10] S. I. Bozhevolnyi, I. Smolyaninov, and A. Zayats, Phys. Rev. B 51, 17 916 (1995); S. I. Bozhevolnyi, B. Vohnsen, I. I. Smolyaninov, and A. V. Zayats, Opt. Commun. 117, 417 (1995).

[11] Near Field Optics, edited by D. W. Pohl and D. Courjon (Kluwer, Dordrecht, 1993).

[12] X. Zhao and R. Kopelman, Ultramicroscopy 61, 69 (1995).

[13] J. M. Vigoureux, C. Girard, and F. Depasse, J. Mod. Opt. 41, 49 (1994).

[14] S. I. Bozhevolnyi, O. Keller, and I. Smolyaninov, Opt. Lett. 19, 1603 (1994).

[15] I. I. Smolyaninov, D. L. Mazzoni, and C. C. Davis, Phys. Rev. Lett. 77, 3877 (1996).

[16] I. I. Smolyaninov, A. V. Zayats, and C. C. Davis, Opt. Lett. (to be published).

[17] K. J. Song, D. Heskett, H. L. Dai, A. Liebsch, and E. W. Plummer, Phys. Rev. Lett. 61, 1380 (1988).

Near-field second-harmonic imaging of ferromagnetic and ferroelectric materials

Igor I. Smolyaninov, Anatoly V. Zayats, and Christopher C. Davis

Department of Electrical Engineering, University of Maryland, College Park, Maryland 20740

A novel scanning probe technique that is able to image surface magnetic and electric properties has been developed. It is based on the near-field microscopy of surface second-harmonic generation. We have demonstrated the capability of the technique by imaging the domain structure of a Ni single crystal and a piezoelectric ceramic.   © 1997 Optical Society of America

Ferromagnetic and ferroelectric materials have numerous applications in modern technology. The performance of these materials is determined by their properties at the microscopic level, particularly by the sizes of magnetic (or electric) domains and domain boundaries. For example, one bit of information in a modern magnetic disk is recorded in a 1-μm size domain. Ferroelectric materials are widely used in computer DRAM chips. Since there is a need to increase data density in magnetic and electric storage devices, it is important to develop high-resolution tools to characterize their structure.

There are three major techniques for magnetic structure observations; they rely on the use of polarized electrons, the magneto-optical Kerr effect, and magnetic force microscopy.[1-3] The recent development of near-field microscopy allows the diffraction-limited resolution of conventional microscopy to be overcome.[4] This achievement allows one to use many potential advantages of optical methods in high-resolution magnetic material imaging, such as time resolution, spectral sensitivity, and noninvasiveness with respect to magnetic structure. Measurements in high magnetic fields can be performed since the probe used is nonmagnetic.

Recently, magneto-optical Kerr near-field transmission microscopy has been developed for transparent samples.[5] Implementation of a similar technique in reflection (to study opaque samples) is rather difficult because reflected light often becomes depolarized when the near-field microscopy tip is in close proximity to a conducting surface.[6] Very recently such measurements have been conducted,[7] although the achieved signal-to-noise ratio was 1:1.

Magnetization-induced second-harmonic generation (SHG) is a nonlinear version of the magneto-optical Kerr technique[8,9] that has been shown to have a very large magneto-optical response.[10] SHG has been used successfully in far-field imaging of magnetic-domain structures.[11] We report implementation of this technique in near-field optical imaging of magnetic materials with spatial resolution of better than 150 nm. This implementation is based on recently developed near-field SHG microscopy.[12]

Our experimental setup for near-field microscopy of SHG shown in Fig. 1. The local second-harmonic

(SH) field distribution was probed with an uncoated adiabatically tapered fiber tip, which was drawn at the end of a single-mode fiber by heating with a CO_2 laser in a micropipette puller. The fiber tip can be scanned over the sample surface with a constant tip–surface distance of a few nanometers by shear-force feedback control. Therefore, surface topography can be imaged with resolution on a nanometer scale, while the SH near-field image is simultaneously recorded. SHG was excited at an angle of incidence of 60° with a Nd:YAG laser operating at 1064 nm (repetition rate, 10 Hz; pulse duration, 20 ns; pulse energy, 10–15 mJ). The SH signal was measured with a photomultiplier and gated electronics. The signal depends quadratically on the fundamental light power. The SH signal at every point of the image was averaged over a few tens of laser pulses, so image-acquisition time was several hours. This drawback can be overcome by use of a Ti:sapphire laser with a high repetition rate.

In the dipole approximation the nonlinear polarization $\mathbf{P}(2\omega)$ of a magnetic medium induced by incident
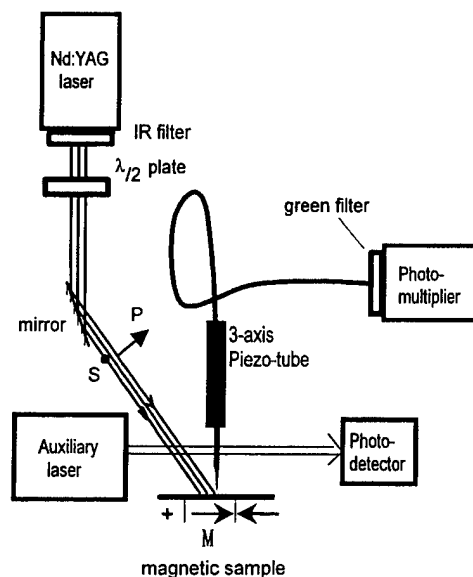

Fig. 1.   Experimental setup for near-field SH microscopy. An auxiliary laser is used for shear-force feedback control.

laser light $\mathbf{E}(\omega)$ is equal to

$$P_i(2\omega) = \chi_{ijk}^d E_j(\omega) + \chi_{ijkl}^m E_j(\omega)E_k(\omega)M_l + \ldots . \quad (1)$$

Here χ_{ijk}^d is an electric dipole contribution to the nonlinear susceptibility, χ_{ijkl}^m is magnetization-induced term, and $\mathbf{M}$ is the magnetization of the medium (the second term describes direct magnetization-induced SH polarization and the influence of the magnetization on the symmetry of the electric dipole contribution). Symmetry considerations show that both terms are absent in centrosymmetric media, and the only remaining source of nonlinearity is a surface interface where inversion symmetry is broken. SHG arises from the top few atomic surface layers. Magnetization-induced contrast depends on the polarization state of the excitation light and the orientation of the magnetization vector in the sample. At zero magnetization, SHG from a perfectly flat metal surface can be excited mainly with p-polarized light, while the much smaller s-polarized-light-induced SHG is generally a measure of the roughness of the surface[13] (since metals are not exactly described by a jellium model there is also some contribution that is due to the crystal structure of metals). Under p-polarized excitation, the motion of electrons has a component perpendicular to the surface. This perpendicular motion of electrons in the top atomic layers is strongly affected by the presence of the surface. The consequent asymmetric motion gives rise to SH generation. Under s-polarized excitation, the driving field is parallel to the surface, and SHG is much weaker in this case.

If the magnetization is nonzero and has a component parallel to the surface and perpendicular to the electric field of the s-polarized excitation light (Fig. 1), the motion of electrons near the surface becomes asymmetric because of the Lorentz force acting perpendicular to the surface. This gives rise to SH generation. This SHG is insensitive to the sign of magnetization. The component of the electric field of the p-polarized excitation light parallel to the surface gives similar SHG. In this case magnetization-induced SHG adds to the nonmagnetic contribution from the component of the electric field perpendicular to the surface. Equation (1) shows that p-polarized-light-induced SHG is sensitive to the sign of magnetization, since nonlinear polarization is linear in the magnetization vector.

In a jellium model, magnetization perpendicular to an ideally flat surface does not contribute to the SHG for both polarizations of the excitation light. However, this magnetization can be allowed by the symmetry of the surface electronic band structure and has been observed recently.[14] It can also be observed from a rough surface since the normal direction to the surface is not well defined.[12] We observed this behavior in our experiment with a strong permanent SmCo magnet. The SH intensity observed from the side surface of the magnet was almost an order of magnitude stronger than from the pole surface.

Taking into account the considerations above, we chose to use s-polarized excitation light in magnetic-domain imaging. We studied magnetic domains at the [100] surface of a Ni single crystal. Before the experiment the sample had not been specially magne-

tized. Images of surface topography and spatial distribution of SHG are shown in Figs. 2(a) and 2(b). Bright and dark regions with characteristic rectangular shapes are seen in the SH image. These features do not correlate with surface topography, which is rather flat. The rectangular features resemble the characteristic shapes of the domains of closure in ferromagnetics.[15] We conclude that the regions with uniform brightness are magnetic domains with different orientations of magnetization. The sizes of the domains observed are of the order of a few micrometers, which is the usual size of magnetic domains in Ni. After the sample is exposed to a strong magnetic field perpendicular to its surface, the domain structure is changed, as can be seen in the SH image in Fig. 2(c). SH light intensity decreased since the induced magnetization was perpendicular to the surface.

The cross section of the SH image in Fig. 2(b) perpendicular to a domain wall is shown in the inset of Fig. 2. The width of a transition region between a pair of domains is equal to 150 nm. This number is close to the known thickness of a Bloch wall (magnetic-domain boundary),[15] that is, ~100 nm, and gives us an estimate of the resolution of our near-field SH microscope.

A ferroelectric material that we studied is poled lead zirconate titanate piezoceramic. Crucial parameters of piezoceramic performance are hysteresis, linearity, and creep, which depend on the quality of poling. A typical image of the SH intensity distribution is shown in Fig. 3. It was recorded with p-polarized
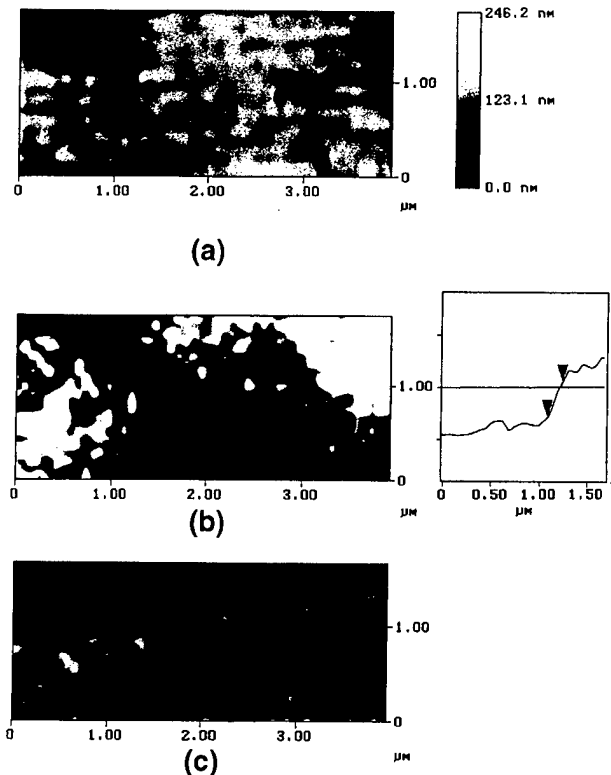

(a)

(b)

(c)

Fig. 2. (a) Topography and (b), (c) SH light distribution measured for the Ni single crystal (b) before and (c) after exposure to a strong magnetic field. The inset shows the cross section of the SH image in (b) perpendicular to a domain wall.
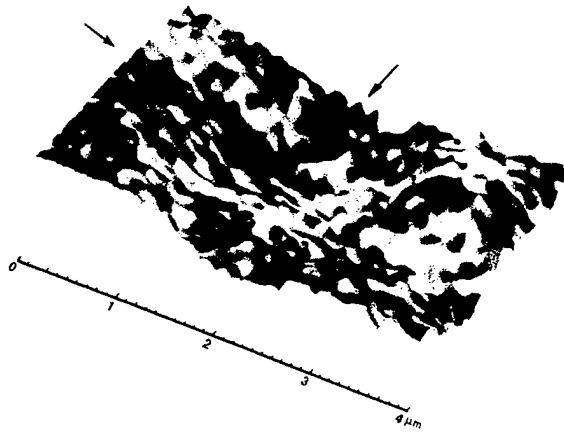
Fig. 3. SH intensity distribution over the piezoceramic surface. This image is a superposition of the surface topography shown as a quasi-three-dimensional view and the half-tone SH image.

fundamental light. The poling vector was parallel to the sample surface. The polycrystalline structure of the ceramic is clearly seen in the topography. Different crystallites show different brightness of SH emission that may correspond to variations in poling. One of the crystallite boundaries (shown by the arrows) also shows a difference in SH brightness from the rest of the material. We believe that such defects contribute to the effects of hysteresis and creep of piezoceramics.

In summary, we have developed a novel scanning probe technique that is able to image surface magnetic and electric properties. It is based on near-field optical imaging of the surface. We have demonstrated resolution of better than 150 nm by using uncoated tapered fiber tips.

References

1. R. Feder, ed. *Polarized Electrons in Surface Physics* (World Scientific, Singapore, 1985).
2. M. Born and E. Wolfe, *Principles of Optics* (Pergamon, London, 1959).
3. R. D. Gomez, E. R. Burke, and I. D. Mayergoyz, J. Appl. Phys. **79,** 6441 (1996).
4. D. W. Pohl and D. Courjon, eds., *Near Field Optics* (Kluwer, Dordrecht, The Netherlands, 1993).
5. E. Betzig, J. K. Trautman, R. Wolfe, E. M. Gyorgy, P. L. Finn, M. H. Kryder, and C. H. Chang, Appl. Phys. Lett. **61,** 142 (1992).
6. J. K. Trautman, E. Betzig, J. S. Weiner, D. J. DiGiovanni, T. D. Harris, F. Hellman, and E. M. Gyorgy, J. Appl. Phys. **71,** 4659 (1992).
7. C. Durkan, I. V. Shvets, and J. C. Lodder, Appl. Phys. Lett. **70,** 1323 (1997).
8. J. Reif, C. Rau, and E. Matthias, Phys. Rev. Lett. **71,** 1931 (1993).
9. R.-P. Pan, H. D. Wei, and Y. R. Shen, Phys. Rev. B **39,** 1229 (1989).
10. B. Koopmans, M. G. Koerkamp, Th. Rasing, and H. van den Berg, Phys. Rev. Lett. **74,** 3692 (1995).
11. V. Kirilyuk, A. Kirilyuk, and Th. Rasing, Appl. Phys. Lett. **70,** 2306 (1997).
12. I. I. Smolyaninov, A. V. Zayats, and C. C. Davis, Phys. Rev. B **56,** N16 (1997).
13. K. J. Song, D. Heskett, H. L. Dai, A. Liebsch, and E. W. Plummer, Phys. Rev. Lett. **61,** 1380 (1988).
14. M. Straub, R. Vollmer, and J. Kirschner, Phys. Rev. Lett. **77,** 743 (1996).
15. C. Kittel, *Introduction to Solid State Physics* (Wiley, New York, 1996).

Focused ion-beam fabrication of fiber probes with well-defined apertures for use in near-field scanning optical microscopy

Saeed Pilevar,[a] Klaus Edinger,[b] Walid Atia, Igor Smolyaninov, and Christopher Davis[c]
Electrical Engineering Department, University of Maryland, College Park, Maryland 20742

We present a focused ion-beam (FIB) fabrication method for very clean and well-defined subwavelength fiber probes with metallic apertures of a desired diameter for use in near-field scanning optical microscopy. Such probes exhibit improved features compared to probes coated with metal by the conventional angled evaporation technique. Examples of FIB fabricated fiber probes are shown and images of a test sample are presented using one of the probes in a near-field microscope. © *1998 American Institute of Physics.* [S0003-6951(98)04524-0]

In the past decade, near-field scanning optical microscopy (NSOM) has successfully demonstrated its capability of subwavelength optical resolution by breaking the diffraction limit of conventional optical microscopy.[1,2] The optical near field of a source exists within a distance of less than one optical wavelength from it. By following Synge's[3] original suggestion, involving the use of a tiny aperture (diameter ≪λ) in a metal screen that is placed in near-field proximity to a sample, optical microscopy can achieve a resolving power below the classical Abbé limit. Practical implementation of a tiny aperture in a conductive screen is accomplished by tapering down an optical fiber to subwavelength diameter using the heating–pulling technique[4] followed by metallic overcoating of the sides of the fiber to define an aperture.

The major drawback of pulled near-field tips is their low optical throughput, which is a key parameter influencing their better utilization in applications such as optical spectroscopy,[5] nanofabrication,[6] and high-density data storage.[7] To overcome this problem many researchers[8-11] have attempted to fabricate NSOM probes of a desired shape and with higher throughput. For example, Zeisel *et al.*[9] used a chemical etching technique similar to that developed earlier by Pangaribuan *et al.*[8] for a photon scanning tunneling microscopy. The resultant fiber tips had a much shorter taper region and higher cone angle; they provided a three orders of magnitude higher throughput than normally obtained with pulled fiber probes. In another experiment Islam and co-workers[11] fabricated hybrid pull-etch tapered probes with throughput four orders of magnitude higher than that of pulled fibers.

The process of applying a metallic overcoat to the tip is an equally important aspect of fabricating high-resolution NSOM probes.[4] Through the addition of an opaque metallic coating such as aluminum that covers the sidewalls of the tapered fiber, a tiny aperture at the end of the fiber is created. The usual process for coating the tip is through vacuum deposition of aluminum by thermal evaporation while the tip is rotated and held at an angle to the source. The exposed

glass fiber end resulting in this manner is generally located inside the metallic aperture, is partially obstructed by rough aluminum grains situated near the aperture boundary, and often contains aluminum protrusions, as evidenced by numerous scanning electron microscope (SEM) images of fiber tips.[12,13] This may contribute to the poor polarization capabilities of the majority of fiber tips prepared by angled evaporation.[14] A larger than optimal separation of fiber tip and sample and the absence of a clean opening result in lower throughput of the probe and poor optical resolution of the NSOM. Furthermore, the angle-evaporation procedure is very time consuming and may not result in the fabrication of a batch of reproducible and well-defined apertures of desired diameter. In addition, other problems associated with angle evaporation are the fabrication of a special holder to accommodate many fibers with adjustable tilt angle, the loading of the probes, rotation of the tips about their axis during the coating operation, and keeping the fibers untangled throughout the coating procedure.

It is the aim of this work to develop a method for fabricating clean, well-defined, and highly reproducible subwavelength apertures for NSOM applications using a focused ion-beam (FIB) milling technique. Fiber probes were produced through the use of a heating–pulling process and by adjusting the parameters described by Valaskovic *et al.*[4] for obtaining probes of optimum shapes and throughputs. The pulled fiber probes were then uniformly coated all over with a 100–150 nm aluminum film in batches of 10–15 fibers
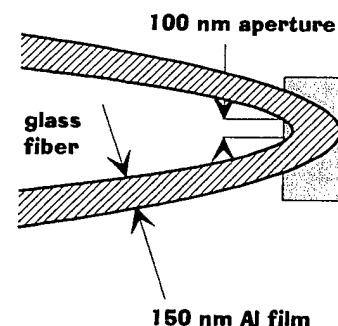

FIG. 1. Schematic diagram of the FIB milling procedure to produce a near-field aperture. The rectangular shaded region represents the area in which the ion-beam raster scans over the tip from right to left in order to remove material cleanly.

---

[a]Present address: Bragg Grating Technologies, 3M Specialty Optical Fibers, 206 West Newberry Rd., Bloomfield, CT 06002-1331.
[b]Also with the Institute for Plasma Research, University of Maryland.
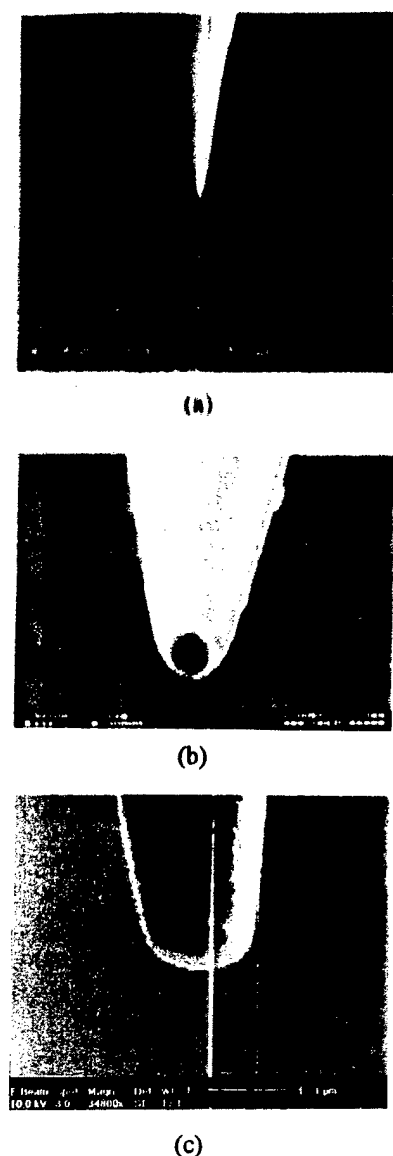[c]Electronic mail: davis@eng.umd.edu

(a)

(b)

(c)

FIG. 2. SEM photographs of the near-field optical fiber probe (a) before FIB milling (bar=2 μm), (b) after FIB fabrication of a 100 nm diam aperture (bar=1 μm), and (c) after FIB fabrication of a 300 nm diam aperture (bar=1 μm).

with a sputtering unit (Edwards Xenosput XE200) usually used to metal coat specimens prior to inspection by scanning electron microscopy. The coating is smooth and exhibits no leakage or pin holes upon injection of laser light into such fiber probes.

In order to use the tips in a near-field microscope, a subwavelength opening at the apex of the probe must be formed. We have used FIB milling to fabricate an aperture of desired diameter at the very end of the metal coated fiber. The FIB system used was a FEI Dualbeam 620 FIB/SEM workstation (30 keV 30 keV Ga$^+$ ions, minimum spot size 5 nm). The electron beam of the system imaged the profile and diameter of each individual tip in the batch containing 5–10 fibers positioned inside the chamber. To remove the metal coating and thus fabricate the aperture, the ion beam was raster scanned in a rectangular pattern at the apex of the fiber, as represented by the shaded region in Fig. 1. In contrast to simply cutting off the end of the fiber in one sweep
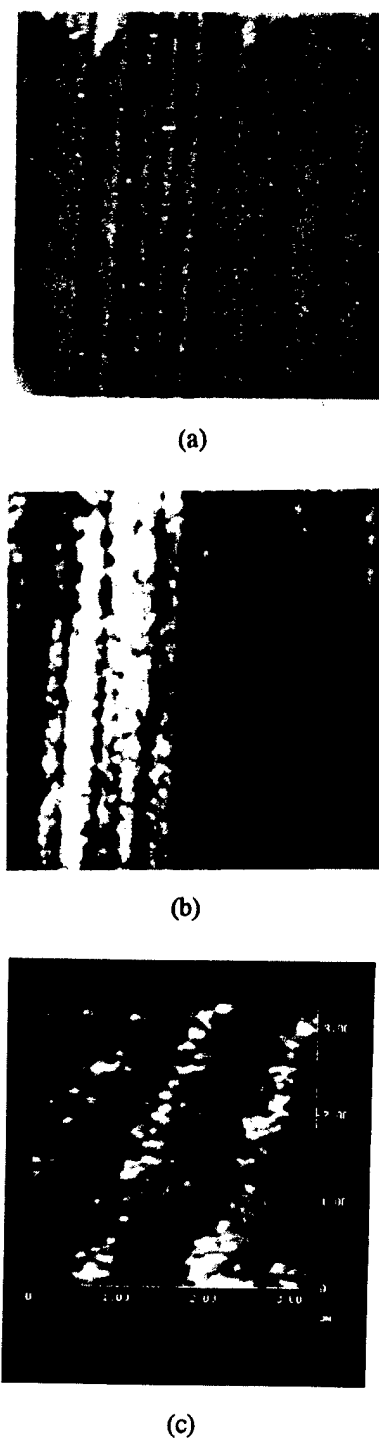

(a)

(b)

(c)

FIG. 3. Simultaneous (a) shear-force topographical and (b) near-field optical images of a 10×10 μm^2 region of a test sample using the 100 nm aperture diameter FIB fabricated fiber probe. An expanded view of a region (3.25 ×3.25 μm^2) of the 100 nm lines is shown in (c).

with the FIB, which would result in redeposition of material onto the aperture, this procedure completely removes the material at the end of the fiber.[15] By varying the size of the rectangular scanned region and with knowledge of the coating thickness and fiber end diameter, we can precisely make a clean-cut aperture of the desired diameter and optical throughput suitable for a variety of NSOM applications.

Figure 2(a) shows a SEM image of a tapered fiber probe coated with 150 nm of aluminum. The aperture is then

Appl. Phys. Lett., Vol. 72, No. 24, 15 June 1998

Pilevar *et al.* 3135

formed with the aforementioned FIB milling procedure creating an extremely well-defined 100 nm diam opening, as shown in Fig. 2(b). Figure 2(c) shows another aluminized fiber tip milled by the FIB to make a 300 nm diam aperture. The entire FIB milling time for each tip was between 2 and 3 min. As revealed in Fig. 2, the fabricated near-field apertures are, to the authors' best knowledge, the best-defined and clean-cut ones ever fabricated. In contrast to angled metal evaporation, the FIB milling procedure removes any rough aluminum grains at the tip end surrounding the aperture. The advantages of this are twofold: the optical through-put is improved and the aperture can give the true near-field optical contrast of a sample without the influence of tip protrusions.

The limitations of our FIB tip aperture fabrication technique involve the coating uniformity, tip geometry, tip charging under ion imaging, and the ion-beam profile. An rf sputterer was used to achieve a smooth and uniform coating over the tip so that for a known coating thickness, one can cut the aperture to a desired diameter. Clearly, nonuniformity of the coating can lead to errors in the desired aperture diameter. Tip geometry is also a factor since a high aspect ratio tip will allow for more precise control of the final aperture diameter (this is especially important for fabrication of apertures smaller than 100 nm). A tradeoff must be struck, however, because high aspect ratio tips have less throughput because the evanescent wave propagates through a longer region. Our FIB has a Gaussian profile with a minimum 5 nm spot size, allowing for precise aperture milling of even ultrahigh aspect ratio tips. A final important consideration is the grounding of the tip to avoid charging while imaging. This was accomplished using a small amount of silver paint, which was then easily removed with acetone.

FIB fabricated fiber probes were tested in the near-field system developed in our laboratory. Near-field distance regulation is maintained through the use of shear force phase-locked tuning fork feedback.[16] The sample imaged was a series of lines of various widths (1 μm–100 nm) milled by the FIB through a 50 nm aluminum film coated on a glass substrate. The sample was imaged using a FIB milled fiber tip of 100 nm aperture diameter in our NSOM setup operating in collection mode using a He–Ne laser source (λ=633 nm). In Figs. 3(a) and 3(b), we show the topographical and near-field optical images of a 10×10 μm^2 region of the sample, respectively. The smallest line imaged at the left-most area is approximately 100 nm wide. A magnified near-field image of the sample showing optically resolved lines of less than 200 nm is shown in Fig. 3(c). Because the probe end is flat and free of aluminum protrusions, the optical con-

trast is much less affected by topographically induced intensity changes.[17] Thus, the optical images in Figs. 3(b) and 3(c) yield optical resolution of about 100 nm (when 100 nm width of the test line itself is taken into account), as expected for the fabricated 100 nm aperture. The signal-to-noise ratio in the optical image is rather low because the sample itself defines an aperture smaller than the wavelength with a thickness of 50 nm. Thus, the optical image is taken in a situation that is equivalent to a double pass through the NSOM tip.

In conclusion, we have implemented a FIB technique to fabricate well-defined near-field apertures of desired diameters that exhibit improved features over the conventional angled metal evaporation method. Currently under investigation is the use of FIB milling applied to chemically etched fiber probes, which has the potential for creating a probe with a much higher optical throughput and smaller aperture. This combined technique could boost the optical signal by orders of magnitude and improve NSOM resolution significantly.

[1] D. W. Pohl, W. Denk, and M. Lanz, Appl. Phys. Lett. 44, 651 (1984).
[2] E. Betzig, J. K. Trautman, T. D. Harris, J. S. Weiner, and R. L. Kostelak, Science 251, 1468 (1992).
[3] E. H. Synge, Philos. Mag. 6, 356 (1928).
[4] G. A. Valaskovic, M. Holton, and G. H. Morrison, Appl. Opt. 34, 125 (1995).
[5] W. P. Ambrose, P. M. Goodwin, J. C. Martin, and R. A. Keller, Science 265, 364 (1994).
[6] A. Shchemelinin, M. Rudman, K. Liberman, and A. Lewis, Rev. Sci. Instrum. 64, 3538 (1993).
[7] E. Betzig, J. K. Trautman, R. Wolfe, E. M. Gyorgy, and P. L. Finn, Appl. Phys. Lett. 61, 142 (1992).
[8] T. Pangaribuan, K. Yamada, S. Jiang, H. Ohsawa, and M. Ohtsu, Jpn. J. Appl. Phys., Part 1 31, 1302 (1992).
[9] D. Zeisel, S. Nettesheim, B. Dutoit, and R. Zenobi, Appl. Phys. Lett. 68, 2491 (1996).
[10] R. U. Maheswari, S. Mononobe, and M. Ohtsu, Appl. Opt. 35, 6740 (1996).
[11] M. N. Islam, X. K. Zhao, A. A. Said, and C. F. Vail, Conference on Lasers and Electro-Optics (Optical Society of America, Washington, DC, 1997), Vol. 11, p. 70.
[12] E. Betzig and J. K. Trautman, Science 257, 189 (1992).
[13] C. Obermuller and K. Karrai, Appl. Phys. Lett. 67, 3408 (1995).
[14] C. Durkan, I. V. Shvets, and J. C. Lodder, Appl. Phys. Lett. 70, 1323 (1997).
[15] K. P. Muller and H. C. Petzold, Proc. SPIE 1263, 12 (1990).
[16] W. A. Atia and C. C. Davis, Appl. Phys. Lett. 70, 405 (1997).
[17] B. Hecht, H. Bielefeldt, Y. Inouye, D. W. Pohl, and L. Novotny, J. Appl. Phys. 81, 2492 (1997).

Apparent superresolution in near-field optical imaging of periodic gratings

Igor I. Smolyaninov and Christopher C. Davis

Department of Electrical Engineering, University of Maryland, College Park, Maryland 20742

A superresolution phenomenon in images of diffraction gratings obtained with a near-field optical microscope probe positioned at distances of the order of 1 μm from the surface was recently reported [Appl. Opt. **33**, 876 (1994)]. This experiment was interpreted in terms of evanescent waves observed in the far field. We show that the effect observed in that experiment is a very well known far-field optical phenomenon called the Talbot effect. The existence of self-imaging Talbot planes for gratings with periods of the order of a few micrometers appears promising for many practical applications. © 1998 Optical Society of America

OCIS codes: 180.5810, 070.6760.

Near-field scanning optical microscopy (NSOM) has become an important tool in surface studies.[1] However, in many situations the problems of the contrast mechanism and resolution of NSOM still require discussion. A recent overview of these questions is available.[2]

An interesting NSOM experiment was reported[3] that has given rise to ongoing discussion and controversy. A study of the imaging properties of the external-reflection NSOM setup was conducted with different diffraction gratings as samples. Surprisingly, the best profiles of a 1.6-μm-period rectangular diffraction grating were measured at a tip–surface distance of 0.7 μm. This experimental observation was used to justify a general theoretical claim that evanescent waves contribute to the radiation fields of sources and to the far fields of scatterers.[4] Recently Wolf and Foley demonstrated,[5] by considering a spherical scalar wave and a linear electric dipole field, that this claim is untrue. The only question that remains unanswered is: what was seen in the experiment? In this Letter we show that the superresolution observed in the experiment reported in Ref. 3 is a manifestation of a well-known far-field optical phenomenon called the Talbot effect.[6]

The Talbot effect exhibits itself when a grating is illuminated with a highly spatially coherent plane wave. Self-images of the grating are produced in certain planes behind and in front of the grating. These images are produced solely by free-space propagation of a diffracted optical field. Applications of the Talbot effect include optical image processing and production of optical elements (see, for example, Refs. 7 and 8).

The theory of the Talbot effect is most easily derived in the one-dimensional case. The scalar field behind an infinite grating with a period a positioned at the origin ($z = 0$), when the grating is illuminated by a plane wave, can be described by Fourier series:

$$E(x, z) = \sum_n C_n \exp(2\pi i n x/a)\exp(i k_n z),$$

$$k_n = 2\pi(1/\lambda^2 - n^2/a^2)^{1/2}. \quad (1)$$

The usual integer Talbot effect happens when $a \gg \lambda$ and $k_n z \approx 2\pi z/\lambda - 2\pi n^2(\lambda z/2a^2)$. Since the square

of an integer n is itself an integer, at $Z_t = 2a^2/\lambda$ all Fourier components of the optical field have exactly the same phase differences with respect to one another as they have at plane $z = 0$. Thus the field distribution of a grating reproduces itself. The same self-imaging is observed at distances that are integer multiples of the Talbot distance: $z = n Z_t$. More-complex field patterns occur at fractional values of the Talbot distance. These patterns are located at $z = (p/q)Z_t$, where p and q are integers. In the case of the fractional Talbot planes many Fourier components of the field (but not all of them) have the same phase differences with respect to one another, so the field pattern resembles (but does not exactly reproduce) the field distribution at $z = 0$.[7]

The experiment discussed in Ref. 3 and the Talbot effect observations have the following common features: (a) field distributions at some plane near gratings illuminated by spatially coherent sources are studied, and (b) sudden contrast enhancement or self-imaging occurs at a certain distance from the grating. The difference between these experiments is that in Ref. 3 $a \gtrsim \lambda$. Since the experimental geometry does not depend on the y coordinate, the optical field remains scalar, and Eq. (1) is still true in this case. But only a few terms in Eq. (1) are now propagating waves, and the rest are evanescent. Therefore we cannot use an expansion of $k_n z$ for small λ/a anymore. On the other hand, it is possible that at some modified Talbot distance Z_{tm} the phase differences among a small number of propagating Fourier terms will be exactly the same as in the plane $z = 0$. For this to occur the following condition must be satisfied:

$$(1/\lambda^2 - 1/a^2)^{1/2}Z_{tm} = (1/\lambda^2 - 2^2/a^2)^{1/2}Z_{tm} + n_2$$
$$= (1/\lambda^2 - 3^2/a^2)^{1/2}Z_{tm} + n_3 = \dots,$$

$$(2)$$

where n_2, n_3, etc., are different integer numbers. Equation (2) can have a number of solutions for Z_{tm} that are no longer periodically spaced. Nevertheless, the field distribution at the planes $z = Z_{tm}$ will possess the Talbot effect property of being self-focused.
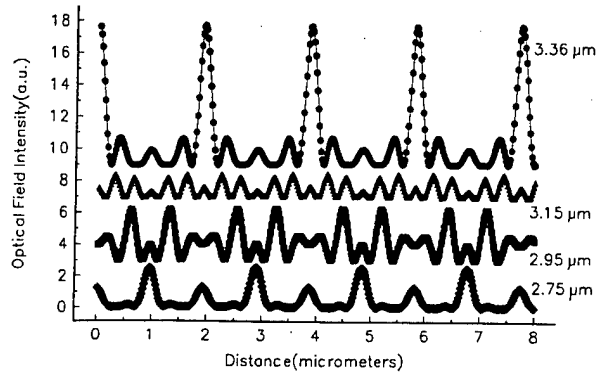
Fig. 1. Field distributions of a grating at different distances near the Talbot plane at $Z_{tm} = 3.36$ μm.

In the following example we show that Talbot planes can indeed appear near gratings with periods $a \sim \lambda$. To make the numerical analysis as simple as possible we consider a monochromatic ($\lambda = 0.633$ μm) plane wave propagating through a periodic set of narrow openings made in a plane opaque screen. To keep our considerations simple we assume that the period of the grating is slightly larger than 3λ and that the size of the openings is $d \ll \lambda$, so there are just three propagating Fourier components of the optical field behind the grating with approximately the same amplitude ($C_1 = C_2 = C_3$). Simple numerical calculations show that such a grating with a period $a = 1.936$ μm exhibits self-focusing at a distance $Z_{tm} = 3.36$ μm. In this case the integer numbers in Eq. (2) are $n_2 = 1$ and $n_3 = 4$. Optical field intensities calculated with Eq. (1) for different planes near the Talbot plane at $z = Z_{tm} = 3.36$ μm are shown in Fig. 1. The planes are selected far enough from the grating that there is no comparable contribution from the evanescent Fourier components of the diffracted field. Figure 1 shows a sudden self-focusing effect. The full widths at half-maximum of the periodic peaks of the optical field are equal to 0.23 μm = 0.36 λ. Here we should recall that the theoretical limit to the resolution of a near-field scanning microscope with un-

coated tapered optical fiber tips is $\lambda/3$.[9] Thus the experimental results obtained in the study with uncoated fiber tips reported in Ref. 3 no longer look surprising. While imaging gratings, one can expect to achieve optical resolution of the order of $\lambda/3$ in some Talbot planes in the far-field that are many micrometers away from the sample. Such results do not require any nontraditional explanation.

On the other hand, the existence of self-imaging Talbot planes for gratings with periods of the order of a few micrometers is itself an interesting phenomenon, since self-imaging can be used in many practical applications. For example, self-imaging can be used in the production of optical elements with much smaller features than those obtained with the usual integer or fractional Talbot effect.

In summary, we have shown that experimentally detected superresolution in near-field scanning microscopes working at micrometer distances from periodic gratings used as samples is a manifestation of the Talbot effect. Superresolution does not require an explanation involving unusual physics such as evanescent-wave detection in the far fields of scatterers.

References

1. D. W. Pohl and D. Courjon, eds., *Near-Field Optics* (Kluwer, Dordrecht, The Netherlands, 1993).
2. J. J. Greffet and R. Carminati, Prog. Surf. Sci. **56**, 133 (1997).
3. S. Bozhevolnyi, M. Xiao, and O. Keller, Appl. Opt. **33**, 876 (1994).
4. M. Xiao, Opt. Commun. **132**, 403 (1996); Chem. Phys. Lett. **258**, 363 (1996); J. Mod. Opt. **44**, 327 (1997).
5. E. Wolf and J. T. Foley, Opt. Lett. **23**, 16 (1998).
6. W. H. F. Talbot, Philos. Mag. **9**, 401 (1836).
7. A. W. Lohmann and J. A. Thomas, Appl. Opt. **29**, 4337 (1990).
8. K. Tatah, A. Fukumoto, T. J. Suleski, and D. C. O'Shea, Appl. Opt. **36**, 3577 (1997).
9. L. Novotny, D. W. Pohl, and B. Hecht, Ultramicroscopy **61**, 1 (1995).

Experimental study of probe–surface interaction in near-field optical microscopy

Igor I. Smolyaninov*, Walid A. Atia, Saeed Pilevar, Christopher C. Davis

Electrical Engineering Department, University of Maryland, College Park, MD 20742, USA

Abstract

The physical mechanism of shear-force interaction between a fiber tip and a sample in near-field optical microscopy has been studied using tunneling current measurements between the tip and a sample. Optical and non-optical (tuning fork) shear-force distance controls have been used. In both cases a tunneling current between the tip and the sample has been detected at the very beginning of shear-force approach curve when the amplitude of tip vibration was just slightly smaller than its initial value. These results indicate that fiber-tips generally mechanically touch samples under shear-force distance feed-back control. © 1998 Elsevier Science B.V. All rights reserved.

PACS: 07.79.Fc

Keywords: Near-field microscopy; Shear-force distance control

1. Introduction

Shear-force distance control (SFDC) is commonly used in near-field optical microscopy. It is based on a decrease in the oscillation amplitude of a resonantly dithered tapered fiber during its approach to a surface. The nature of SFDC has been the subject of ongoing discussion, since it is used with equal success in air, in ultra high vacuum, and in superfluid helium. This "universal" nature of the shear force suggests some common physical mechanism of fiber tip damping in these different environ-

ments. Several possible interaction mechanisms have been suggested to contribute to SFDC, such as capillary and van der Waals forces [1]. More recently it has been suggested that an effective non-linear bending force (NBF) connected with one-sided mechanical probe–surface contact is a main source of the shear-force [2]. The latter mechanism could be the "universal" one that is common to all environments.

It is possible to detect a mechanical contact between a conductive probe and a conductive sample by measuring the probe–sample electric resistance [3]. For relatively large tip–surface separations of several nanometers, the current increases exponentially with decreasing separation (at a fixed tunneling voltage). On further approach, a discontinuous

---

*Corresponding author. Tel.: + 1 301 4053255; fax: + 1 301 3149281; e-mail:smoly@eng.umd.edu

current jump is observed [4], which is attributed to mechanical instability caused by significant atomic motion under the influence of adhesive forces, initiating point contact between tip and sample [5]. The resistance of a point contact is determined by the Sharvin formula: $R_s = 4\rho l/3\pi a^2$ [3], where a is the radius of the contact area and l is the electron mean free path. The Sharvin formula is valid when $a \ll l$. For a contact of atomic dimensions one could expect resistance to be of the order of $R_s \sim 35$ KΩ. Thus, the value of tip–sample resistance indicates approximately the tip–sample distance and/or an area of tip–sample contact.

We have used regular STM tips (cut gold wires and electrochemically etched tungsten tips) and metal coated fiber-tips that are conventionally used in near-field scanning optical microscopy in the SFDC of our near-field microscope. Typical shear-force approach curves were observed together with the corresponding tunneling current measured between these tips and a freshly prepared thermally evaporated gold film used as a sample. Depending on the mechanical stiffness of the STM tip we observed both contact and non-contact van der Waals (or capillary) modes of SFDC operation. All the data indicate that metal coated fiber-tips mechanically touch samples under shear-force distance control.

2. Experimental setup

Two types of SFDC have been used in our experiments. In optical SFDC (Fig. 1a) a regular STM tip or metal coated fiber tip is attached to a piezotube that provides both XYZ motion in the nanometer range and dithers the tip at its resonant frequency. The vibration amplitude is detected with the help of a laser beam passing by the fiber near its tip in a direction perpendicular to the axis of the fiber. This beam is directed onto a pinhole covering a photodiode. The component of optical signal from the photodiode at the frequency of tip dithering is extracted using a lock-in amplifier and directed into the feedback loop. Typical eigenfrequencies of fiber tips are ~ 3 kHz. This value is limited by the lowest eigenfrequency of a piezotube, which is 4.5 kHz. The typical amplitude of tip
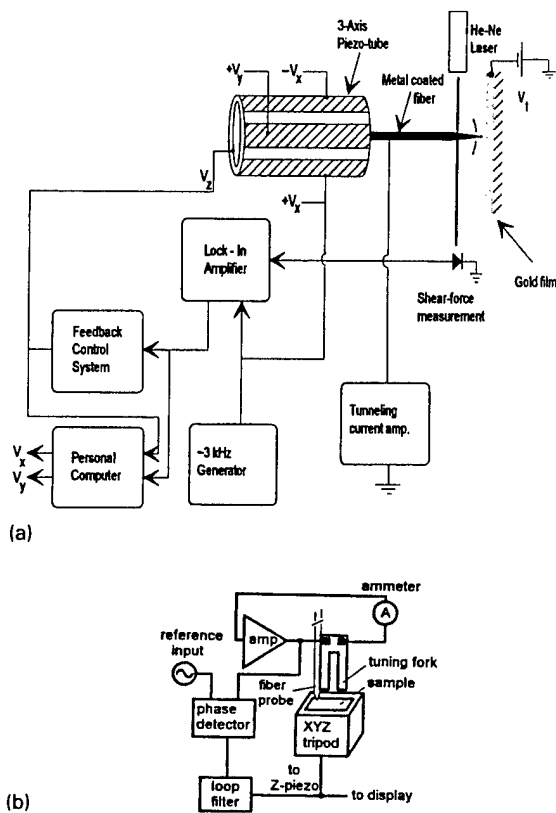

(a)

(b)

Fig. 1. Schematic diagrams of the optical (a) and non-optical (tuning fork) (b) SFDC setups.

vibration has been estimated from the dithering voltage and the Q-factor of the fiber tip to be 5–10 nm.

Alternatively, a non-optical SFDC [6,7] utilizing a quartz crystal tuning fork acting as a resonant vibration sensor has been implemented. A fiber tip is mounted on one of the prongs of the fork (Fig. 1b) to serve as both a shear-force pickup and a near-field optical probe. The crystal is driven at its resonance frequency (around 33 kHz) by another piezo crystal mounted next to the tuning fork. The current through the tuning fork is converted to a voltage and is fed back into the tip–sample distance control loop. Typical Q-factors of the fork with an attached fiber tip are on the order of 1000–2000. The tip vibrates with an amplitude of 0.5 nm during approach to the sample.

Two types of metal tips have been used in our experiments: freshly cut gold or gold–palladium wires with different diameters, and chemically etched tungsten tips. These metal tips were positioned in both optical and non-optical SFDC setups instead of fiber tips. Also, regular tapered fiber tips coated head-on with gold, gold-palladium, or chromium have been used. The choice of metal tips or metal coating is determined by the oxidization properties of metals in air. For the same reason, we used freshly prepared gold and gold-palladium films as samples. A voltage in the range 0.1–0.3 V is applied between the tip and the sample of the microscope and the current is measured under SFDC operation.

3. Results

As a first step in our experiment we used metal tips with different shapes and stiffness in an optical SFDC setup. Depending on the tip, we observed different shear-force approach characteristics and different behavior of the current between the tip and sample. Using soft 3 mm long 60 µm diameter cut gold wire in the optical SFDC setup we have observed an extended region of shear-force sensitivity without any tip–sample current (Fig. 2a). These data have been recorded while the tip moved away from the sample. A region of shear-force sensitivity extending out to 400 nm indicates capillary force to be responsible for tip damping. A similar extended range (~240 nm) of tip-sample force sensitivity in a soft AFM sensor under ambient conditions has been reported in [8], and the capillary nature of this force has been clearly demonstrated. The shape of the cut gold tip may contribute to its increased sensitivity to viscous forces and give rise to a very long shear force approach curve.

Stiffer metal tips and metal coated fiber tips exhibit different behavior (Fig. 2(b)). The range of shear-force damping is much shorter (on the order of 20–30 nm). The force from the capillary water layer is not enough to substantially attenuate tip vibration. Unlike Fig. 2a, we observe a tip–sample current right from the very beginning of the shear-force approach curve when the amplitude of tip vibration is slightly smaller than its initial value.
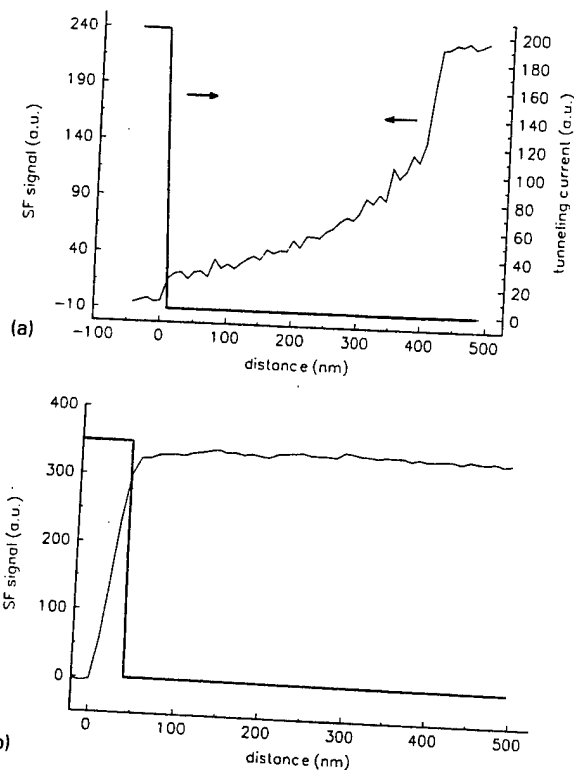

Fig. 2. Simultaneously measured shear-force damping and tunneling current (bold line) dependences on the tip–sample distance. The tips used are: (a) a cut gold wire with the tip length 3 mm, diameter 60 µm, tip eigenfrequency 1.898 kHz; (b) chromium coated single-mode fiber with the length 6 mm, diameter 125 µm, eigenfrequency 2.302 kHz.

The current appears around the 0.9 level of maximum shear-force signal, which is the largest set point we can achieve for our signal to noise ratio. This level varies with the freshness and cleanliness of the sample and the tip. Freshly prepared metal film absorbs water very fast. But over time it can also absorb oil and any other vapor that is present in the laboratory. The current may appear only at much lower level of shear-force signal if the experiment is not done carefully enough and the tip and sample are dirty.

The current curve is saturated in both figures. It is difficult to avoid saturation of the current preamplifier because of the exponential dependence of tunneling current on the tip–sample distance. These curves give only a qualitative impression on the current behavior since the tip–sample current is not
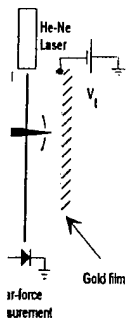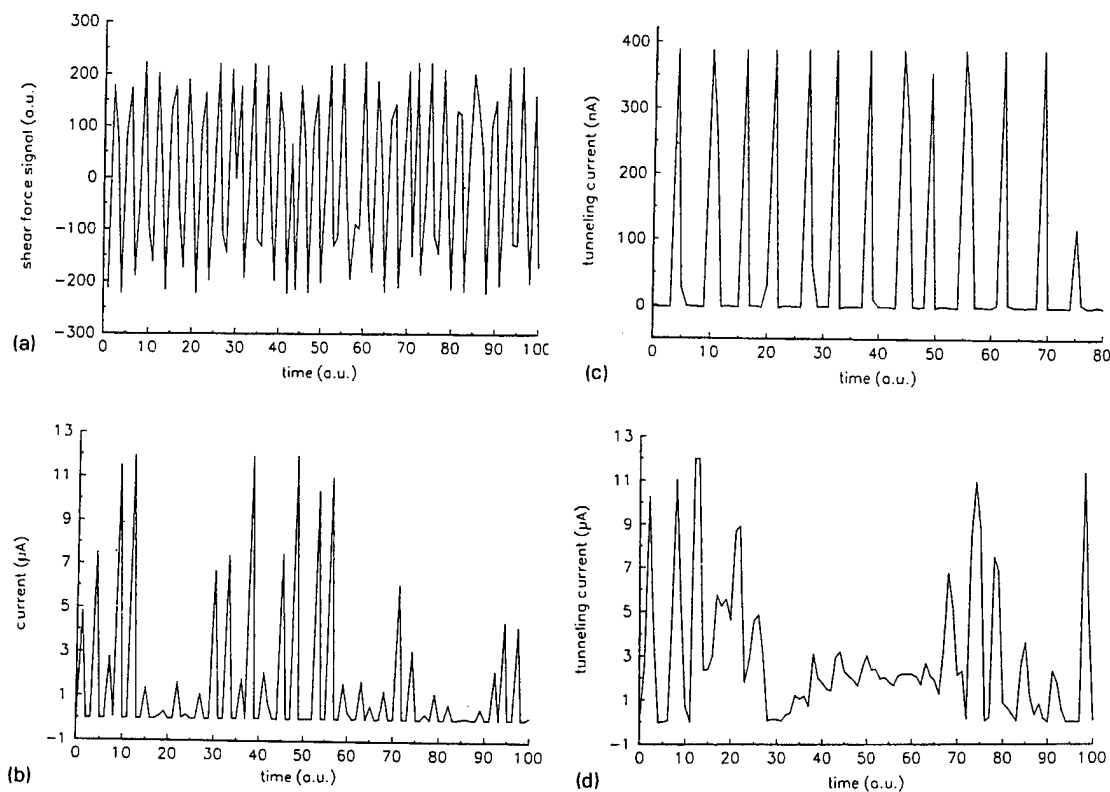
Fig. 3. Time scans of the optical shear-force signal (a) and the tip–sample current (b) measured simultaneously using a tungsten STM tip in the optical SFDC setup. Electrochemically etched tungsten tip (eigenfrequency $v = 4.288$ kHz) and a gold film sample have been used. SFDC level is 0.90. Period of oscillations in (a) is equal to v^{-1}. (c) and (d) are the time scans of a current between a chromium coated fiber tip and a gold sample at 0.90 and 0.82 level of SFDC. Period of oscillations in tunneling current is again equal to the period of fiber tip oscillations.

steady. Fig. 3 shows time scans of current measured with a tungsten STM tip and a chromium coated fiber tip under optical SFDC. The spikes of current indicate that tips are actually knocking on the sample during SFDC feed back. The tip–sample resistance in the peaks of current in Fig. 3b and Fig. 3d is measured to be around 30 KΩ. This value is of the order of magnitude of the resistance of an "atomic" point contact according to Sharvin's formula. However, the current may flow through a thicker layer of contaminations on the surface of the metal film. In any case, all these data support the nonlinear bending force hypothesis [2] for the shear-force. Yet another paper supporting the idea of mechanical tip contact has been presented in this conference by Wei and Fann [9].

The drawback of our optical SFDC, which is common to most other types of optical SFDC is the rather large amplitude of tip vibration in free space. Non-optical SFDC using a tuning fork as a sensitive element offers an improvement in this respect. The vibration amplitude of a tuning fork ($x \sim$ 0.5 nm) is an order of magnitude smaller. Despite its stiff spring constant (typically 20 000 N/m) keeping the Q-factor of the fork high, on the order of 1000–2000, makes it dynamically soft ($k/Q \sim$ 10 N/m), although it is still stiffer than a typical fiber tip probe with $Q = 50$ and $k/Q \sim 2$ N/m. Nevertheless, an actual force acting on the tip ($\sim kx/Q$) is about the same in both SFDC setups. The approach curve of a tuning fork SFDC setup is shown in Fig. 4.
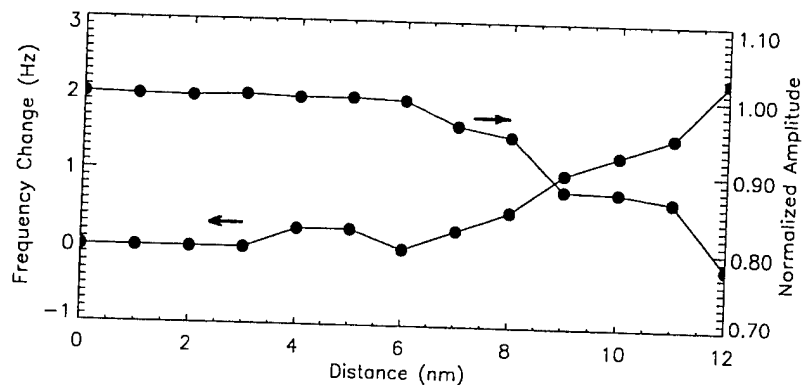
Fig. 4. Simultaneous amplitude and frequency deviation of the tuning fork oscillator upon approach to the sample. Within 6 nm from the interaction area, the amplitude decays by over 20% while the frequency increases by 2.3 Hz. The Q-factor is 2100.

We have used tapered single mode optical fibers coated "head-on" with 200 nm of gold–palladium in our tunneling experiment. We were able to run SFDC feed back at the level of 99.9% of the initial undamped shear-force signal. Moreover, the sensitivity of the SFDC has been increased by moving the driving signal slightly off resonance (by slightly modifying our experimental setup in Fig. 1b). Nevertheless, we always see spikes in the tunneling current of the kind shown in Fig. 3. This indicates that the tip is knocking on the sample in the tuning fork SFDC setups. One has to be careful running this experiment. A gold or gold–palladium coating does not stick really well to the fiber. It is easy to rip off the coating from the very end of the fiber tip. On a number of occasions we did not observe a tip–sample current under SFDC or only observed it for larger tuning fork damping (for example at 70% of the initial shear-force signal). In all these cases careful study of the tip coating revealed tip damage as shown in Fig. 5a. This damage was not due to any drawback in the feed-back control system. The vertical fluctuations of the piezo when the feed-back control was on were less than 1 nm.

It should be noted that an aluminum coating does stick well to the fiber. It is possible to run tuning fork SFDC with much larger damping without causing physical damage to the coating. Fig. 5b shows the very end of an aluminum coated fiber tip after scanning. This tip was used in the

Fig. 5. Electron microscope images of (a) a gold–platinum coated tip that did not reveal any tunneling current under SFDC and (b) an aluminum coated fiber tip after scanning.
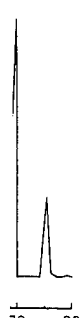
same conditions as the tip in Fig. 5a. No damage is apparent in this photo.

All our data indicate that the tip of a near field microscope is knocking on the sample under SFDC feed back. This is the "universal" physical mechanism behind the shear-force in all environments. There is nothing surprising in this fact, since for example AFM is a contact scanning probe microscope as well. However, we should point out the following important consequences of our observations:

(1) One should not believe shear-force approach curves. They cannot give the actual distance between the tip and a sample.

(2) It is much safer to work at the smallest possible shear-force damping, since in this case there is much less probability of damage to a tip aperture or of scratching a sample.

(3) It is important to look at the tip aperture not only before scanning but after scanning as well.

References

[1] R. Toledo-Crow, P.C. Yang, Y. Chen, M. Vaez-Iravani, Appl. Phys. Lett. 60 (1992) 2957.
[2] M.J. Gregor, P.G. Blome, J. Schofer, R.G. Ulbrich, Appl. Phys. Lett. 68 (1996) 307.
[3] R. Wiesendanger, Scanning Probe Microscopy and Spectroscopy, Cambridge University Press, Cambridge, 1994, p. 201.
[4] J.K. Gimzewski, R. Moller, Phys. Rev. B 36 (1987) 1284.
[5] J.B. Pethica, A.P. Sutton, J. Vac. Sci. Technol. A 6 (1988) 2490.
[6] K. Karrai, R.D. Grober, Appl. Phys. Lett. 66 (1995) 1842.
[7] W.A. Atia, C.C. Davis, Appl. Phys. Lett. 70 (1997) 405.
[8] A.L. Weisenhorn, P.K. Hansma, T.R. Albrecht, C.F. Quate, Appl. Phys. Lett. 54 (1989) 2651.
[9] P.K. Wei, W.S. Fann, Ultramicroscopy 71 (1998) 159.

On the spatial resolution of uncoated optical-fiber probes in internal reflection near-field scanning optical microscopy

Walid A. Atia[a],*, Saeed Pilevear[a], Ali Güngör[b], Christopher C. Davis[a]

[a] *Electrical Engineering Department, University of Maryland, College Park, MD 20742, USA*
[b] *Uludag Üniversitesi, Fen-Edebiyat Fakültesi, Fizik Bölümü, Görükle-Bursa, Turkey*

Abstract

We present conclusive experimental quantitative evidence of the resolution limit of uncoated optical fiber probes in the internal reflection mode. Additionally, we present a new technique for unambiguously determining the resolution of a near-field scanning optical microscope without topographical influences. A sample with nearly no topography but with a large dielectric step junction was created by evaporating a thin chromium layer on a silicon wafer and subsequently cleaving the wafer. The cleaved edge is then scanned over the step junction, allowing a quantitative determination of the lateral resolution without topographical influences. © 1998 Elsevier Science B.V. All rights reserved.

1. Introduction

In most near-field microscopes, the sides of a tapered optical fiber are coated with metal to prevent side leakage and thus confine the beam to only the aperture's size, since side leakage would severely degrade the lateral spatial resolution in collection or reflection near-field scanning optical microscopy (NSOM). Indeed, when the fiber diameter goes below half a wavelength, the HE_{11} mode is no longer confined by the waveguide and is essentially ejected from the core [1]. However, if the fiber tip is used both as source and detector (the so-called internal reflection mode), the double pass through the aperture effectively produces a system where the point-spread function of the uncoated aperture is traversed twice, eliminating a large part of the unwanted background radiation.

Several claims have been made regarding the resolution of uncoated optical fibers in the internal reflection configuration [2–8], but these are at best qualitative estimates that may be seriously exaggerated as a result of the topographical contrast present in the samples. Indeed, a recent investigation [9] of the internal reflection mode revealed that the same group's claim of better than 70 nm ($\lambda/7$) resolution [4,5] with uncoated fibers was simply a topographical artifact. A fluorescence measurement using uncoated fiber probes in the internal-reflection mode estimates the lateral resolution to be about 200 nm ($\lambda/3$) by measuring the intensity profile at a fluorescent film edge [10], but this estimate may also be affected by the topography of the fluorescent film. The most popular technique involving the use of a shadow mask [11]

---

* Corresponding author.

suffers from a large topographical element, and as such claims of resolution using this sample remain questionable.

The aim of the present work was to devise an experimental technique of determining the optical resolution of a near-field scanning optical microscope without the influence of topographically induced intensity changes that can give rise to a false high optical resolution. The described experimental technique can also be used to quantify the resolution of other near-field microscopes, including those using coated probes [12] and apertureless probes [13].

2. Experiment

A sample of virtually no topography but with a well-defined refractive index variation was constructed in order to quantify the lateral resolution of the uncoated fiber probe in the internal-reflection configuration. The sample we have used was a silicon wafer on which we have evaporated 500 nm of chromium and then cleaved perpendicular to the (1 0 0) plane in the [0 1 1] direction. We chose a thickness of 500 nm so that the chromium would not peel after cleaving. The cleaved edge

presents a nearly atomically flat junction between the silicon and the chromium that can be used as a step junction to determine the lateral resolution of the microscope. The sample is mounted at a slight tilt in order that the tip glide smoothly near the edge of the chromium region rather than catastrophically fall off. The measured length at which the optical signal rises to its half its maximum value gives a quantitative measure of the optical resolution. A shear-force mechanism using tuning-fork distance regulation [14] was used to insure that the tip was always in the near field of the sample. The vibration amplitude was set at less than 1 nm to insure that it did not contribute to any loss of resolution. Our tip diameter used was less than 100 nm determined through SEM imaging before and after scanning the junction.

3. Results and conclusions

In Fig. 1, we show a 2 × 2 μm scan of the cleaved Si-wafer edge where a region of chromium lies directly at the edge. The surface is representative of the shear-force topographical image while the shading is rendered by the near-field signal. A sudden change in slope occurs when the tip begins to
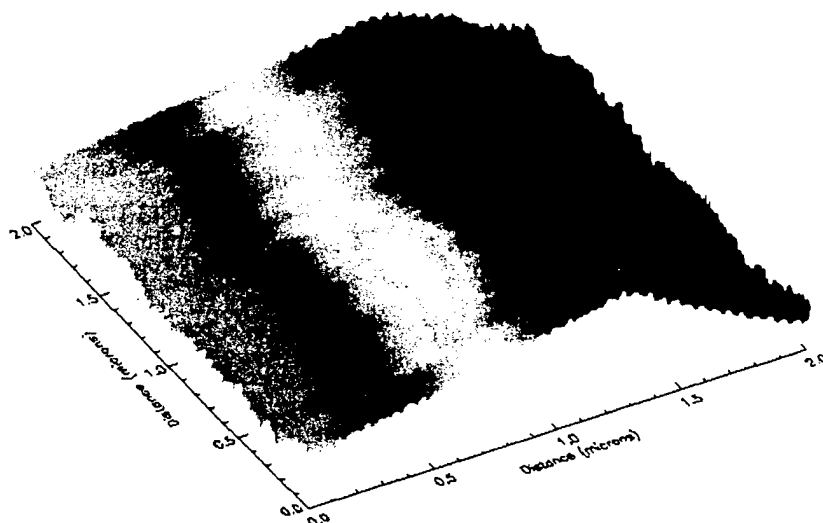

Fig. 1. 2 × 2 μm scan of the silicon–chromium interface. The surface topography is given by the shear-force signal, while the shading is rendered by the optical signal. The 500 nm chromium region is clearly resolved.
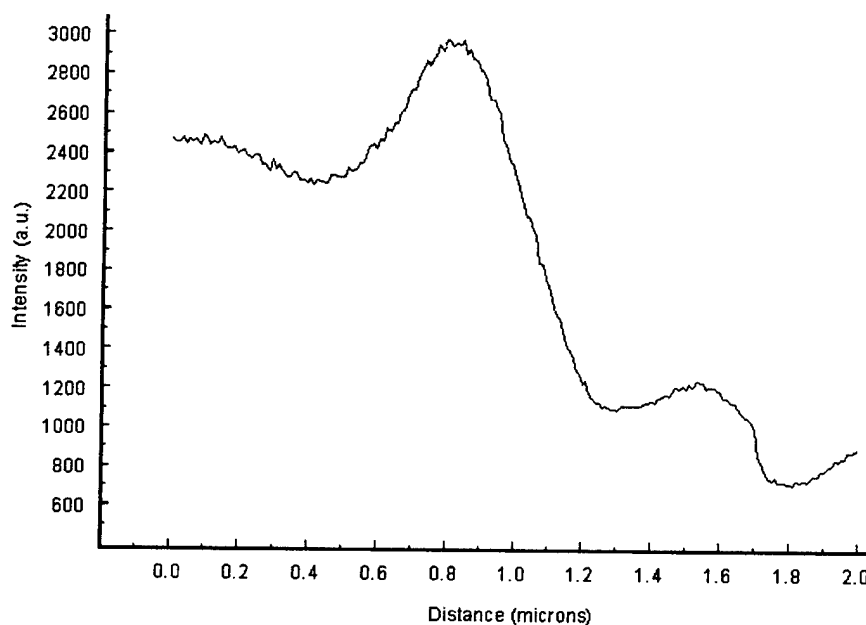
Fig. 2. Line scan of silicon–chromium cleaved-edge interface. The full-width half-maximum reveals a resolution of 300 nm.

fall off the edge of the chromium region; otherwise, there is no observable topography within the noise limit (< 3 nm) of our microscope. The entire height variation in Fig. 1 is only 30 nm, due to the tilt of the sample. As shown in the figure, the 500 nm region of the chromium is clearly resolved. A line scan of the optical signal through the region is shown in Fig. 2. From this scan, we can quantitatively deduce the resolution of the uncoated fiber probe in the internal-reflection mode to be about 300 nm ($\lambda/2.6$) (from the full-width at half-maximum taken from the baseline of the step transition before the edge), which is significantly better than the diffraction limit of 390 nm for our 780 nm wavelength source. We should also note that our best conventional microscope was not able to successfully image the chromium region. The variations before and after the chromium region are likely due to interference effects at the step junction and resemble a far-field microscope diffraction pattern generated at a step junction. A large background field generated by the uncoated fiber tip often gives rise to such imaging artifacts at a sharp junction. These effects may be eliminated by using

a coated fiber tip since such a source has a well-defined aperture.

In conclusion, we present quantitatively the resolution limit of uncoated fiber tips used in the internal-reflection configuration. The results agree well with recent experiments [9] that suggest the uncoated fiber configuration is nearly diffraction limited. Furthermore, we describe a new experimental technique for characterizing the optical resolution in a near-field microscope without the topographically-induced artifacts present in current resolution standards.

References

[1] E.L. Buckland, P.J. Moyer, M.A. Paesler, J. Appl. Phys. 73 (1993) 1018.
[2] D. Courjon, J. Vigoureux, M. Spajer, K. Sarayeddine, S. Leblanc, Appl. Opt. 29 (1990) 3734.
[3] M. Spajer, O. Bergossi, M. Guignard, Opt. Commun. 106 (1994) 139.
[4] G. Krausch, S. Wegscheider, A. Kirsch, H. Bielefeldt, J.C. Meiners, J. Mlynek, Opt. Commun. 119 (1995) 283.

[5] H. Bielefeldt, I. Horsch, G. Krausch, J. Mlynek, O. Marti, Appl. Phys. A. 59 (1994) 103.

[6] S.I. Bozhevolnyi, M. Xiao, O. Keller, Appl. Opt. 33 (1994) 876.

[7] G.A. Ensure, M. Holton, G.H. Morrison, J. Microsc. 179 (1995) 29.

[8] C. Durkan, I.V. Shvets, J. Appl. Phys. 79 (1996) 1219.

[9] V. Sandoghdar, S. Wegscheider, G. Krausch, J. Mlynek, J. Appl. Phys. 81 (1997) 2499.

[10] A. Jalocha, N.F. Van Hulst, Opt. Commun. 119 (1995) 17.

[11] U.C. Fischer, H.P. Zingsheim, J. Vac. Sci. Technol. 17 (1981) 881.

[12] E. Betzig, J.K. Trautman, T.D. Harris, J.S. Weiner, R.L. Kostelak, Science 251 (1991) 1468.

[13] F. Zenhausern, M.P. O'Boyle, H.K. Wickramasinghe, Appl. Phys. Lett. 65 (1994) 1623.

[14] K. Karrai, R.D. Grober, Appl. Phys. Lett. 66 (1995) 1842.

Near-field optical microscopy of two-dimensional photonic and plasmonic crystals

Igor I. Smolyaninov, Walid Atia, and Christopher C. Davis

Electrical Engineering Department, University of Maryland, College Park, Maryland 20740

(Received 10 June 1998)

Near-field optical images of electromagnetic mode structures in two-dimensional photonic and plasmonic crystals are presented. Interference patterns of plasmon Bloch waves in a plasmonic crystal have been observed. Fourier analysis of the photonic crystal images allows the reconstruction of the refractive index spatial distribution in the crystal. A similar procedure performed on images of a plasmonic crystal allows the recovery of parameters of the surface plasmon interaction with the periodic grooves that constitute the plasmonic crystal structure. [S0163-1829(99)13203-X]

INTRODUCTION

The optical properties of spatially periodic dielectric structures called photonic crystals have attracted much recent interest.[1] The analogy between electromagnetic wave propagation in multidimensionally periodic structures and electron wave propagation in real crystals has proven to be a valuable one. Electron waves traveling in the periodic potential of a crystal are arranged into energy bands separated by gaps in which propagating states are prohibited. Analogous band gaps exist when electromagnetic waves propagate in a periodic dielectric structure with a period comparable to the wavelength. These frequency gaps are referred to as "photonic band gaps." A demonstration of band structure effects in photonic crystals was in the microwave regime.[2] Recently, these effects have been measured in the near-infrared and visible regions.[3] Photonic crystals can have a profound impact in many areas of pure and applied physics. For example, inside a photonic band gap, optical modes, spontaneous emission, and zero point fluctuations are all absent.[1] From a practical point of view photonic crystals can be designed to transmit or reflect light within a specific range of frequencies, and their properties may be tunable by modification of their periodicity or refraction index.

Until recently photonic crystals have been studied by measuring their bulk optical properties. With the invention of the near-field scanning optical microscope[4] (NSOM) local microscopic properties of photonic crystals become accessible to experimental measurement. An application of NSOM techniques to characterize the local density of photon states and the electromagnetic mode structure of a two-dimensional photonic crystal has been reported in Ref. 5. In this work a photonic crystal was locally excited by light leaving a subwavelength aperture at the end of a metal-coated fiber tip. The light transmitted by the crystal was collected in the far field with a microscope objective. The numerical aperture (NA) of the objective was varied. Depending on the value of the NA, the transmitted light with different spatial momenta was integrated and recorded as a function of the position of the fiber tip. The contrast in the images obtained depended strongly on the region in the photon momentum space probed.

Theoretically this situation can be understood as follows: the photonic crystal was excited by a photon source that may be idealized as a δ function in coordinate space. The transmitted light was analyzed as a function of the absolute value of its momentum and the spatial position of the light source. A complicated theoretical model has to be used in order to analyze this experiment.

In the present work we study an alternative approach to the near-field optical characterization of photonic crystals. We suggest exciting the crystal with an incident laser beam. This may be idealized as an excitation by a δ function in momentum space. We use NSOM in the transmission mode to measure directly the local electromagnetic mode structure on the surface of a photonic crystal in coordinate space. The NSOM images are Fourier analyzed in order to extract information on the band-gap structure and refractive index distribution in the photonic crystal. We show this approach to be straightforward and simple.

We also apply our technique to the study of a two-dimensional "plasmonic crystal": a gold-coated rectangular bigrating, which possesses properties similar to the properties of a photonic crystal. Far-field optical properties of similar plasmonic crystals have been studied very recently[6] but no near-field studies of such crystals have been reported to date.

The surface plasmon (SP) is a fundamental electromagnetic excitation mode of a metal-dielectric interface.[7] The SP is free to propagate along the metal surface, but its field decays exponentially in both media in the direction perpendicular to the interface. Thus the spatial distribution of the SP field is inaccessible to far-field optical techniques. The development of NSOM has created ways to probe the SP field directly. SP propagation along the interface has been imaged in Ref. 8. SP scattering by *in situ* created individual surface defects has been studied and some prototype two-dimensional optical elements able to control SP propagation have been demonstrated.[9,10]

A periodic array of defects in the metal-dielectric interface should exhibit the properties of a two-dimensional "plasmonic crystal" when the periodicity of the structure is comparable with the wavelength of the SP. A complicated system of band gaps has indeed been measured in Ref. 6 using different bigratings. In the present paper we report our measurements of the local electromagnetic mode structure of a plasmonic crystal and derive some parameters of SP interaction with defects that constitute the bigrating. We present a

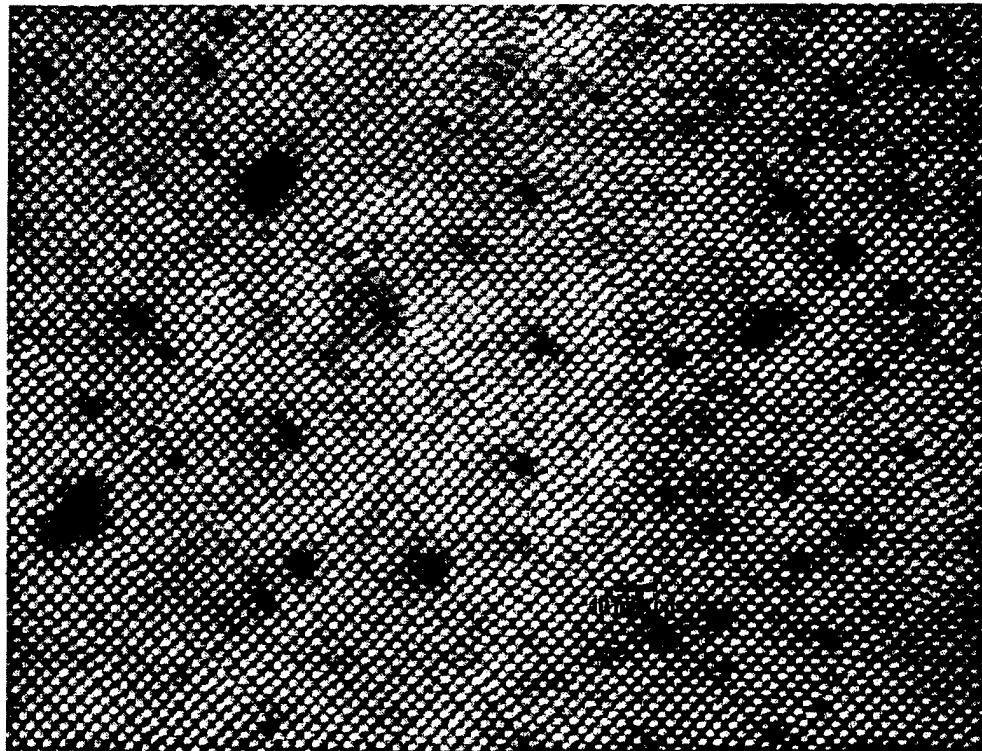   PRB 59   2454

FIG. 1. Far-field transmission image of the photonic crystal structure taken with an optical microscope using bottom face illumination with white light.

similar description of the results obtained with two-dimensional photonic and plasmonic crystals.

EXPERIMENTAL SETUP AND SAMPLES

We have studied two different kinds of photonic band-gap structures. The first sample studied is similar to the photonic crystal used in Ref. 5. It is a fiber bundle obtained from Schott Glass Technologies, Inc. made of two glasses with similar indices of refraction. The bundle is a two-dimensional rectangular lattice of glass with a higher refractive index embedded in a matrix glass with a lower refractive index. The period of the structure is approximately 3 μm. Figure 1 shows an image of a top face of the sample taken with a conventional optical microscope using bottom face illumination with a white light source. The image shows good periodicity of the structure although some dislocations and blemishes are present. Both faces of the sample are polished. The thickness of the sample is about 100 mm.

The second sample is a gold-coated two-dimensional rectangular calibration grating with a period of about 1 μm obtained from Digital Instruments, Inc. An atomic force microscope image of the sample surface is shown in Fig. 2. According to the manufacturer, a 30-nm layer of gold has been deposited by thermal evaporation on top of a glass grating coated with 800 nm of aluminum and 4 nm of chromium. In the absence of grooves such a "sandwich" structure supports surface plasmon propagation with a spectrum close to the spectrum of SPs on the surface of an infinitely thick flat gold sample. (The decay length of the SP field inside gold is about $l = \lambda/2\pi\epsilon_{Au}^{1/2}$.[7] At a wavelength of 633 nm this gives $l = 36$ nm.) The grooves scatter the SP field in the plane of propagation. Also they couple the SP field to photons in free

space. Since the period of the structure is comparable with the wavelength of plasmons: $\lambda_p = \lambda[(\epsilon_{Au}+1)/\epsilon_{Au}]^{1/2} = 590$ nm, where $\lambda = 633$ nm is the wavelength of light in air, this sample must behave as a "plasmonic crystal." There should be forbidden gaps in the SP momentum space. The spatial topology of such SP forbidden gaps in a similar rectangular bigrating has been studied in Ref. 6.

Our NSOM setup is described in detail in Ref. 10. It allows us to measure simultaneously surface topography using optical shear-force feedback,[4] and the spatial distribution of the optical signal in near-field proximity to the sample surface. In order to study the samples described, our experimental setup has been modified as follows [Figs. 3(a) and 3(b)]. The photonic crystal from Fig. 1 has been studied using NSOM working in a transmission mode as shown in Fig.
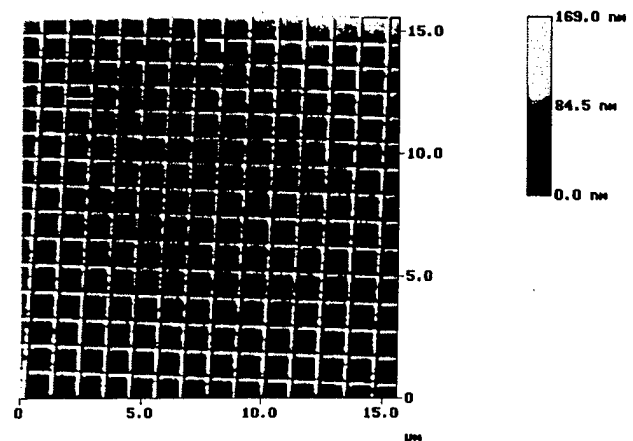

FIG. 2. Atomic force microscopic image of the plasmonic crystal surface topography.
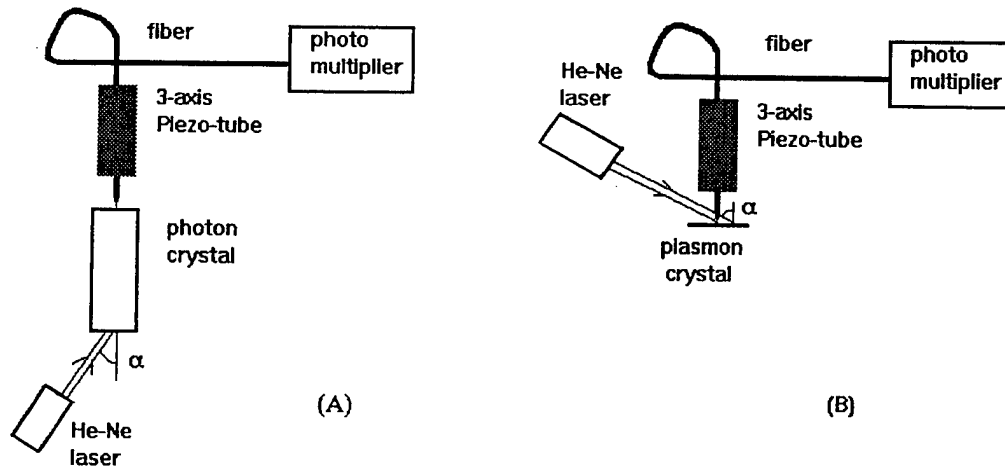
FIG. 3. Experimental setups for studying optical properties of (a) the photonic crystal and (b) the plasmonic crystal.

3(a). The angle of the bottom face illumination was varied and the field distribution on the top face was studied as a function of this angle.

The SPs on the surface of the plasmonic crystal from Fig. 2 were excited in reflection [Fig. 3(b)]. It is impossible to excite a SP wave on the flat gold-air interface by illumination of the surface from air. At a given frequency the momentum of photons in air is smaller than the momentum of plasmons. The presence of the periodically spaced grooves leads to a modification of the momentum conservation law: integer multiples of the reciprocal lattice vectors of the big-rating can be added to the photon and plasmon momenta. This leads to the possibility of SP excitation by photons illuminating the bigrating at certain resonant angles. Accordingly, the angle of sample illumination was varied in the experimental geometry shown in Fig. 3(b) in order to achieve SP excitation. P-polarized light from a He-Ne laser has been used. The SP field distribution has been measured using an uncoated tapered fiber tip in our NSOM. Although the resolution of a NSOM is higher when metal-coated tips are used,[4] an uncoated fiber tip introduces a much smaller perturbation in the SP field distribution.[10] This results from the much smaller difference between the dielectric constants of the glass tip and air ($\epsilon_{tip}-1$) in comparison with the difference between the dielectric constants of air and metal.

PHOTONIC CRYSTAL IMAGING

Near-field optical images of the photonic crystal sample obtained at different angles of excitation are shown in Figs. 4(a)–4(c). The topographical images taken simultaneously show no features higher than 10 nm and do not correlate with the optical ones. The optical images in Fig. 4 exhibit general periodicity of the refractive index structure (a 3-μm period in both directions). Some distortions in the images may be attributed to the dislocations observed in Fig. 1.

The main feature of these images is an appearance of additional periodicity and a richer spatial frequency spectrum at larger excitation angles. This feature is quite clear from the Fourier spectra presented in Figs. 5(a) and 5(b). Such behavior is easy to understand when the general theory of a photonic band-gap material is applied to our particular case (an extensive theoretical description of two-dimensional photonic crystals can be found in Ref. 11).

When a monochromatic electromagnetic wave of frequency ω propagates in a dielectric medium with a periodic dielectric constant $\epsilon(\mathbf{r})=\epsilon_0+\epsilon_1(\mathbf{r})$ (ϵ_0 is an average dielectric constant of a medium), the classical wave equation may be written in a form resembling the Schrödinger equation:

$$-\nabla^2\mathbf{E}+\vec{\nabla}(\vec{\nabla}\mathbf{E})-\omega^2\epsilon_1(\mathbf{r})\mathbf{E}/c^2=\epsilon_0\omega^2\mathbf{E}/c^2. \qquad (1)$$

In this equation $\epsilon_1(\mathbf{r})$ plays a role analogous to the periodic potential $U(\mathbf{r})$ in the Schrödinger equation for an electron in a crystal. In the two-dimensional crystal under consideration the photon motion may be decomposed into the motion in a periodic potential (perpendicular to the fiber bundle axis) and the free motion along the structure with momenta $k_\perp$ and $k_\parallel$, so that $k_\parallel^2+k_\perp^2=\epsilon_0\omega^2/c^2$. Thus larger excitation angles correspond to a larger momentum of motion in a periodic potential. Consequently, higher harmonics may be expected in the near-field image. To some extent our data are similar to the images of metal or semiconductor crystals obtained in scanning tunneling microscopy with different tunneling voltages applied. In both cases one can vary the particle (electron or photon) energy in the periodic potential as a free parameter.

The intensities of different spectral peaks in Fig. 5 contain information about the periodic part of the dielectric constant $\epsilon_1(\mathbf{r})$ of the photonic crystal. The Bloch theorem can be used in order to extract this information. Exact theory[11] gives slightly different equations for different polarization states of the electromagnetic field in the two-dimensional photonic crystal. On the other hand, regular individual optical fibers (not polarization maintaining ones) similar in design to the fibers that constitute our photonic crystal (Fig. 1) scramble the polarization of incoming light. Generally, NSOM fiber tips also do not preserve the polarization of the light,[12] so we can disregard this difference and consider the field to be scalar. In this case, the wave equation looks exactly like the Schrödinger equation for an electron in a periodic potential $U=\omega^2\epsilon_1/c^2$ and we can directly use the standard representation of the Schrödinger equation in momentum space[13]:

$$(k_\parallel^2+k_\perp^2-\epsilon_0\omega^2/c^2)A_{k_\perp}+\sum_G U_G A_{k_\perp-G}=0, \qquad (2)$$
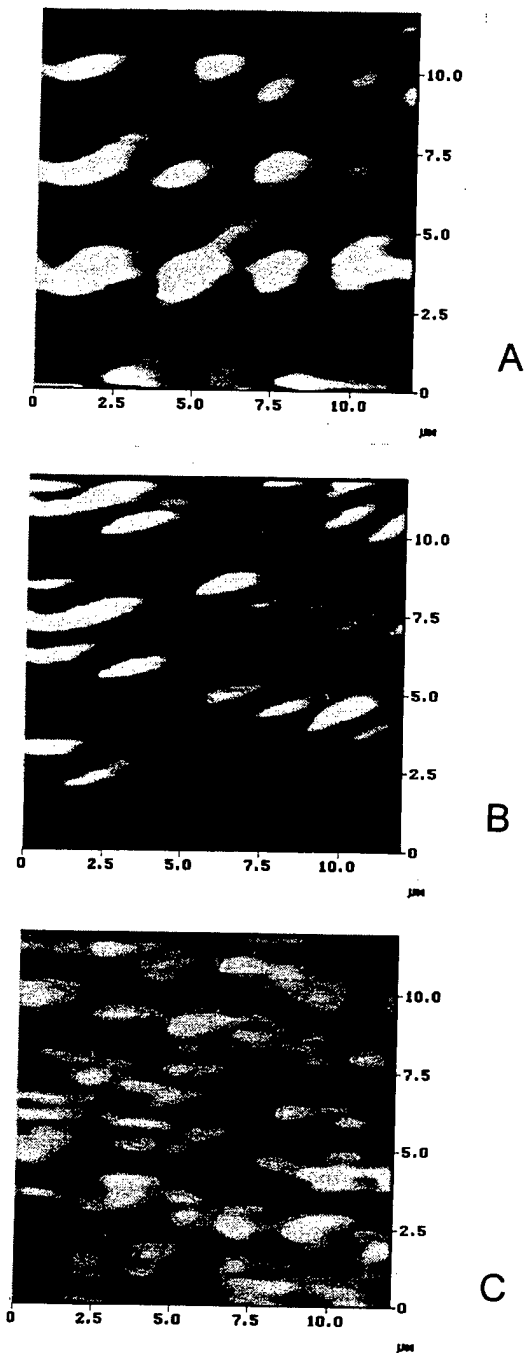
FIG. 4. Transmission near-field optical images of the photonic crystal taken at different angles of bottom face illumination: (a) 0°, (b) 7°, (c) 15°.

where $U(\mathbf{r}) = \Sigma_G U_G e^{iG \cdot \mathbf{r}}$ is the periodic potential, G are the reciprocal lattice vectors, and

$$E = e^{i\mathbf{k}_\perp \mathbf{r}} \sum_G A_{\mathbf{k}_\perp - G} e^{-iG \cdot \mathbf{r}} \qquad (3)$$

is the Bloch wave solution of the equation.

Usually it is reasonable to assume that the coefficients $A_\mathbf{k}$ are very small for large absolute values of $\mathbf{k}$. We also see this from our experimental measurements in Fig. 5. This reduces the Schrödinger equation (2) to a small number of linear equations relating $A_\mathbf{k}$ and U_G.
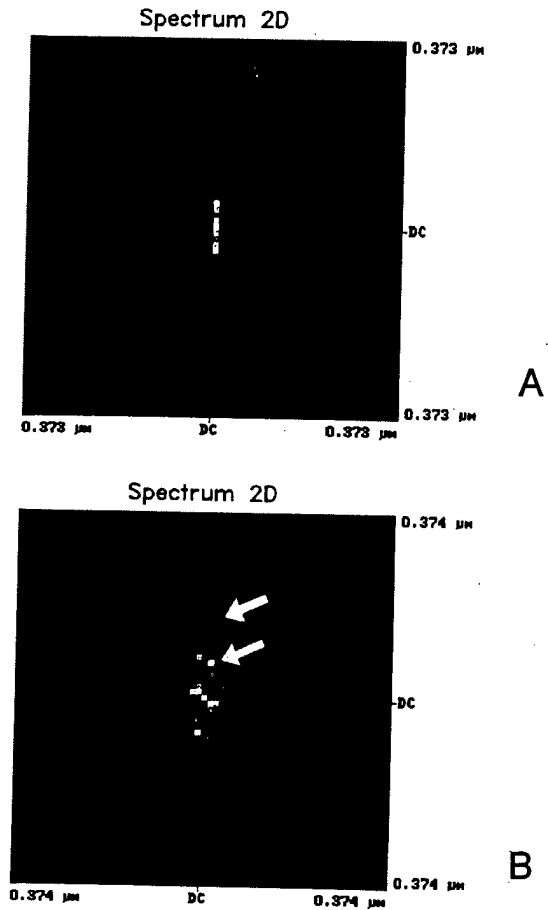

FIG. 5. Images (a) and (b) are the Fourier spectra of the images from Figs. 4(a) and 4(b), respectively. Additional periodicity and a richer spatial frequency spectrum appear at larger excitation angles. Spectral peaks near the first- and second-order reciprocal lattice vectors are shown by arrows in (b).

We have performed a one-dimensional reconstruction of the photonic crystal refractive index as follows. The physical value measured in the experiment is the local electromagnetic field intensity on the face of the photonic crystal. If a one-dimensional Bloch wave propagates in the crystal along the x direction, its field distribution can be written as $E = \Sigma_n A_n e^{i(kx - \omega t)} e^{i2\pi n x/a}$, where a is the period of the crystal in the direction of propagation and n is an integer. An averaged field intensity is equal to

$$I = 1/2 \sum_{mn} A_m A_n \cos[2\pi(n-m)x/a]. \qquad (4)$$

Thus measurements of the intensities of spectral peaks at $2\pi n/a$ in Fig. 5 allow us to recover the coefficients A_n of the Bloch wave. The first three coefficients have been measured. Substitution of these A_n in Eq. (2) allows us to obtain three coefficients U_n of the Fourier spectrum of the crystal potential in this direction: $U(x) = \Sigma_n U_n e^{i2\pi n x/a}$. The results of our measurements are represented in Fig. 6, which shows variations of the refractive index of the photonic crystal along one direction. The amplitude of these variations agrees well with the indices of the bulk unprocessed glasses used to make the crystal, which were measured by Schott Glass Technologies, Inc. at 590 nm to be 1.657 and 1.676. Thus the simple ap-
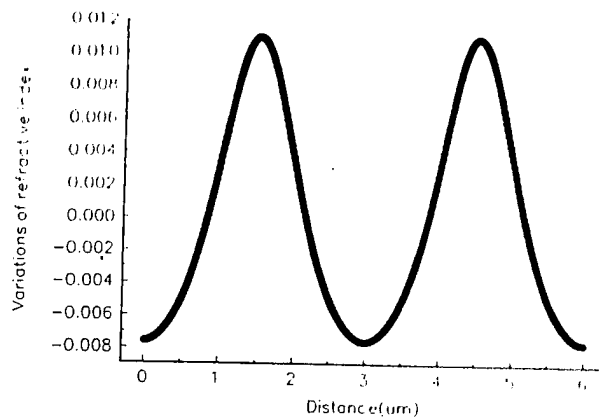
FIG. 6. Reconstructed refractive index variations in the photonic crystal along one direction.

proach introduced above allows a reasonable description of the photonic crystal properties.

PLASMONIC CRYSTAL STUDY

A surface plasmon can be excited on the surface of the rectangular bigrating (Fig. 2) at a number of resonant angles. These angles α_n are determined by the quasimomentum conservation law: $k \sin \alpha_n = k_p + 2\pi n/a$, where k_p is the SP wave vector on the flat metal surface, a is the period of the structure in the direction of propagation, and n is an integer. The angular dependence of the optical signal measured at the output of the fiber tip of our NSOM near one of the resonant angles is shown in Fig. 7. Resonant excitation of SP has been clearly detected. The angular width of the resonant curve is narrower than in Ref. 6. This may be attributed to the better surface quality of the bigrating used in our experiments.

We simultaneously measured topography of the sample and the optical field distribution with resonant SP excitation. Some examples of these images are shown in Figs. 8(a)–8(c). The periodicity properties of the optical images are much more complicated than those of a topographical image. This is evident from the Fourier image of Fig. 8(c) shown in Fig. 9. The brightest spectral peak in this image corresponds to a spatial period of 3.5 μm. Our calculations show this value to be approximately equal to half of the largest effec-

FIG. 8. Topography (a) and optical near-field distributions in the plasmon crystal measured on different scales (b), (c) with surface plasmon excitation.

tive wavelength of SP propagating along the surface of the plasmonic crystal: $\lambda_p^* = 2\pi/k_p^* = 2\pi/(k_p + 2\pi n/a) = 7.26$ μm at $n = -2$. This indicates that we observe interference pattern of the plasmon Bloch waves in the image in Fig. 8(c). Complicated interference patterns formed by SPs on the flat gold surface had been observed in Ref. 14. They were attributed to the presence of surface defects. The surface quality of our plasmonic crystal structure is very good (Fig. 2), nevertheless some surface defects can be seen. So the appearance of SP Bloch wave interference patterns in the images is natural.
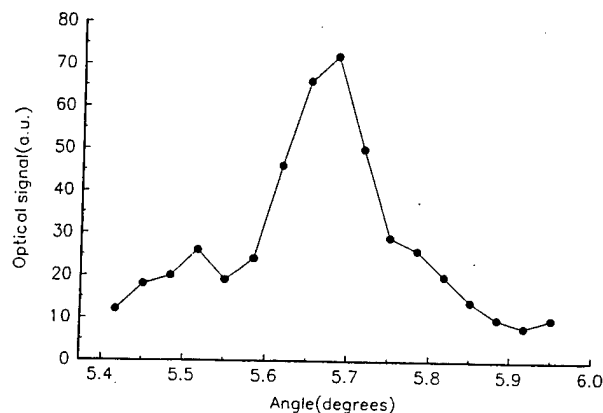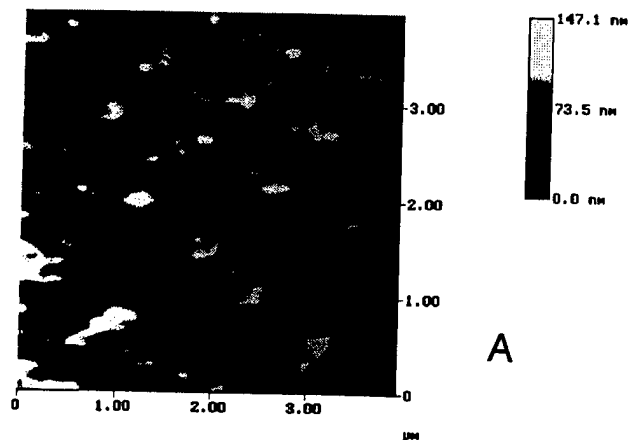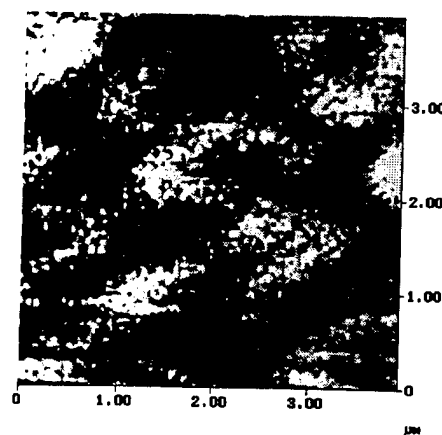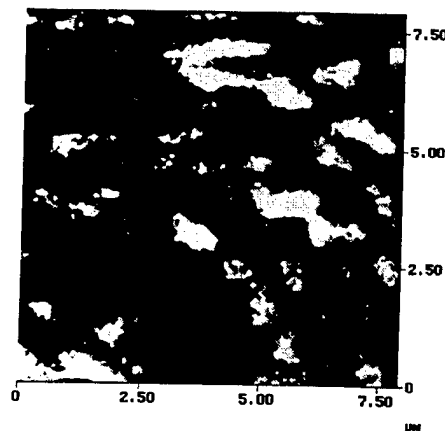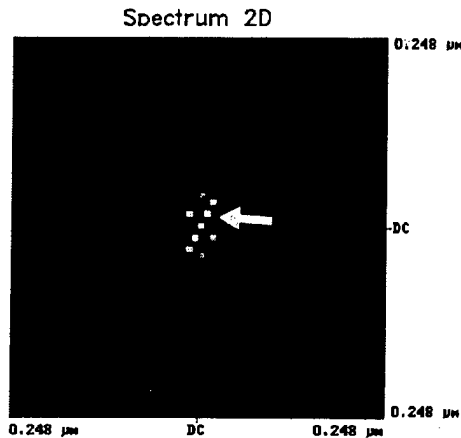

FIG. 7. Angular dependence of the NSOM optical signal near one of the SP resonances.

Spectrum 2D

FIG. 9. Fourier spectrum of the image in Fig. 8(b). The spectral peak at a spatial period of 3.5 μm is shown by an arrow.

NSOM allows us to modify a surface under investigation. Direct-write lithography may be performed by coupling UV light into a fiber tip[9] or by delicate mechanical touching of the sample surface.[15] Mechanical surface modification is especially easy in the case of a soft sample such as a gold surface. We have verified experimentally that artificially created defects lead to the appearance of very pronounced long-period interference patterns in the vicinity of defects. The results of such an experiment are shown in Fig. 10. A defect has been created in the middle of the NSOM field of view on top of the periodic plasmon crystal structure, which has also been slightly modified. A shadowlike phenomenon is seen just behind the defect (the direction of SP propagation is shown by an arrow). A set of stripes with a period on the order of 3 μm has become very pronounced. These results indicate that we are indeed dealing with the interference of SP Bloch waves.

The SP field distribution and band-gap structure of a plasmonic crystal can be calculated analytically in the limit of small roughness if the surface topography is known.[16] In our case the surface roughness cannot be considered to be small since the depth of the grooves in Fig. 2 is comparable with the thickness of the gold film. Rather complicated numerical calculations are required to compare the results of our measurements with an exact theory also presented in Ref. 16. Such a comparison is desirable and could give a good test of the electrodynamics of metals on a submicrometer scale.

A simpler approach is to use the concept of effective plasmon refractive index introduced in Ref. 10. SP phase velocity depends on the metal film thickness. The effective refractive index of a surface defect may be introduced as a ratio of SP phase velocities on the defect and on the background metal film area. Use of this concept makes the description of photonic and plasmonic crystals similar. Effective SP refractive index distribution over the crystal surface may be derived using the procedure described above for the case of a photonic crystal. Unfortunately, SP Bloch wave interference makes the situation more complicated since they contribute substantially to the Fourier spectrum of the SP field distribu-
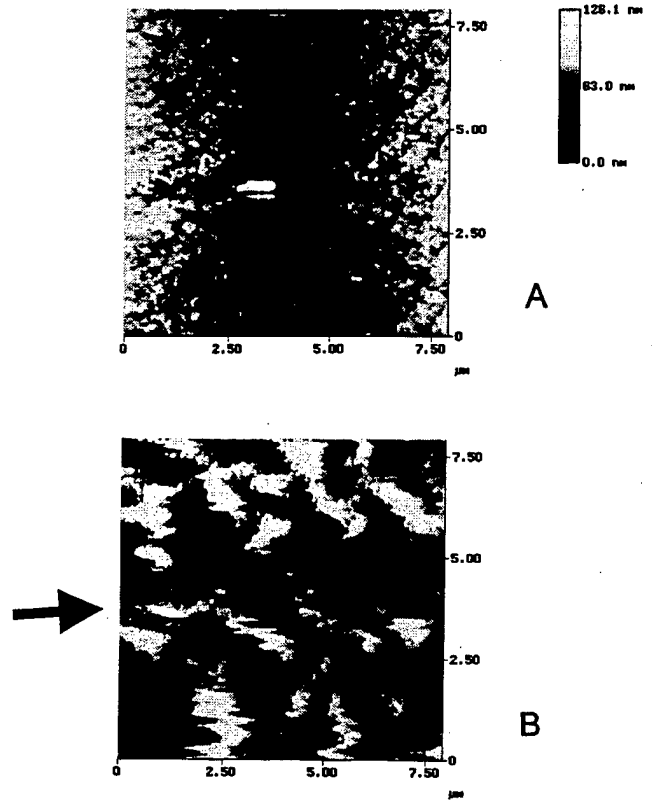

FIG. 10. Topography (a) and optical near-field distribution (b) around artificially created defect on the surface of the plasmon crystal structure. The direction of SP propagation is shown by an arrow.

tion and the amplitude of the reflected waves is generally unknown. Only an order of magnitude estimate of the effective refractive index can be derived from Fig. 9. It follows from Eq. (2) that $\omega^2 \epsilon_1 / c^2 \sim (2\pi/a)^2 A_{n+1} / A_n$. This leads to $\Delta n \sim (\lambda/a)^2 A_{n+1} / A_n \sim 0.05$ as an estimate of the amplitude of the effective SP refractive index variations. This number is in general agreement with the values of SP refractive indices of different surface defects derived in Ref. 10.

CONCLUSION

The main results of this paper may be summarized as follows.

An alternative method for studying photonic crystals using NSOM has been introduced. In a previous study [5] the photonic crystals were excited by light from a NSOM tip. This may be idealized as an excitation with a δ function in coordinate space. The transmitted light distribution was analyzed as a function of the absolute value of its momentum.

In the present work photonic crystals were excited with an incident laser beam. This may be idealized as an excitation by a δ function in momentum space. NSOM images are Fourier analyzed in order to extract information on refractive index distributions in the photonic crystals.

Interference patterns produced by SP Bloch waves in the plasmonic crystal have been directly observed.

[1] J. D. Joannopoulos, R. D. Meade, and J. N. Winn, *Photonic Crystals* (Princeton University Press, Princeton, NJ, 1995).

[2] E. Yablonovitch, Phys. Rev. Lett. **58**, 2059 (1987); W. M. Robertson, G. Arjavalingam, R. D. Meade, K. D. Brommer, A. M. Rappe, and J. D. Joannopoulos, *ibid.* **68**, 2023 (1992).

[3] K. Inoue, M. Wada, K. Sakoda, M. Hayashi, T. Fukushima, and A. Yamanaka, Phys. Rev. B **53**, 1010 (1996); A. Rosenberg, R. J. Tonucci, H. B. Lin, and A. J. Campillo, Opt. Lett. **21**, 830 (1996); H. B. Lin, R. J. Tonucci, and A. J. Campillo, Appl. Phys. Lett. **68**, 2927 (1996).

[4] *Near Field Optics*, edited by D. W. Pohl and D. Courjon (Kluwer, Dordrecht, 1993).

[5] E. B. McDaniel, J. W. P. Hsu, L. S. Goldner, R. J. Tonucci, E. L. Shirley, and G. W. Bryant, Phys. Rev. B **55**, 10 878 (1997).

[6] R. A. Watts, J. B. Harris, A. P. Hibbins, T. W. Preist, and J. R. Sambles, J. Mod. Opt. **43**, 1351 (1996).

[7] H. Raether, *Surface Plasmons*, Springer Tracts in Modern Physics Vol. 111 (Springer, Berlin, 1988).

[8] P. Dawson, F. de Fornel, and J.-P. Goudonnet, Phys. Rev. Lett. **72**, 2927 (1994).

[9] I. I. Smolyaninov, D. L. Mazzoni, and C. C. Davis, Phys. Rev. Lett. **77**, 3877 (1996).

[10] I. I. Smolyaninov, D. L. Mazzoni, J. Mait, and C. C. Davis, Phys. Rev. B **56**, 1601 (1997).

[11] A. A. Maradudin and A. R. McGurn, in *Photonic Band Gaps and Localization*, edited by C. M. Soukoulis (Plenum, New York, 1993), p. 247.

[12] J. K. Trautman, E. Betzig, J. S. Weiner, D. J. DiGiovanni, T. D. Harris, F. Hellman, and E. M. Gyorgy, J. Appl. Phys. **71**, 4659 (1992).

[13] C. Kittel, *Introduction to Solid State Physics* (Wiley, New York, 1976).

[14] S. I. Bozhevolnyi, I. I. Smolyaninov, and A. V. Zayats, Phys. Rev. B **51**, 17 916 (1995).

[15] S. I. Bozhevolnyi and F. A. Pudonin, Phys. Rev. Lett. **78**, 2823 (1997).

[16] A. A. Maradudin, in *Surface Polaritons*, edited by V. M. Agranovich and D. L. Mills (North-Holland, Amsterdam, 1982), p. 405.

Near-field second harmonic imaging of lead zirconate titanate piezoceramic

Igor I. Smolyaninov, Chi H. Lee, and Christopher C. Davis

Electrical Engineering Department, Laboratory for Atomic, Molecular, and Optical Science and Engineering, University of Maryland, College Park, Maryland 20742

A technique to characterize the local nonlinearity of lead zirconate titanate piezoceramic (PZT) has been developed. Near-field optical microscopy has been used to image variations in local optical second harmonic generation from the PZT surface. Individual crystalline grains and grain boundaries are the main features visible in the images. The technique allows us to determine the local poling direction of individual submicrometer size crystalline grains of ceramic by near-field second harmonic imaging at different angles of incidence and polarization states of fundamental excitation light. © *1999 American Institute of Physics.* [S0003-6951(99)00514-8]

The ability of ferroelectric materials such as $Pb(Zr_xTi_{1-x})O_3$ (PZT) piezoceramics to switch from one stable polarization state to another forms the basis of a new thin film technology for data storage.[1] Thin PZT films are used in prototype nonvolatile ferroelectric random-access memory (NVFRAM) and dynamic random-access memory (DRAM) devices. PZT materials also have numerous applications in actuators, transducers, resonators, and sensors. Crucial parameters of piezoceramic performance in different applications are hysteresis, nonlinearity, polarization retention (or the loss of polarization), creep, etc. For proper application of the material, it is imperative to understand this nonlinear behavior on a microscopic level. Optical microscopy of second harmonic generation (SHG) in PZT is a natural tool to study this local nonlinearity.

Far field observations of SHG in PZT ceramic near the ferroelectric phase transition[2] demonstrated a sharp drop in SHG in the paraelectric state. The second harmonic intensity versus temperature curve corresponds qualitatively to the temperature dependence of the spontaneous polarization, which is an order parameter in the transition to the polar phase. PZT ceramic is a strongly scattering medium consisting of individual submicrometer-size crystallites. The elastic scattering lengths of fundamental and SH light in PZT is of the order of the characteristic size of a crystallite. Theory of SHG in strongly scattering media shows[3] that generation of SH light in PZT should occur in a thin layer (of the order of an elastic scattering length) near the illuminated interface. Thus, near-field second harmonic microscopy[4] is ideally suited for studies of PZT nonlinearity and poling quality at the microscopic level (the level of individual crystallites and crystallite boundaries). Its main advantages in comparison with the other scanning probe techniques such as recently developed piezoresponse atomic force microscopy[5] are the possibility of fast time-resolved measurements, and substantially smaller perturbation of the sample under investigation caused by the optical probe.

We report second harmonic imaging of the surface of PZT ceramic obtained in a near-field microscopy setup (Fig. 1) using a Ti:sapphire laser system consisting of an oscillator and a regenerative amplifier operating at 810 nm (repetition rate up to 250 kHz, 100 fs pulse duration, and up to 10 μJ

pulse energy). The SHG from the surface of a PZT sample was excited at an angle of incidence around 60° by a weakly focused beam (illuminated spot diameter on the order of 50–100 μm) of the Ti:sapphire laser. The excitation power at the sample surface was kept well below the ablation threshold. The local SHG was collected using an uncoated adiabatically tapered fiber tip, which is drawn at the end of a single mode fiber by the standard heating and pulling procedure. The fiber tip was scanned over the sample surface with a constant tip-surface distance of a few nanometers using shear force feedback control described elsewhere.[4] Therefore, surface topography images were obtained with a resolution on a nanometer scale, while simultaneously recording the SH near-field image. The SH signal was measured with a photomultiplier and gated electronics. The SH signal at every point of the image was averaged over 30–100 ms. The characteristic SH photon counting rate was on the order of one photon count per 30 laser pulses. Thus, the image acquisition time was on the order of 20–30 min. This is approximately an order of magnitude improvement with respect to our previously reported work[4] where a Nd:yttrium–aluminum–garnet (YAG) laser was used as a source of fundamental light.
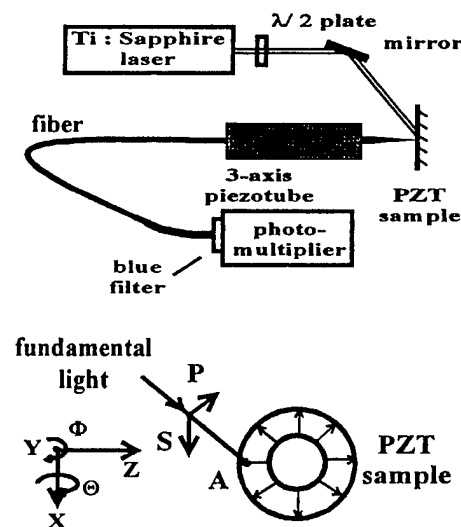

FIG. 1. Schematic view of the near-field optical microscope for second harmonic generation studies.
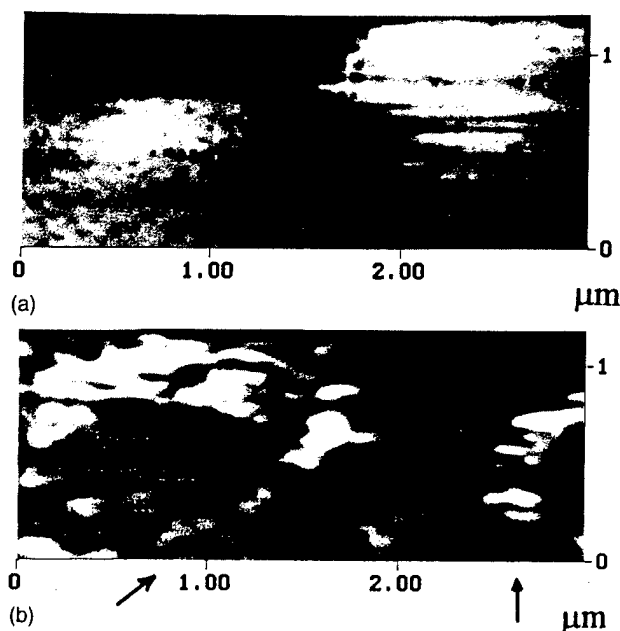
FIG. 2. Simultaneously measured (a) shear-force topographical and (b) SH near-field optical images of a PZT sample surface. The size of the images is 1.2 μm by 3 μm. Height variation within the topographical image is 580 nm. The near-field image has been measured using P-polarized excitation light. Crystallite boundaries are indicated by arrows.

We have used a commercial radially poled PZT tube as a sample. Measurements have been performed at a point A (see Fig. 1) where the electric field of P-polarized fundamental light has a component along the macroscopic poling direc-

tion of the piezotube. Electric field of S-polarized light is perpendicular to the poling direction. Simultaneously measured topographical and near-field SH images of the surface of the PZT sample obtained using P-polarized fundamental light are shown in Fig. 2. The polycrystalline structure of the ceramic exhibits itself in these images. Different crystallites show different brightness of SH emission that corresponds to variations in local poling. These variations should contribute to the effects of hysteresis and creep of piezoceramic. Some crystallite boundaries also show up in the SH image (as is indicated by arrows). They are believed to contribute to the nonlinear behavior of PZT ceramic.[6]

Symmetry considerations show that the second harmonic polarization tensor $d_{ijk}^{2\omega}$ that relates SH and the fundamental excitation light ($P_i^{2\omega} = \epsilon_0 d_{ijk}^{2\omega} E_j^\omega E_k^\omega$) has the same form as the piezoelectric tensor d_{ijk}, which gives the electric polarization P_i at a given stress σ_{jk}: $P_i = d_{ijk}\sigma_{jk}$.[7] Thus, it should be possible to study local variations of the piezoelectric tensor of the PZT ceramic d_{ijk} by looking at the local SH response of the material for different polarization states of incoming fundamental light. Indeed, switching between P- and S-polarized excitation light leads to substantial changes in the near-field SH images of PZT ceramic, as it is evident from Fig. 3. Differences in polarization directions of individual crystallites exhibit themselves as variations of SH brightness for different polarizations of excitation light. A complete recovery of the local poling direction should be possible if near-field SH measurements are made at different polarization states and different angles of incidence of the
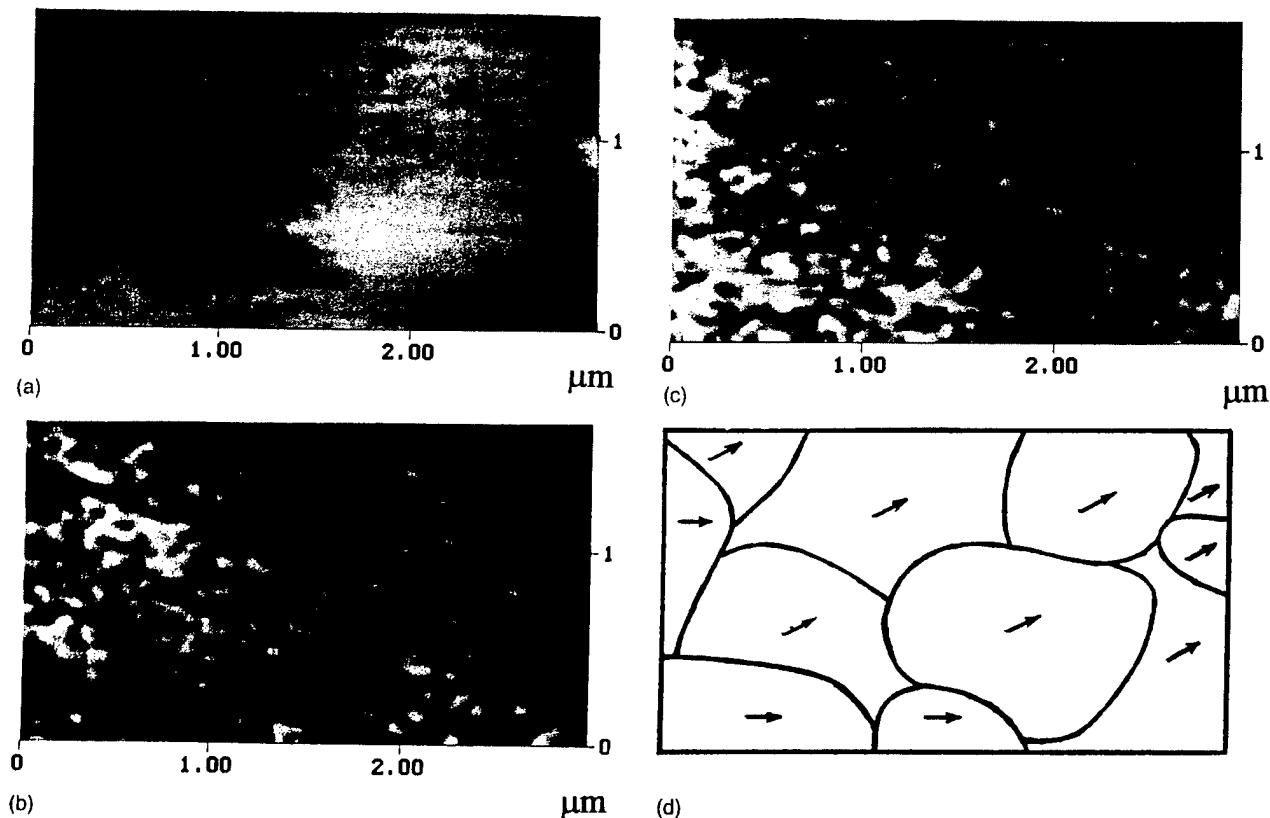
FIG. 3. Simultaneously measured (a) shear-force topographical and SH near-field optical images of a PZT sample surface measured using (b) P- and (c) S-polarized excitation light. Size of the images is 1.7 μm×3 μm. Height variation within the topographical image is 350 nm. Image (d) represents a schematic view of different grains visible in the images (a)–(c) with the in-plane components of the local poling vector shown by the arrows.

fundamental light together with the control of SH light polarization.

Individual crystallites of PZT have a perovskite crystal structure and belong to the tetragonal symmetry class $4mm - C_{4v}$. BaTiO$_3$ is a very similar piezoelectric material with the measured nonlinear susceptibilities[8] of $d^{2\omega}_{yyz} = d^{2\omega}_{xxz} = d^{2\omega}_{yzy} = d^{2\omega}_{xzx} = -17.7 \times 10^{-12}$ m/V, $d^{2\omega}_{zyy} = d^{2\omega}_{zxx} = -18.8 \times 10^{-12}$ m/V, and $d^{2\omega}_{zzz} = -7.1 \times 10^{-12}$ m/V, where z is the poling direction. A three times smaller value of $d^{2\omega}_{zzz}$ with respect to the other components of the SHG tensor results from the much smaller value of the permittivity ϵ_{zz} of a piezoelectric single domain crystal in the poling direction. Thus, local SH intensity should have a pronounced minimum (equal to approximately one tenth of its average value) when the electric field of fundamental excitation light is polarized along the local z direction. This is one of the recipes for local poling direction recovery, although it may not be the most convenient way since it requires angle of incidence adjustment of the fundamental excitation light.

It is much easier to analyze data in Fig. 3 if an assumption is made that the local poling direction deviates slightly from the macroscopic one (this assumption should be true in the case of a poled PZT sample). If the local poling direction is rotated by a small angle θ around the X axis (see Fig. 1) the electric field of the S-polarized fundamental excitation light remains perpendicular to the poling direction. No changes in local SHG should be expected. On the other hand, if the local poling direction is rotated by a small angle Φ around the Y axis, the components of second harmonic polarization change as follows:

$$P^{(2)}_z = \epsilon_0 d^{2\omega}_{zxx} E^2 \cos^2 \Phi$$

and

$$P^{(2)}_x = \epsilon_0 d^{2\omega}_{xxz} E^2 \sin^2 \Phi \ll P^{(2)}_z, \tag{1}$$

where E is the fundamental electric field. Thus, the SH image in Fig. 3(c) reflects variations in $\cos^4 \Phi$. Analysis of Fig. 3(b) is more complicated since variations in Θ and Φ are mixed in the case of P-polarized excitation. However, expressions similar to Eq. (1) are easy to derive and possible to analyze completely if the data for $\cos^4 \Phi$ is known. This analysis is especially easy when there is no variation in local S-polarized SHG as in the upper right part of Fig. 3(c). In this case variations of local SHG with P-polarized excitation correspond to variations in Θ. Figure 3(d) represents a schematic view of different grains visible in the images in Figs. 3(a)–3(c) with the in-plane components of the local poling vector shown by the arrows. The directions of local poling vectors were derived using the procedure described above.

In conclusion, we have developed a microscopy technique to study local nonlinear properties of PZT piezoceramic. The technique allows us to determine the local poling direction of individual submicrometer size crystalline grains of ceramic by near-field second harmonic imaging for different angles of incidence and polarization states of fundamental excitation light.

[1] O. Auciello, J. F. Scott, and R. Ramesh, Phys. Today, 22 (1998).

[2] O. A. Aktsipetrov, S. B. Apukhtine, A. A. Nikulin, K. A. Vorotilov, E. D. Mishina, and A. S. Sigov, JETP Lett. **54**, 563 (1991).

[3] V. E. Kravtsov, V. M. Agranovich, and K. I. Grigorishin, Phys. Rev. B **44**, 4931 (1991).

[4] I. I. Smolyaninov, A. V. Zayats, and C. C. Davis, Opt. Lett. **22**, 1592 (1997).

[5] A. Gruverman, H. Tokumoto, A. S. Prakash, S. Aggarwal, B. Yang, M. Wuttig, R. Ramesh, O. Auciello, and T. Venkatesan, Appl. Phys. Lett. **71**, 3492 (1997).

[6] V. Mueller and Q. M. Zhang, Appl. Phys. Lett. **72**, 2692 (1998).

[7] P. N. Butcher, *Nonlinear Optical Phenomena* (Ohio State University Press, Columbus, 1965), pp. 43–50.

[8] F. Zernike and J. E. Midwinter, *Applied Nonlinear Optics* (Wiley, New York, 1973).

Giant Enhancement of Surface Second Harmonic Generation in BaTiO$_3$ due to Photorefractive Surface Wave Excitation

Igor I. Smolyaninov, Chi H. Lee, and Christopher C. Davis

Electrical Engineering Department, University of Maryland, College Park, Maryland 20742
(Received 29 March 1999)

We report observation of strongly enhanced surface second harmonic generation (SHG) in BaTiO$_3$ due to excitation of a photorefractive surface electromagnetic wave. Surface SH intensity may reach 10^{-2} of the incident fundamental light intensity. Angular, crystal orientation, and polarization dependencies of this SHG are presented. Possible applications of this effect in nonlinear surface spectroscopy are discussed.

Linear surface electromagnetic waves (SEW) such as surface plasmons or surface polaritons [1] play a very important role in such surface optical phenomena as surface enhanced Raman scattering, surface second harmonic generation (SHG), etc. They are extremely useful in applications such as chemical and biological sensing since the electromagnetic field of a SEW is strongly enhanced near the interface. A linear SEW may be excited at the interface between media with opposite signs for their dielectric constants ϵ, such as at a metal-vacuum interface. Another example is the interface between a vacuum and a dielectric that has a sharp absorption line. Such a dielectric has $\epsilon(\omega) < 0$ for frequencies just above the absorption line. In both cases the SEW free propagation length in the visible range does not exceed a few micrometers because of high losses [1]. This limits the potential advantages of using SEW in surface enhanced nonlinear optical studies and sensor applications.

Recently, a new kind of nonlinear SEW called a photorefractive surface wave has been predicted [2] and observed experimentally [3] in BaTiO$_3$. This phenomenon is closely related to self-trapped optical beams (also known as spatial solitons) and self-bending beams observed in photorefractive crystals [4]. A photorefractive SEW occurs when a beam self-bent towards the positive direction of the optical axis (the poling direction) undergoes a cycle of deflections towards the face of the crystal and total internal reflections. The resulting nonlinear SEW is localized near the crystal-air interface with a penetration depth as small as 10 μm into the photorefractive crystal [2]. This leads to a strong enhancement of the optical field near the interface that is common for all SEWs. On the other hand, since BaTiO$_3$ is transparent in the visible range, the free propagation length of the photorefractive SEW along the surface is limited only by the size of the crystal. As a result, a very strong enhancement of all nonlinear surface optical phenomena (such as surface adsorbed molecular luminescence, Raman scattering, surface SHG, etc.) may be expected due to photorefractive SEW excitation. This effect may also be used in combination with further field enhancements produced by surface topo-graphical defects or by the probe tip of a scanning probe microscope [5].

In this Letter we report the first observation of strongly enhanced surface SHG due to the photorefractive SEW excitation in BaTiO$_3$. Surface SHG in BaTiO$_3$ is a very suitable phenomenon for demonstrating the potential of photorefractive SEWs in nonlinear surface optics. Phase-matched optical SHG (collinear or noncollinear) is forbidden in the bulk of BaTiO$_3$ in the visible range because of strong dispersion: The refractive indices for ordinary and extraordinary waves are 2.67 and 2.57, respectively, at 400 nm, and 2.36 and 2.32, respectively, at 800 nm light wavelength [6]. The momentum conservation law cannot be satisfied in the volume SHG process. Thus, in contrast to experiments done with KTP crystals [7], observation of the fundamental and phase-matched SHG fields mutually trapped in the volume spatial solitary wave is impossible in BaTiO$_3$. On the other hand, phase-matching conditions are modified for the surface SHG. Only the momentum component parallel to the interface must be conserved. This leads to an extremely strong phase-matched surface SHG when a photorefractive SEW is excited.

The surface nature of this SHG, in combination with the strong photorefractivity of BaTiO$_3$, leads to quite peculiar angular and orientational behavior of the SH light intensity. We believe that our observations performed in a well controlled geometry may clarify a lot of questions concerning still unclear "anomalous" SHG in BaTiO$_3$ reported recently by a number of groups [8,9]. This is especially important for the rapidly developing field of ferroelectric oxide film growth and characterization. Much recent effort in this field is caused by the applications of these films in nonvolatile ferroelectric random-access memory and dynamic random-access memory devices [10]. SHG has been used to determine the crystallographic orientation and the degree of poling of these films (in particular, BaTiO$_3$ films in [9]).

Our experimental geometry is shown in Fig. 1. The iron doped crystal of BaTiO$_3$ from Sanders Inc. used in the experiments is a 8 mm $\times$ 8 mm $\times$ 8 mm cube which

was cut with two opposing faces perpendicular to the c axis and poled along the c axis. The crystal was mounted on a three-axis translational and rotational stage. Linearly polarized light from a Ti:sapphire laser operating at a wavelength of 810 nm (repetition rate 76 MHz, 100 fs pulse duration, 30 mW average power) was focused onto the top edge of the crystal. The direction of the beam was parallel to the top face of the crystal.

As the vertical position of the crystal was scanned, very bright second harmonic light emission coming from the top face of the crystal was observed. The brightness of SH emission was very sensitive to the vertical position of the crystal as is evident from Fig. 2(a), which was obtained using a focusing lens with a focal length of 60 mm. No SH emission had been detected when the fundamental light passed through the crystal in any direction far from the top face. This is consistent with the fact that phase-matched SHG is prohibited in the bulk of $BaTiO_3$ crystal. Also, no comparable SHG has been detected from the other five faces of the same crystal. The full width at half maximum of the SH peak in Fig. 2(a) is equal to 80 μm.

The SH emission appeared to be localized in the xy plane of the top face of the crystal coming out of the top face within a wide (almost 180°) angle. This peculiar spatial distribution of SHG is illustrated in Fig. 3 which shows a pattern of SH illumination on the screen placed just behind the crystal in the xz plane. The SH light is vertically polarized. Its intensity is proportional to the square of the fundamental light intensity and depends strongly on the polarization state of the linearly polarized fundamental light [Fig. 2(b)]. The SH intensity is approximately 6 times stronger in the case of fundamental light linearly polarized perpendicular to the optical axis of the $BaTiO_3$ crystal.

All features of the observed SH emission are consistent with the proposed surface SHG enhancement due to the photorefractive surface wave excitation in $BaTiO_3$. The crystal cut allows photorefractive SEW propagation only on the top face of the crystal (only near this face can photorefractive self-bending and total internal reflection compete with each other). This is consistent with the observation of SHG only from the top face of the crystal. At the same time, the full width at half maximum of the vertical position dependence of SHG in Fig. 2(a) corresponds to the observed range of photorefractive SEW launching in $BaTiO_3$ [3].
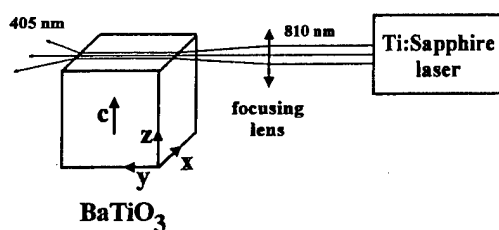
An explanation of the angular distribution of the observed SHG needs a more detailed analysis. Nonlinear SEW solutions of the Maxwell equations in a photorefractive medium may be found as follows [2]. It is assumed that a SEW written as $E(z, y) = E(z) \exp(-iky)$ induces a dielectric constant change of the form $\epsilon(z) = \epsilon + \delta\epsilon(z)$ due to the photorefractive effect [here $E(z)$ is supposed to be real, ϵ is the real dielectric constant of the medium in the absence of the wave, the photorefractive medium is supposed to be optically isotropic, and the field distribution is assumed to be independent of x. These simplifying assumptions may not be true in the most general case, but they allow us to illustrate the basic physics of the phenomenon]. Substituting this into Maxwell's equations results in the following equation for $E(z)$:

$$[d^2/dz^2 + (k_0^2 - k^2) + k_0^2 \delta\epsilon(z)/\epsilon]E(z) = 0, \quad (1)$$

where $k_0 = \omega(\epsilon\epsilon_0\mu_0)^{1/2}$ is the wave number of the light in a linear medium with the same unperturbed dielectric constant ϵ. Assuming the diffusion mechanism for nonlinearity [11], the distribution $\delta\epsilon(z)$ may be related
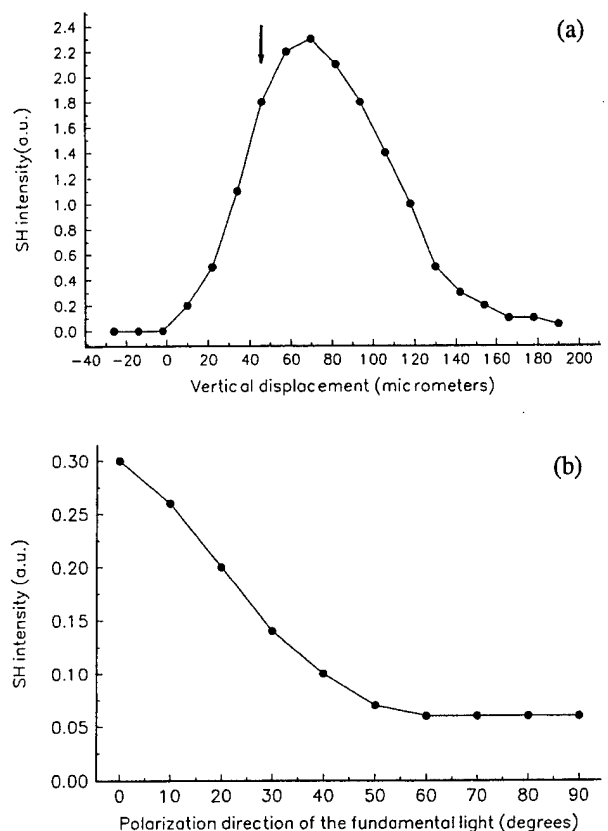
FIG. 2. (a) SH intensity as a function of the vertical position z of the crystal. Large positive z corresponds to the fundamental light passing through the crystal. Approximate position of the focal spot of the lens is shown by the arrow. (b) SH intensity as a function of the polarization direction of the linearly polarized fundamental light, 90° corresponds to the polarization direction parallel to the optical axis of the $BaTiO_3$ crystal (z direction).

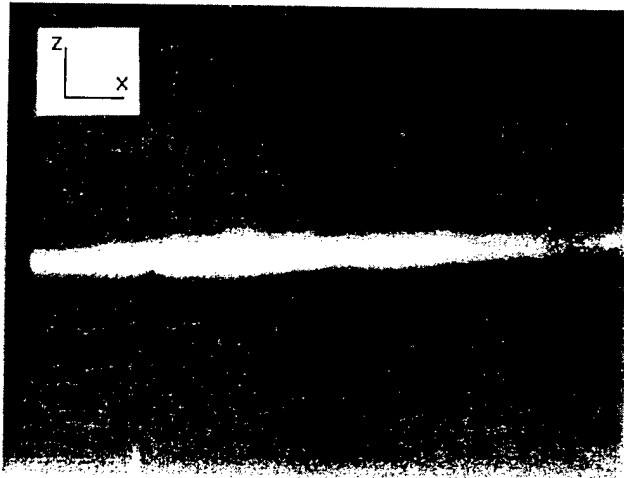FIG. 1. Schematic view of our experimental geometry.

FIG. 3. The pattern of SH illumination produced on a screen placed just behind the crystal. A bandpass filter is used to cut off the illumination by fundamental light.

to $E(z)$ through the space-charge electric field E_{sc}:

$$E_{sc} = -(k_B T/e)[dI(z)/dz]/I(z), \qquad (2)$$

where $I(z)$ is the intensity of light. The space-charge electric field induces refractive index changes via the electro-optic effect [11]:

$$\delta\epsilon(z) = 2n^4 r(k_B T/e)[dE(z)/dz]/E(z), \qquad (3)$$

where r is the linear electro-optic coefficient. Thus, we obtain the wave equation in the form

$$[(d^2/dz^2)/k_0^2 + (2\gamma d/dz)/k_0 -$$
$$2(k - k_0)/k_0]E(z) = 0, \qquad (4)$$

where $\gamma = k_0 n^2 r(k_B T/e)$. This equation has a solution exponentially decaying into the photorefractive medium:

$$E(z) = \exp(-\gamma k_0 z)\cos\{[2(k - k_0)k_0]^{1/2}z + \phi\}. \qquad (5)$$

In the case of BaTiO$_3$ the photorefractive SEW field penetration depth is $d_z = (\gamma k_0)^{-1} \sim 10 \ \mu m$ [2]. Since the resulting equation (4) is linear, this penetration depth does not depend on the field intensity.

Real laser beams have finite width in x, but if the width of the beam is much larger than d_z the simplified theory described above should be applicable. Thus, a real life photorefractive SEW must have a localization length in the x direction (d_x) much larger than d_z. Indeed, this is evident from the profile of the photorefractive SEW in BaTiO$_3$ measured in [3], where $d_x \sim 500 \ \mu m$. Unlike d_z, d_x may depend on the intensity of SEW.

A very fruitful approach to all phenomena related to spatial solitons is the representation of solitons as linear waves propagating in the self-induced optical waveguides [12,13]. Let us follow this way of thinking and consider fundamental light propagating in a surface waveguide with a rectangular $d_z \times d_x$ profile such as $d_x \gg d_z \sim 10 \ \mu m$ [Fig. 4(a)] (this is an approximation since such a self-induced waveguide does not have sharp physical boundaries, but this approximation works fine for spatial
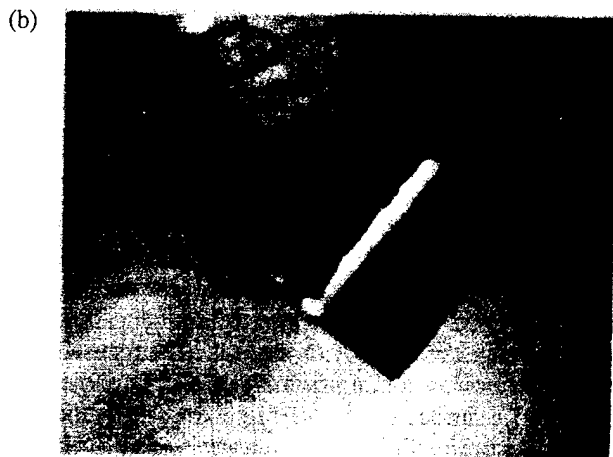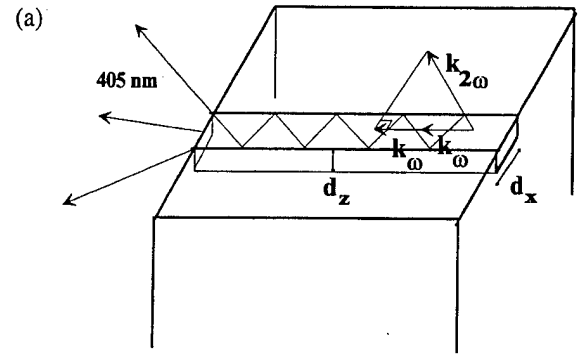
FIG. 4. (a) Phase-matched SHG in the self-induced surface waveguide. (b) A picture of the top face of the crystal taken through the bandpass filter which cuts off the fundamental illumination light. Simultaneous weak illumination with the white light from the flashlight allows the edges of the BaTiO$_3$ crystal to show. The focused fundamental beam was coming from the top right corner of the image. The surface beam of SH light trapped by the propagating photorefractive SEW is clearly visible.

solitons). The phase matching conditions for SHG in the surface waveguide are further modified. Only the momentum component parallel to the waveguide direction must be conserved. At the same time, such a waveguide is highly multimode with many optical modes corresponding to geometrical optics rays propagating in a zigzag manner parallel to the surface. Thus, there will always be a SH waveguide mode phase matched with the fundamental light. Upon resonant excitation, such a mode will be coupled to many other modes existing in the waveguide at the same frequency. As a result, when the SH light reaches the edge of the crystal, it leaves the surface waveguide in a ray fan parallel to the face of the crystal. This results in the pattern of SH illumination detected in Fig. 3.

We have performed further experiments to confirm the physical picture of the phenomenon described above. Using a 3.6-mm focal length 40× microscope objective as a focusing lens in Fig. 1, we have observed much brighter surface SH emission with an average power on the order

of some tens of microwatts. No damage to the surface of the BaTiO$_3$ crystal was apparent after this experiment. Thus, as much as 10^{-2} of the fundamental light power had been converted into SH emission. This is a much higher conversion efficiency than is usually observed in surface SHG experiments: simple calculations show that as much as 10^7 second harmonic photons per 1 nJ laser pulse have been generated. This is 3 orders of magnitude higher than the conversion efficiency observed in the case of surface SHG enhanced by a surface plasma wave [14]. It is comparable (just an order of magnitude smaller) with the best SH conversion efficiencies obtained in any other experimental geometry. At such a high power self-pumped phase conjugation builds up with the laser power dependent time constant on the order of a few hundreds of milliseconds, causing instability of the Ti:sapphire laser. So, optical isolation is necessary for SHG to be stable (which itself exhibits a similar characteristic buildup time following sudden changes in optical alignment).

A picture of the top face of the crystal taken through the bandpass filter (which cuts off the fundamental excitation light) is shown in Fig. 4(b). Simultaneous weak illumination with the white light from a flashlight allows us to show the edges of the BaTiO$_3$ crystal. The focused fundamental beam was coming from the top right corner of the image. The surface beam of SH light trapped by the propagating photorefractive SEW is clearly visible. The beam starts from the focal point of the microscope objective. It is possible to see the SHG because of surface scattering. The width of the self-induced surface waveguide is estimated to be on the order of 400 μm.

The polarization properties of SH emission mostly reflect the properties of the second harmonic polarization tensor $d_{ijk}^{(2)}$ of BaTiO$_3$, which relates SH and the fundamental excitation light ($P_i^{(2)} = \epsilon_0 d_{ijk}^{(2)} E_j^{(1)} E_k^{(1)}$). For a surface SH process in the geometry of our experiment only two nonzero components of $d_{ijk}^{(2)}$ are available: $d_{zxx}^{(2)} = -18.8 \times 10^{-12}$ m/V and $d_{zzz}^{(2)} = -7.1 \times 10^{-12}$ m/V [15]. Thus, the ratio of SH intensity for excitation with fundamental light linearly polarized in the x (horizontal) and z (vertical) directions should be $(d_{zxx}^{(2)}/d_{zzz}^{(2)})^2 = 7.0$ which is very close to the ratio observed in the experiment [Fig. 2(b)].

At the same time, the photorefractive coupling constant r is smaller in the case of horizontally (ordinary) polarized light. This means that the photorefractive SEW field penetration depth d_z is bigger in this case and the fundamental excitation light spends more time away from the surface. According to the simple self-induced waveguide model described above, we should expect stronger attenuation of SHG under these circumstances. In order to account for this discrepancy a complimentary point of view on the nature of SHG enhancement due to the photorefractive SEW excitation may be suggested. In the picture of a SEW as a beam undergoing a cycle of photorefractive deflections towards the face of the crystal and total internal reflections,

a periodic self-induced modulation of the refractive index near the surface of BaTiO$_3$ crystal may be expected. Such a situation would closely resemble the geometry of SHG experiments with periodically poled nonlinear crystals such as lithium niobate, which show substantial enhancement of SHG efficiency (periodic poling creates periodic modulation of refractive index near the interface).

In conclusion, we have observed strongly enhanced surface SHG in BaTiO$_3$ due to the excitation of a photorefractive surface electromagnetic wave. The surface SH intensity may reach 10^{-2} of the incident fundamental light intensity. A physical picture of this SHG has been introduced that assumes phase-matched SHG in the self-induced surface waveguide. Peculiar angular, crystal orientation, and polarization dependencies of this SHG are presented. They may account for anomalous SHG in BaTiO$_3$ recently reported in the literature. The observed phenomenon may have many potential applications in nonlinear surface spectroscopy. Also, it may be considered as an example of guiding of light with light in a self-induced surface waveguide, which may find applications in such emerging soliton related techniques as writing virtual photonic circuits [16], etc.

[1] Surface Polaritons, edited by V. M. Agranovich and D. L. Mills (North-Holland, Amsterdam, 1982); H. Raether, Surface Plasmons, Springer Tracts in Modern Physics Vol. 111 (Springer, Berlin, 1988).
[2] G. S. Garcia Quirino, J. J. Sanchez-Mondragon, and S. Stepanov, Phys. Rev. A **51**, 1571 (1995).
[3] M. Cronin-Golomb, Opt. Lett. **20**, 2075 (1995).
[4] B. Crosignani, P. Di Porto, M. Segev, G. Salamo, and A. Yariv, Riv. Nuovo Cimento **21**, 1 (1998).
[5] Y. Kawata, C. Xu, and W. Denk, J. Appl. Phys. **85**, 1294 (1999).
[6] Handbook of Lasers with Selected Data on Optical Technology, edited by R. J. Pressley (CRC Press, Cleveland, OH, 1971), p. 509.
[7] W. E. Torruellas, Z. Wang, D. J. Hagan, E. W. VanStryland, G. I. Stegeman, L. Torner, and C. R. Menyuk, Phys. Rev. Lett. **74**, 5036 (1995).
[8] E. V. Bursian, V. G. Zalesskii, A. A. Luzhkov, and V. V. Maslov, JETP Lett. **64**, 270 (1996).
[9] L. D. Rotter, D. L. Kaiser, and M. D. Vaudin, Appl. Phys. Lett. **68**, 310 (1996).
[10] O. Auciello, J. F. Scott, and R. Ramesh, Phys. Today **51**, No. 7, 22 (1998).
[11] M. P. Petrov, S. I. Stepanov, and A. V. Khomenko, Photorefractive Crystals in Coherent Optical Systems (Springer, Berlin, 1991).
[12] Y. R. Shen, Science **276**, 1520 (1997).
[13] A. W. Snyder and D. J. Mitchell, Science **276**, 1538 (1997).
[14] Y. R. Shen, The Principles of Nonlinear Optics (Wiley, New York, 1984), pp. 479–504.
[15] F. Zernike and J. E. Midwinter, Applied Nonlinear Optics (Wiley, New York, 1973).
[16] A. W. Snyder and F. Ladouceur, Opt. Photonics News **10**, No. 2, 35 (1999).

Near-field optical study of photorefractive surface waves in BaTiO₃

Igor I. Smolyaninov and Christopher C. Davis

Department of Electrical Engineering, University of Maryland, College Park, Maryland 20742

Near-field optical microscopy has been used to study photorefractive surface waves in BaTiO₃. The field distribution of the photorefractive surface wave near the crystal–air interface has been measured and compared with theory. Experimental data indicate that a micrometer-wide transition layer with dielectric and photorefractive properties that are different from the properties of the bulk BaTiO₃ exists near the interface. © 1999 Optical Society of America

OCIS codes: 180.5810, 190.5330, 190.4350, 240.6690.

Recently a new kind of nonlinear surface electromagnetic wave (SEW) called a photorefractive surface wave was predicted[1] and observed experimentally[2] in BaTiO₃. This phenomenon is closely related to self-trapped optical beams (also known as spatial solitons) and self-bending beams observed in photorefractive crystals.[3] A photorefractive SEW occurs when a beam that is self-bent toward the positive direction of the optical axis (the poling direction) undergoes a cycle of deflections toward the face of the crystal and subsequent total internal reflections. The resultant nonlinear SEW is localized near the crystal–air interface with a penetration depth as small as 10 μm into the photorefractive crystal.[1] This localization leads to strong enhancement of the optical field near the interface, which should cause a significant enhancement of all nonlinear surface optical phenomena [such as surface-adsorbed molecular luminescence, Raman scattering, and surface second-harmonic generation (SHG)]. Giant enhancement of surface SHG in BaTiO₃ as the result of photorefractive SEW excitation was observed recently.[4]

All SEW's are sensitive to the optical properties of the guiding interface, which are different from the properties of the bulk medium. The concept of the transition layer is usually used to describe the behavior of the dielectric constant (and other optical parameters) near the interface in a macroscopic electrodynamics approach. Detailed measurements of the SEW field distribution and comparison of these data with theoretical models may provide valuable information on the properties of transition layers.

In this Letter we report near-field optical measurements performed on photorefractive surface waves excited on the surface of a BaTiO₃ crystal. The field distribution of the photorefractive surface wave near the crystal–air interface was measured and compared with theory. Experimental data indicate that a micrometer-wide transition layer with dielectric and photorefractive properties that are different from the properties of bulk BaTiO₃ exists near the interface.

Our experimental geometry is shown in Fig. 1. The iron-doped crystal of BaTiO₃ (from Sanders, Inc.) used in the experiments is a 8 mm × 8 mm × 8 mm cube

that was cut with two opposing faces perpendicular to the c axis and poled along the c axis. This crystal cut permits photorefractive SEW propagation only on the top face of the crystal (only near this face can photorefractive self-bending and total internal reflection compete with each other). The crystal was mounted upon the three-axis translation sample stage of a near-field optical microscope described elsewhere.[5] Horizontally (ordinarily) polarized light from an argon-ion laser operating at 488 nm was focused with a 40× microscope objective onto the top edge of the crystal within a few micrometers of the top face. The direction of the beam was parallel to the top face of the crystal. This geometry corresponds to the geometry of photorefractive SEW excitation reported in Ref. 2. Near-field measurements were performed on the top face and on the side (exit) face of the BaTiO₃ crystal.

Figure 2 shows the data for field distribution measurements performed near the edge of the exit face of the crystal where the photorefractive SEW was leaving the surface of the crystal. The position of the edge is determined from the topographical data (shown in the same figure and marked by the arrow). The flat part of the topographical data (at distances larger than 8 μm) corresponds to feedback saturation where the tip of the microscope falls off the edge of the crystal. The field distribution calculated according to the theory given in Ref. 1 is shown in the same figure
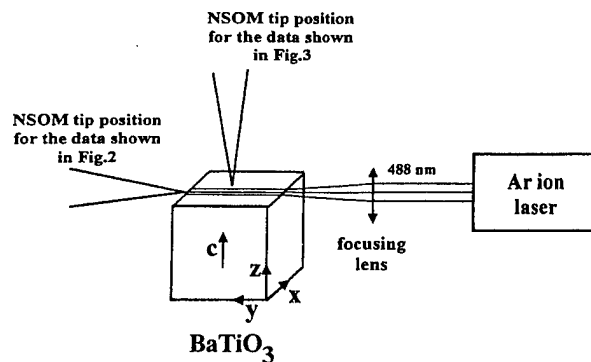

Fig. 1. Schematic view of our experimental geometry: NSOM, near-field scanning optical microscopy.

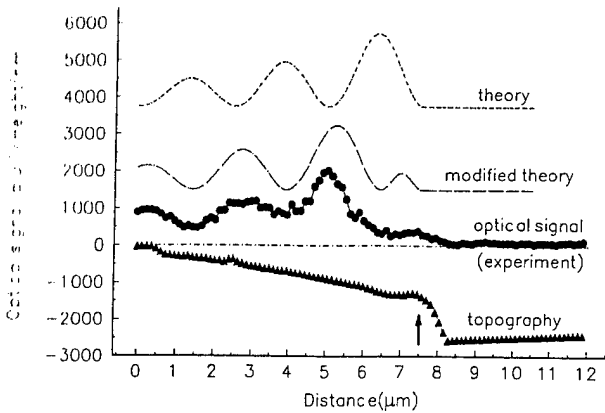© 1999 Optical Society of America

Fig. 2. Comparison of measured photorefractive SEW field distribution near the edge of the exit face of the crystal with theory. The position of the edge is determined from the topographical data and is marked by an arrow. The flat part of the topographical data (at distances larger than 8 μm) corresponds to feedback saturation when the tip of the microscope falls off the edge of the crystal.

(labeled theory). Although our data follow theoretical predictions quite well, there is a substantial difference in the SEW field behavior near the interface. To understand what parameters of the model must be changed to account for this discrepancy, let us recall the basic points of the theory of photorefractive SEW.

Nonlinear SEW solutions of the Maxwell equations in a photorefractive medium can be found as follows[1]: It is assumed that a SEW written as $E(z, y) = E(z)\exp(-iky)$ induces a dielectric constant changes of the form $\epsilon(z) = \epsilon + \delta\epsilon(z)$ because of the photorefractive effect. [Here $E(z)$ is assumed to be real, ϵ is the real dielectric constant of the medium in the absence of the wave, the photorefractive medium is assumed to be optically isotropic, and the field distribution is assumed to be independent of x. These simplifying assumptions may not be true in the most general case, but they allow us to illustrate the basic physics of the phenomenon.] Substituting this equation into Maxwell's equations results in the following equation for $E(z)$:

$$[d^2/dz^2 + (k_0^2 - k^2) + k_0^2 \delta\epsilon(z)/\epsilon]E(z) = 0, \quad (1)$$

where $k_0 = \omega(\epsilon\epsilon_0\mu_0)^{1/2}$ is the wave number of the light in a linear medium with the same unperturbed dielectric constant ϵ. Assuming the diffusion mechanism for nonlinearity,[6] the distribution of $\delta\epsilon(z)$ can be related to $E(z)$ through the space-charge electric field E_{sc}:

$$E_{sc} = -(k_B T/e)[dI(z)/dz]/I(z), \quad (2)$$

where $I(z)$ is the intensity of light. The space-charge electric field induces refractive-index changes by means of the electro-optic effect[6]:

$$\delta\epsilon(z) = 2n^4 r(k_B T/e)[dE(z)/dz]/E(z), \quad (3)$$

where r is the linear electro-optic coefficient. Thus we obtain the wave equation in the form

$$[(d^2/dz^2)/k_0^2 + (2\gamma d/dz)/k_0 - 2(k - k_0)/k_0]E(z) = 0, \quad (4)$$

where $\gamma = k_0 n^2 r(k_B T/e)$. Equation (4) has a solution that decays exponentially into the photorefractive medium:

$$E(z) = \exp(-\gamma k_0 z)\cos\{[2(k - k_0)k_0]^{1/2}z + \phi\}. \quad (5)$$

In the case of BaTiO$_3$ the photorefractive SEW field penetration depth is $d_z = (\gamma k_0)^{-1} \sim 10$ μm.[1] Because the resultant equation (4) is linear, this penetration depth does not depend on the field intensity. The phase ϕ is easy to find from the boundary conditions. The theoretical field distribution found in this way is shown in Fig. 2 (labeled theory). Similar results can be found in Ref. 1.

The value of field penetration depth d_z observed in the experiment is close to the theoretical prediction. Only the behavior near the interface is unaccounted for. The simplest way to explain this difference is to assume the existence of a transition layer with dielectric and photorefractive properties that are different from the properties of bulk BaTiO$_3$. Thus Maxwell's equations have to be solved for a three-layer medium. The curve labeled modified theory in Fig. 2 represents the best fit obtained in this way. It corresponds to a 1-μm-wide transition layer with a refractive index 0.01 higher than the refractive index of the bulk BaTiO$_3$ ($\sim$2.6 at 488-nm light wavelength) and much weaker photorefractive properties (much smaller γ). The exact value of the refractive-index change is (to some extent) a function of the transition layer width. But it is clear from the shape of the measured optical signal that a transition layer of the order of 1 μm does exist near the interface. Attenuation of photorefractive properties near the interface may be expected in a material with a diffusion mechanism for nonlinearity (electric charges cannot diffuse into the air side of the interface). Another likely reason for the existence of the transition layer is surface charging. It is an interesting theoretical problem to derive the properties of this transition layer from microscopic theory.

Characteristic near-field images of the photorefractive SEW propagation along the top face of the crystal are shown in Fig. 3. The optical image in Fig. 3(b) exhibits a set of periodic higher- and lower-intensity regions in the direction of SEW propagation. This behavior may be expected in a model of the photorefractive SEW as a beam undergoing a cycle of photorefractive deflections toward the face of the crystal and subsequent total internal reflections. Thus a periodic self-induced modulation of the refractive index near the surface of BaTiO$_3$ crystal may be expected. Such a situation would closely resemble the geometry of SHG experiments with periodically poled nonlinear crystals such as lithium niobate, which show substantial enhancement of SHG efficiency (periodic poling creates periodic modulation of the refractive index near the interface). This analogy may explain some features of strongly enhanced surface SHG in BaTiO$_3$ owing to recently observed photorefractive SEW excitation.[4]

In conclusion, we have performed, for the first time to our knowledge, a near-field optical study of photorefractive SEW's in BaTiO$_3$. A micrometer-wide
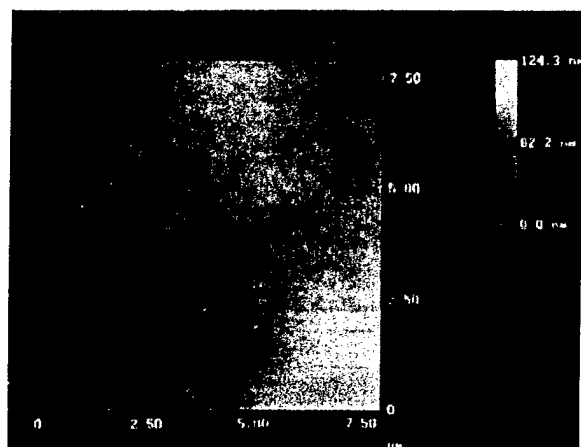
(a)
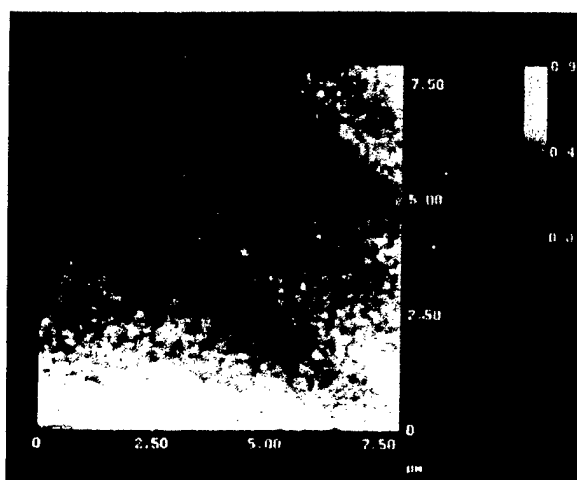
(b)

Fig. 3.   (a) Topography and (b) near-field optical image of photorefractive SEW propagation along the top face of the crystal.

transition layer with dielectric and photorefractive properties that are different from the properties of the bulk $BaTiO_3$ was observed.   Near-field images of SEW propagation along the interface show periodic bouncing of light off the interface as a result of the competition between photorefractive self-bending and total internal reflection.

I. I. Smolyaninov's e-mail address is smoly@ eng.umd.edu.

References

1. G. S. Garcia Quirino, J. J. Sánchez-Mondragón, and S. Stepanov, Phys. Rev. A **51**, 1571 (1995).
2. M. Cronin-Golomb, Opt. Lett. **20**, 2075 (1995).
3. B. Crosignani, P. Di Porto, M. Segev, G. Salamo, and A. Yariv, Riv. Nuovo Cimento **21**, 1 (1998).
4. I. I. Smolyaninov, C. H. Lee, and C. C. Davis, "Giant enhancement of surface second harmonic generation in $BaTiO_3$ due to photorefractive surface wave excitation," Phys. Rev. Lett. (to be published).   Paper available at http://xxx.lanl.gov/abs/cond-mat/9906252.
5. I. I. Smolyaninov, D. L. Mazzoni, and C. C. Davis, Phys. Rev. Lett. **77**, 3877 (1996).
6. M. P. Petrov, S. I. Stepanov, and A. V. Khomenko, *Photorefractive Crystals in Coherent Optical Systems* (Springer-Verlag, Berlin, 1991).